

On-chip Mammalian Cell Cultivation and Monitoring

Vom Fachbereich für Physik und Elektrotechnik
der Universität Bremen

zur Erlangung des akademischen Grades eines

Doktor-Ingenieur (Dr.-Ing.)

genehmigte Dissertation

von

M.Sc. Frank Bunge

aus Lilienthal

Referent: Prof. Dr.-Ing. Michael J. Vellekoop
Universität Bremen

Korreferent: Prof. Dr.-Ing. habil. Gerald Gerlach
Technische Universität Dresden

Eingereicht am: 17.04.2018
Tag des Promotionskolloquiums: 02.07.2018

Abstract

The biological and medical progress is, among other factors, also enabled by powerful analysis devices. In the future, new tools will be based on microfluidics to assay mammalian cells. In this thesis, novel concepts for long-term cultivation and monitoring of cells are investigated in the context of Lab-on-a-Chip, which are compact analysis systems in which all relevant processes are integrated. In general, the focus of this work is laid on entire systems instead of single components or functionalities. In particular, the requirements for the presented systems are the usage of non-cytotoxic materials, the fabrication based on clean room processes, the integration of functionalities to avoid bulky and expensive external equipment wherever possible and easy-to-use interfaces. The cell monitoring is limited to the measurement of oxygen uptake of mammalian cells which indicates the metabolism, being a key process of living cells.

In this thesis, two concepts are discussed for the on-chip cultivation of adherent mammalian cells. Both concepts contain porous membranes to supply the cells with nutrients and gases by diffusion. The horizontal concept is based on diffusion processes in horizontal direction through membranes made of agarose hydrogel. In contrast, the supply takes place in vertical direction through a membrane of anodised aluminium oxide in the vertical concept. The successful on-chip passaging is shown with MDCK- and HaCaT cells over 48 h and 14 days, respectively.

The oxygen consumption rate is determined by measuring the decay of the oxygen concentration inside a closed microfluidic chip. This sensing is based on an oxygen sensitive, phosphorescent dye that is embedded in a thin, porous film. In addition, electrical heating elements are integrated into the chip while all optical components are part of the assembly. With this system, the oxygen consumption rate of HaCaT cells is determined for different temperatures.

The discussed concepts and results show that microfluidic devices are well suited for on-chip cell cultivation and monitoring despite their requirements.

Kurzfassung

Der medizinische und biologische Fortschritt wird unter anderem durch leistungsvolle Analysemethoden ermöglicht. Zukünftig werden neue Methoden zur Untersuchung von Säugetierzellen auf mikrofluidischen Ansätzen basieren. In dieser Arbeit werden neuartige Konzepte für die Langzeitkultivierung und Überwachung von Zellen im Kontext von Lab-on-a-Chip-Systemen untersucht, in deren kompakten Analysesystemen alle relevanten Prozesse integriert sind. Der generelle Fokus dieser Arbeit wird daher auf komplette Systeme anstelle von einzelnen Komponenten oder Funktionalitäten gelegt. Spezielle Anforderungen an die Systeme sind, dass die Herstellung mit Reinraumtechnologien realisiert wird, dass Funktionalitäten weitestgehend integriert sind um voluminöse und teure externe Geräte zu vermeiden und dass einfach zu benutzende Schnittstellen vorhanden sind. Die Zellüberwachung beschränkt sich auf die Messung der Sauerstoffaufnahme der Zellen, die Aufschluss über den Stoffwechsel als wichtiges Merkmal von lebenden Zellen gibt.

In dieser Arbeit werden zwei Konzepte für die Kultivierung von adhärennten Säugetierzellen diskutiert. Beide enthalten poröse Membranen um die Zellen mit Gasen und Nährstoffen per Diffusion zu versorgen. Das horizontale Konzept basiert auf horizontalen Diffusionsprozessen durch Membranen aus Agarosehydrogel. Im Gegensatz dazu findet die Diffusion im vertikalen Konzept in vertikaler Richtung durch eine Membran aus anodisiertem Aluminiumoxid statt. Die Zellpassage wird für MDCK- und HaCaT-Zellen über 48 h bzw. 14 Tage nachgewiesen.

Die Sauerstoffverbrauchsrate wird durch Messung der abnehmenden Sauerstoffkonzentration in einem geschlossenen mikrofluidischen Chip bestimmt. Die Messung basiert auf einem sauerstoffempfindlichen, phosphoreszierenden Farbstoff, der in einen dünnen porösen Film eingebettet ist. Zusätzlich wird ein elektrisches Heizelement in den Chip integriert, während die optischen Komponenten Teil der Baugruppe sind. Mit diesem System werden die Sauerstoffverbrauchsraten von HaCaT-Zellen für verschiedene Temperaturen bestimmt.

Die vorgestellten Konzepte und deren Ergebnisse zeigen, dass mikrofluidische Systeme gut für die Kultivierung und Überwachung von Zellen auf einem Chip auch unter den eingangs genannten Voraussetzungen geeignet sind.

Contents

1	Introduction	1
1.1	The vision of Lab-on-a-Chip	1
1.2	Focus of this work	3
1.3	Outline	3
2	Lab-on-a-Chip for Cell Applications	5
2.1	Characteristics of Lab-on-a-Chip	5
2.1.1	Advantages	5
2.1.2	Challenges	6
2.2	State of the art	7
2.2.1	Cell cultivation	7
2.2.2	Analysis methods	11
2.3	Conclusion	13
3	On-chip Cultivation of Mammalian Cells	15
3.1	Requirements	16
3.1.1	General requirements	17
3.1.2	Choice of materials	18
3.1.3	Supply with gases	19
3.1.4	Supply with nutrients	20
3.2	Concept	22
3.2.1	Horizontal supply concept	22
3.2.2	Vertical supply concept	23
3.3	Porous membranes	24
3.3.1	Hydrogels as porous walls	25
3.3.1.1	Properties of hydrogels	25
3.3.1.2	Integration based on symmetrical surficial phaseguides	26
3.3.2	Porous anodised aluminium oxide	28
3.3.2.1	Comparison of different porous materials	28
3.3.2.2	Formation of pores by anodisation of aluminium . .	29
3.3.2.3	Properties of anodised aluminium oxide	31
3.3.3	Silica-aerogels as porous membranes	32
3.3.4	Comparison of the porous materials	36

3.4	Implementation	38
3.4.1	Design of the horizontal concept	38
3.4.1.1	Application of surficial phaseguides	38
3.4.1.2	Diffusion of oxygen	42
3.4.1.3	Detailed design of the chip	47
3.4.2	Design of the vertical concept	47
3.4.3	Fabrication	50
3.4.3.1	Horizontal concept	50
3.4.3.2	Vertical concept	53
3.4.4	Assembly	56
3.4.4.1	Horizontal supply concept	56
3.4.4.2	Vertical supply concept	56
3.4.4.3	Parylene coating	58
3.5	Experiments and results	59
3.5.1	Characterisation of the horizontal supply chip	59
3.5.1.1	Phaseguides	59
3.5.1.2	Oxygen supply	62
3.5.2	Characterisation of the vertical supply chip	64
3.5.2.1	Properties of the pores	64
3.5.2.2	Diffusion through the membrane	65
3.5.3	2D-cell cultivation	66
3.5.3.1	Horizontal supply chip	66
3.5.3.2	Vertical supply chip	68
3.5.4	3D-cell cultures	70
3.6	Comparison of both concepts	75
3.7	Conclusion	78
3.8	Outlook	79
4	Cell Monitoring: Measurement of the Oxygen Consumption Rate of Cells	81
4.1	Theoretical background	82
4.1.1	Principle of photoluminescent oxygen sensing	82
4.1.2	Sensor properties	83
4.1.3	Read-out methods	84
4.1.4	Sensing dyes	85
4.1.5	Matrix	86
4.2	Concept	87
4.2.1	Requirements	87
4.2.2	Sensor layout	88

4.3	Implementation	89
4.3.1	Chip design	90
4.3.2	Heating element	91
4.3.3	Sensing film	91
4.3.4	Fabrication	93
4.3.5	Temperature control and electrical read-out system	96
4.3.6	Assembly	99
4.4	Results	101
4.4.1	Characterisation of the temperature control	102
4.4.2	Characterisation of the sensing film	104
4.4.2.1	Methods	106
4.4.2.2	Intensity of the film	106
4.4.2.3	Photo-oxidation of the film	109
4.4.2.4	Response time of the film	110
4.4.2.5	Phase shift of the polystyrene film	110
4.4.2.6	Comparison of the read-out methods	112
4.4.3	Cell experiments	113
4.4.3.1	Methods	113
4.4.3.2	Oxygen consumption of cells	114
4.4.3.3	Temperature dependency of the oxygen consumption	115
4.5	Conclusion	115
4.6	Outlook	117
5	Conclusion	121
	Bibliography	CXXV
	List of publications	CXXXVII
	Acknowledgements	CXXXIX

List of Abbreviations

Abbreviation	Description
AAO	Anodized aluminium oxide
CAD	Computer aided design
DRIE	Deep reactive ion etching
DMEM	Dulbecco's modified eagle medium
ECM	Extra-cellular matrix
EPDM	Ethylene propylene-diene monomer
FBS	Fetal bovine serum
HaCaT	Immortal keratinocyte cell line from adult human skin
HMDS	Hexamethyldisilazane
LoC	Lab-on-a-Chip
MEMS	Micro-electro-mechanical systems
MDCK	Madin-Darby kidney cells
μ TAS	Micro-total-analysis-system
OCR	Oxygen consumption rate
ODT	Octadecanethiol
ORMOSIL	Organically modified silica gel
PdTFPP	Palladium(II)-5,10,15,20-tetrakis-(2,3,4,5,6-pentafluorophenyl)-porphyrin
PDMS	Polydimethylsiloxane
PEG	Polyethylene glycol
PS	Polystyrene
PT1	First order lag element
PTFE	Polytetrafluoroethylene
PtTFPP	Platinum(II)-5,10,15,20-tetrakis-(2,3,4,5,6-pentafluorophenyl)-porphyrin
$[\text{Ru}(\text{dpp})_3]^{2+}$	Tris(4,7-diphenyl-1,10-phenanthroline) ruthenium(II) complex
SEM	Scanning electron microscope
SU8	Epoxy-based negative photoresist
TEOS	Tetraethyl orthosilicate

List of variables

Variable	Description	Unit
A_c	Cross-section area	m^2
A_z	Area covered by a cell	m^2
c	Concentration	$\frac{g}{L}$ or $\frac{mol}{L}$
c_{O_2}	Concentration of dissolved oxygen	$\frac{mol}{L}$
D	Diffusion constant	$\frac{m^2}{s}$
d	Diameter	m
d_p	Pore diameter	m
h	Height	m
f	Frequency	Hz
I	Intensity	-
I_0	Intensity in the absence of oxygen	-
$I_{0,0}$	Intensity in the absence of oxygen at the temperature T_0	-
k_{dO_2}	Solubility of oxygen	$\frac{g}{L Pa}$
K_I	Amplification of the integral part of the PI-control	-
K_{m,O_2}	Michaelis-Menten-constant	$\frac{mol}{L}$
K_P	Amplification of the proportional part of the PI-control	-
K_{SV}	Stern-Volmer-constant	1/%(air)
$K_{SV,0}$	Stern-Volmer-constant at the temperature T_0	1/%(air)
n	Amount of substance	mol
OCR	Oxygen consumption rate of cells	$\frac{amol}{cells}$
p	Pressure	Pa
p_{O_2}	Partial pressure of oxygen	Pa
R_s	Electrical resistance of the temperature sensor	V
r	Radius	m
r_{xy}	Radius in the x-y-plane	m
r_{yz}	Radius in the y-z-plane	m
T	Temperature	$^{\circ}C$
t	Time	s
t_{ph}	Width of the phaseguides	m
U	Voltage	V
U_{out}	Output voltage	V
V	Volume	m^3
V_z	Volume of a cell	m^3
w_c	Channel width	m
w_{Gr}	Width of the growth chamber	m

Variable	Description	Unit
w_{Hg}	Width of the hydrogel	m
x_m	Dimension of the meniscus in x-direction	m
y_m	Dimension of the meniscus in y-direction	m
y_{mis}	Misalignment in y-direction	m
α_{I_0}	Temperature coefficient of the intensity in the absence of oxygen	$\frac{1}{^\circ\text{C}}$
$\alpha_{K_{SV}}$	Temperature coefficient of the Stern-Volmer-constant	$\frac{1}{^\circ\text{C}}$
α_{PG}	Ratio of the width and of the height of the phaseguide	-
α_{Pt}	Temperature coefficient of the electrical resistance of platinum	$\frac{1}{^\circ\text{C}}$
α_w	Angle of wall in the x-y-plane	$^\circ$
γ_f	Filling factor which is the relative area that is covered with cells regarding the total area	-
γ_Q	Relative amount of the dye that is quenched	-
ΔR_s	Change of the electrical resistance of the temperature sensor	V
ΔT	Temperature difference	$^\circ\text{C}$
θ	Contact angle	$^\circ$
θ_d	Contact angle at the boundary between two surfaces	$^\circ$
θ_{gl}	Contact angle on glass	$^\circ$
θ_{odt}	Contact angle on ODT	$^\circ$
θ_w	Contact angle on the wall	$^\circ$
σ	Surface tension	$\frac{\text{N}}{\text{m}}$
τ	Lifetime	s
τ_0	Lifetime in the absence of oxygen	s
φ	Phase delay	$^\circ$
φ_0	Offset of the phase delay	$^\circ$

1 Introduction

Mammalian cells are the most common subjects in biological and medical research and analyses. In many cases, these activities require the cultivation of cells over several hours and days while their behaviour and their reaction is monitored. The technical progress enables the research on new microfluidic devices for the on-chip cell cultivation and cell monitoring, which will result in better tools and methods compared to the current state. The concepts and results of this thesis contribute to the technical aspects of this research by investigating new concepts.

The realisation of new techniques, such as the on-chip cell cultivation and monitoring, requires holistic approaches instead of the optimisation of one functionality. These approaches for biomedical applications of microfluidic devices are summarised by the vision of Lab-on-a-Chip (LoC) that is described in more detail in sec. 1.1. The principles of this vision are included in many considerations expressed in this thesis. The main focus is discussed in sec. 1.2 followed by the outline in sec. 1.3.

1.1 The vision of Lab-on-a-Chip

Tremendous progress in the field of microelectronics and micro-electro-mechanical systems (MEMS) has led to the expectation of similar success with microfluidic systems. The aim of such microfluidic systems is the manipulation or analysis of liquids or particles inside liquids, which is attractive for biological and medical applications. These analysis processes are usually run in laboratories and require manpower despite the automation e.g. with handling robots. The concept of Lab-on-a-Chip (LoC) is to integrate all processes that are required for the analysis into one chip and, consequently, to minimise the entire lab. This definition is not exclusive for Lab-on-a-Chip but also valid for other terms like micro-total-analysis-systems (μ TAS).

The relevant processes are categorised as¹:

1. Sample handling: The handling includes minor but not less important processes like inserting the samples into the device, transporting the liquids between different parts of the chip and also removing them after the process.

¹Not all mentioned processes are necessarily part of a LoC while some might occur more than one time.

2. Sample preparation: The liquids have to be prepared prior to the analysis. This might include mixing with other liquids (e.g. with antibodies), the separation into different components (e.g. separation of cells from the blood), chemical reactions, physical processes like heating or cooling or biological processes like cell cultivation.
3. Sensing: The target is the analysis of the liquids or particles inside the liquids. Common methods are optical analysis (e.g. with a microscope) sometimes in combination with fluorescence, electrical sensing (e.g. amperometry) or mechanical sensing (e.g. the viscosity).
4. Signal processing and interpretation: The measured signals have to be processed and the results have to be interpreted to extract the information.

LoCs are used only for commercial applications if they perform significantly better than the current processes in the lab [68]. In general, the process with LoC must be either much cheaper, easier to use, faster or provide better results (e.g. higher sensitivity, accuracy, etc.) to compensate the efforts of introducing a new technology to the scientists or lab technicians. The benefits are addressed by three different categories of applications for LoC [92]:

1. Diagnostic devices for environments with little or no infrastructure: Such LoCs should not replace laboratories but should be used where labs are not available such as in developing countries or for in-home-testing. This enables a better diagnose to the patients and therefore a suitable therapy. Such devices have to be very easy to use, cheap and scalable for mass fabrication.
2. Rapidly assaying of biofluids: Some common techniques of biological assaying for medical applications (such as identification of pathogen and antibiotic testing) take several hours or days. In this case, LoCs aim to analyse the liquids much faster by using different sensing methods or benefiting of smaller samples. Consequently, the therapy can be started earlier or be more specific and thus provide a higher chance of success. All in all, the performance for these applications is more important than a low price or the ease of use.
3. Pharmaceutical research: The testing of new drugs, diagnostics and fundamental research require a high number of in-vitro cell cultures. Therefore, the aim of LoC for pharmaceutical research is to lower the costs per test significantly or mimic in-vivo-conditions better than standard cultures. The latter benefit might be based on different physiological parameters (e.g. shear stress, surface properties) or the coculturing of different cells which results in entire organs-on-a-chip. Consequently, new drugs or therapies are available faster and at lower costs.

1.2 Focus of this work

In this thesis, new approaches are investigated for the cultivation and monitoring of mammalian cells inside closed microfluidic devices. The chips are realised in the context of LoC and are targeted, but not limited, to future applications for the pharmaceutical research. In general, the emphasis is put on the entire system instead of individual components. In particular, the cell cultivation aims at the passaging of mammalian cells, which includes the seeding inside the microfluidic devices, the feeding with gases and nutrients over several hours or days and the removal of the cells.

Various parameters of cells and the cell culture can be monitored, such as the number of cells, their metabolism or the change of the culture media composition. In this thesis, the focus is placed on the oxygen consumption rate of the cells because this parameter is directly linked to the cell metabolism. Furthermore, the oxygen consumption also indicates the state of the cells and their response to environmental parameters by an increased or decreased oxygen uptake. Therefore, monitoring the oxygen consumption of the cells is of particular interest for biological and pharmaceutical researchers.

1.3 Outline

In this thesis, the cell cultivation and cell analysis is described in the context of LoC. Consequently, LoC are explained at first in chapter 2. In that chapter, these systems are characterised and the state of the art regarding the cultivation and analysis of mammalian cells is discussed.

Chapter 3 explains two different concepts for the on-chip cell cultivation. Both concepts are based on the supply of gases and nutrients to the cells by diffusion through porous membranes. Therefore, suitable porous materials are investigated regarding their properties and fabrication methods. Subsequently, the implementation is described including design aspects of both concepts, their fabrication by clean room processes and their assembly. Both concepts are afterwards characterised regarding their membranes and their capability to cultivate mammalian cells. Finally, both concepts are compared and conclusions are presented.

A similar structure is used for the cell monitoring in chapter 4 in which a chip to measure the oxygen consumption rate of mammalian cells is investigated. At first, the theoretical background of the sensing principle is discussed and the concept of this chip is presented. Following, the implementation regarding the design, the sensor and chip fabrication, the assembly and the electrical circuits are described.

Finally, the system is characterised regarding its oxygen sensing properties and regarding the cell experiments.

In the end, the investigated devices are compared to the characteristics of LoC and conclusions are drawn in chapter 5.

2 Lab-on-a-Chip for Cell Applications

Lab-on-a-Chip is a vision of holistic concepts of microfluidic systems for the analysis of biological or medical samples. A vision is defined as a trend-setting plan for the future. Such as every new concept, there are some significant differences compared to today's analysis processes (see sec. 2.1).

A vision describes usually an ideal state in the future. However, the ideal and perfect LoC is not and will not be realised because of physical or economical restrictions. Though, there are already several approaches which follow the idea of LoC. An overview about important systems that are of interest for this thesis is given in sec. 2.2. In particular, this includes systems for cultivation and for monitoring of the oxygen consumption of mammalian cells.

The investigation of the characteristics and of the state of the art allows conclusions about the current achievements and also about the next steps to make LoCs successful in the real world (see sec. 2.3).

2.1 Characteristics of Lab-on-a-Chip

LoC are systems that contain components to address all processes as mentioned in sec. 1.1. The miniaturisation has several attractive features as described in sec. 2.1.1 but also requires some concepts and technologies that differ from the macroscopic world (e.g. efficient mixing of two fluids by diffusion) as presented in sec. 2.1.2.

2.1.1 Advantages

LoCs provide several advantages compared to macroscopic systems. First of all, the dimensions are smaller by several magnitudes. On one hand, some useful physical effects are almost eliminated by the downscaling, like turbulent flows which do not exist in small microfluidic channels and hamper the mixing of fluids. On the other hand, some effects are very powerful when the dimensions are reduced to micrometers, such as the fast diffusion of molecules through porous materials. Consequently, LoC enables the application of new sensing and actuation principles. In case of in-vitro cell cultures, LoC might represent the in-vivo conditions better than conventional cell cultures, e.g. by textured surfaces, 3D-cell cultures, coculturing

of different cells in one system, etc. Last but not least, smaller volumes allow fast processes, e.g. faster heating-cooling-cycles or faster exchange of samples.

As the systems are scaled down, the sample volumes are also reduced significantly. Some of the chemicals of biological analysis methods are very expensive meaning that smaller volumes reduce the process costs significantly. In case of medical analysis, smaller sample volumes mean that e.g. less blood has to be drawn from the patient or enables the analysis of special liquids e.g. intra-articular fluid¹.

All functionalities are integrated in an ideal LoC. Consequently, the entire assembly is very small and therefore easy to transport. Hence, biomedical analysis can be carried out outside of laboratories, e.g. directly in hospitals, ambulances or at home. Furthermore, the integration and crosslinking of different steps facilitates the automation of LoC. Consequently, LoCs are easy to use and require no manpower which cut the running costs down and allows the usage of LoCs in developing countries without highly skilled staff.

Similar to microelectronics, the expenses consist of high development costs for the chip design and for the process development as well as fixed costs for the machines but low individual costs (e.g. for materials). The fabrication is wafer based and each wafer contains numerous devices. The process time is independent of the number of devices per wafer and independent of the wafer dimension. Consequently, the individual costs decrease significantly with an increasing number of the devices. Therefore, LoCs have potentially low fabrication costs in case of mass production.

2.1.2 Challenges

There are some major challenges that prevent the breakthrough of LoCs [21, 68, 109]. Many systems, that are claimed as LoCs, require external equipment such as pumps, valves, read-out systems (e.g. microscopes, spectrometers) or specialised electrical equipment (e.g. high voltage sources or waveform generators). These devices are usually bulky, expensive, sometimes difficult to use and require skilled staff and thus thwart the idea of LoC. Consequently, these systems are no real LoCs but are referred to as "Chips-in-a-Lab" which are considered as intermediate step towards the vision of LoC.

The miniaturisation of these components like pumps or valves was shown on individual chips but the integration of all components into one device is very complex, costly and requires a very high reliability of each component. The fully integrated LoC is a vision, but the same objectives can be fulfilled with a "Chip-in-a-Lab" approach as long as the external components are sufficiently small, cheap and effective. The technical progress of microelectronics enables e.g. the use of

¹Intra-articular fluid that might appear in the joints in case of infections or other diseases.

smartphone cameras instead of microscopes or small DC-DC-converters instead of bulky high voltage sources.

Nevertheless, these external components increase the price of the system. In addition, the packaging of the chip, the assembly of the components and perhaps the alignment of the optical components can be more expensive than the fabrication of the chip itself.

Most approaches of LoCs in the world of academic research are made out of polydimethylsiloxane (PDMS) because of its advantages regarding fast prototyping. PDMS, made by an easy and cheap moulding process, is flexible and soft meaning that it is hard to break. However, the fabrication and the assembly are basically manual work which makes this material not suitable for mass production [21, 92, 109]. Due to other difficulties of PDMS (see sec. 3.1.2), the conversion of these academic devices made out of PDMS to commercial LoCs requires different materials that are ideally low cost and enable low cost standard processes.

LoCs require an interface to the macroscopic world to provide new samples and chemicals but also to withdraw them after the analysis or to remove the waste. In contrast to electronic interfaces, there are no standard connectors or plugs for microfluidics. Though, easy and reliable interfaces are essential and have to be considered when designing a system.

Last but not least, biologists developed their standard protocols without LoCs. Working with LoCs differs from common methods and requires different skills. Consequently, the users are reluctant to use LoCs instead of their standard protocols unless LoCs provide a significant progress (e.g. cheaper or faster by one order of magnitudes or new functionalities).

2.2 State of the art

Lab-on-a-Chip is a vision for various analytical methods. Here, a general overview is given about the state of the art regarding cell cultivation (sec. 2.2.1) and cell analysis (sec. 2.2.2).

2.2.1 Cell cultivation

For many years, researchers developed various concepts for the cultivation of mammalian cells in microfluidic devices. An overview about some approaches for LoC-devices with on-chip cell cultivation is given in tab. 2.1 [14], where the systems are described regarding the application and how gases and nutrients are supplied.

Apart from a few special concepts, there are two main types as summarised in fig. 2.1: either the cells adhere to a surface or they are embedded in a matrix. The

Table 2.1: Comparison of different microfluidic approaches to culture mammalian cells on-chip.

Description	Year	Comment	Nutrient supply	Gas supply	Ref.
3D-cell culture	2005	Closed chip out of glass and silicon	Perfusion & diffusion through 3D-culture	Perfusion with fresh medium	[36]
3D-cell culture	2007	-	Diffusion through 3D-culture	Diffusion through PDMS	[102]
Highly integrated perfusion system	2011	Integration of heater, pump and electrical readout	Perfusion	Diffusion through PDMS	[60]
CO ₂ -control culture	2011	Gradient of CO ₂	Perfusion	Diffusion through PDMS	[35]
Blood-brain-barrier	2012	Coculture and conductivity measurements	Perfusion & diffusion through membrane	Diffusion through PDMS	[6]
Assay for coculturing	2012	Suitable for 2D and 3D-cell cultures	Diffusion through hydrogel	Diffusion through PDMS	[96]
PDMS-hydrogel hybrid reactor	2013	3D-culture on multi-electrode array	Diffusion through 3D-culture	Diffusion through PDMS	[94]
Blood-vessel-on-a-chip	2013	3D-Coculture	not possible	Diffusion through PDMS	[106]
Shear-stress culture	2014	Chamber with different shear stress on cells	Perfusion	Diffusion through PDMS	[42]
Cancer metastasis under hypoxia	2014	Integration of gas supply and oxygen sensor	Perfusion	Diffusion through PDMS	[1]
On-chip incubator	2014	Integration of oxygen supply	Perfusion	Oxygen dissolved in medium	[100]
Breast-cancer analysis	2015	3D-cell culture	Diffusion through 3D-culture	Diffusion through PDMS	[50]
Hypoxia monitoring of cells	2015	Oxygen control and sensing for 3D-cell cultures	Perfusion	Diffusion through PDMS	[39]
Lung cancer chip	2016	3D-2D-coculture	Perfusion & diffusion through 3D-culture	Diffusion through PDMS	[119]
Liver-on-a-chip	2016	Modular and pumpless platform for 2D-3D-coculture and electrical measurements	Perfusion & diffusion through 3D-culture	Oxygen dissolved in medium	[32]
Cell invasion	2016	Measurement of cell movement through membrane	Exchange of medium	Open reservoir	[58]
Micro-lung	2017	Integration of membrane and electrical readout	Perfusion	Diffusion through PDMS	[72]

adherent cell cultures can be further distinguished between diffusion based and perfusion based supply structures. When the cells are embedded in a matrix, this matrix might be either fixed inside the chip or suspended.

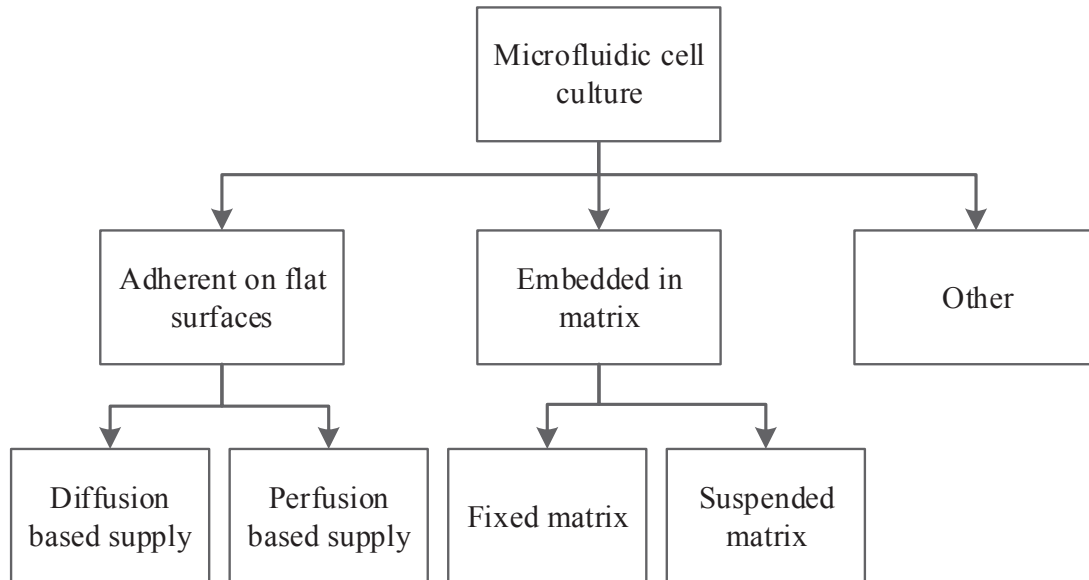


Figure 2.1: Types of microfluidic cell cultures.

Adherent cell cultures

Adherent cell cultures are similar to macroscopic cell cultures in culture flasks, petri-dishes or well-plates. Here, the cells adhere on the bottom of the device and form a 2D-culture. These systems feature:

- easy access to the cells and optional passaging of the cells,
- transferability of protocols and of results to traditional cell cultures,
- good optical inspection,
- optional integration of additional sensors.

The supply with nutrients is realised either by perfusion of the cells or by diffusion through a porous membrane. The perfusion based systems (as shown in fig. 2.2(a)) require only channels and a culture chamber and thus feature an easy design and simple fabrication. With such a device, the influence of shear stress on the cells could be investigated [42] and a high throughput system for parallelised experiments could be realised [47] among other applications (see also tab. 2.1). There are already some systems commercially available such as "The CellASIC[®] ONIX2 Microfluidic System" of Merck KGaA.

Diffusion based culture systems as shown in fig. 2.2(b) contain at least one porous membrane which separates the supply channel from the culture chamber. Consequently, the nutrients or gases diffuse through the membrane. The integration of the membrane complicates the design and fabrication but results in enhanced culturing conditions. Furthermore, the membrane could also separate different cell types which is required to investigate cell-cell-interactions like the blood-brain-barrier [6] or a placenta-on-a-chip [56] (see also tab. 2.1).

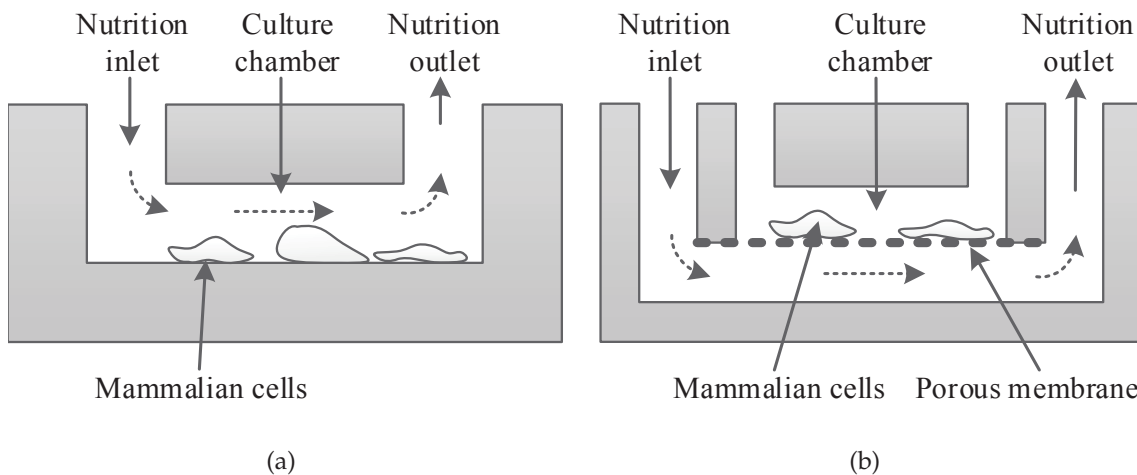


Figure 2.2: General design of adherent cell cultures in microfluidic devices: (a) device in which the supply with nutrients is based on perfusion (b) device in which the supply with nutrients is based on diffusion through a porous membrane.

Cell cultures embedded in a matrix

Instead of culturing the cells on a flat surface, they might also be embedded in a matrix usually made out of hydrogel. Here, the cells form a 3D-cell culture, in which they grow in every direction. The characteristics of these systems are:

- good model for in-vivo conditions, because the cells inside the body also form a 3D-culture,
- infeasibility for cell passaging because the release of the cells from the platform is very difficult,
- high cell densities compared to adherent cultures,
- complex design and fabrication.

As the cells are embedded in a matrix, the supply has to be realised by diffusion through the matrix. The matrix is either fixed inside the chip or suspended. Fixed

matrices as shown in fig. 2.3(a) are the more common type and are usually referred to as 3D-cell cultures. In this case, a suspension of cells and liquid hydrogel is filled into the chip where the matrix gels and forms the culture. The volume of the gel is in the range of a few μL and may contain several thousand cells. Such a 3D-culture could be used to investigate cancer metastasis [1] or breast-cancer [50] (see also tab. 2.1).

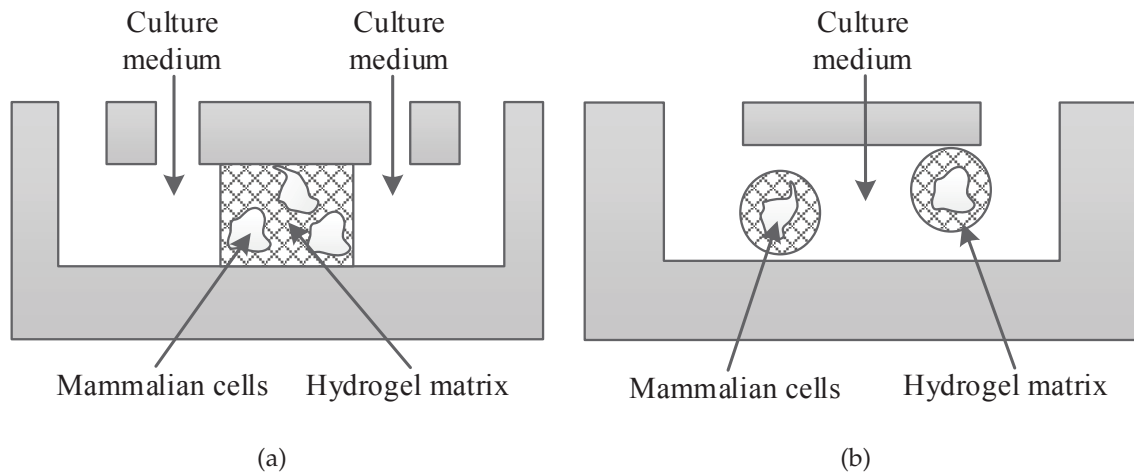


Figure 2.3: General design of cell cultures that are embedded in a matrix: (a) 3D-cell culture, that is fixed inside the microfluidic chip (b) microfluidic chip with suspended particles out of hydrogel containing single cells or a cluster of cells.

The concept of cultures with a suspended matrix differs significantly. Single cells or a cluster of cells are embedded in hydrogel spheres or fibres as shown in fig. 2.3(b), which can be handled, manipulated and analysed afterwards. The advantage is that the cells are better protected e.g. against shear stress, the viability is improved and that they are easier to handle compared to the other devices with a fixed matrix. This concept is based on the formation of small droplets of hydrogel containing the cells [29, 62].

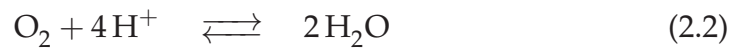
2.2.2 Analysis methods

Almost all properties of mammalian cells can be analysed on-chip nowadays. Apart from the detection of cells in a microfluidic flow cytometer [91], the common cell analysis covers all aspects like whole cell assays [117], mechanical [107] and electrical characterisation, ion channel studies [3] and protein or ion detection [3, 63]. In this work, the focus is laid on the monitoring of cell respiration as an indicator for their metabolism. Consequently, the oxygen concentration and its change over time has to be measured. The concentration of the dissolved oxygen can be determined

either with Clark electrodes based on amperometry or with phosphorescent films as discussed below.

Clark electrode

A common method to detect dissolved oxygen is the amperometric measurement by using Clark electrodes. The setup consists of one platinum electrode that acts as the cathode, a reference electrode as anode, which is usually made out of silver and silver chloride, and sometimes another platinum counter electrode. Depending on the pH-value of the solution, the oxygen reacts if a voltage is applied:



This reaction occurs at voltages between -700 mV and -800 mV . The applied voltage triggers this reaction and the electrical current correlates to the concentration of dissolved oxygen. [116]

Amperometric measurements suffer from low selectivity because various compounds might react at the applied voltage. Especially in cell cultures, the culture medium contains a large variety of proteins, amino acids, salts, etc. (see sec. 3.1.4) and furthermore, sometimes unknown proteins are produced by the cells. To avoid the contact of other compounds with the electrodes, the platinum electrode could be covered with an oxygen permeable membrane. However, such a membrane, e.g. PTFE or 1,3-diaminobenzene [115], is no ideal filter meaning that other molecules might still diffuse through the membrane and interfere with the measurement.

The reaction consumes oxygen which influences the measurement because the oxygen has to diffuse towards the electrodes where a depletion layer is formed. Consequently, lower concentrations are present near the electrodes than far away. In addition, the sensor significantly lowers the oxygen concentration in case of small volumes or very low concentrations. Last but not least, the reaction results in more alkaline products which influence the cell cultures. [85]

The third main disadvantage is the Ag/AgCl-coating of the electrode. These electrodes are not stable since silver chloride dissolves into the liquid. Therefore, the chips can be used only for a limited time. [79]

Though, Clark electrodes are robust and well established in the macroscopic world. Additionally, the integration in microfluidic devices can be realised with common clean room technologies. Therefore, these electrodes have been applied to determine the oxygen concentrations in microfluidic devices despite the mentioned disadvantages. [75, 115]

Luminescent sensing

Luminescent sensing methods are based on the oxygen dependency of phosphorescence of specific dyes. Hence, the setup consists of an oxygen sensitive film, an excitation light source and the sensor to detect the phosphorescence (e.g. a photodiode or a camera). The luminescent is described by the intensity of the emitted light and the lifetime which is the time span between the absorption of the excitation light and the emission of the phosphorescent light. Both parameters are higher in the absence of oxygen and decrease with increasing concentrations.

There is a large variety of sensing films that consist of the sensing dyes and matrices. The most common dyes are metal-ligand complexes like PtTFPP, PdTFPP or Ru(dpp)₃. The matrix are usually either silicon rubber, polystyrene (PS) or organically modified silica gels (ORMOSIL). On one hand, the integration of these films into a close microfluidic system is usually challenging because they do not withstand high temperatures and adhere only poorly on smooth surfaces. On the other hand, the optical readout and the excitation source do not have to be integrated, which lowers the complexity of the chip fabrication.

Due to the large variety of materials, luminescent sensors can be adapted for each application. The sensing film is either applied on a large surface (e.g. inside a microfluidic chip [104]), at the end of an optical fibre [19] or on nanoparticles [57]. Furthermore, the film generally does not consume oxygen. However, photo-oxidation of the organic compounds might occur due to the excitation light. Depending on the dye and the matrix, these sensors are stable up to several weeks [116].

2.3 Conclusion

LoC could trigger a significant progress of diagnostics as well as biological and medical research because of the lower costs, faster analysis methods or new functionalities among other advantages. At the moment, the first diagnostic tools, e.g. for pathogen detection or blood analysis, that follow the vision of LoC, are commercially available. However, the cultivation and long-term monitoring of mammalian cells is still based on conventional petri-dishes or well-plates, although these applications have been addressed as well with LoC approaches by researchers in the last years. Here, different concepts where the cells either adhere on a flat surface or are embedded in a matrix have been investigated for individual applications such as 3D-cell cultures or for organs-on-a-chip based on the cocultivation of different cell types. Furthermore, the monitoring of the cells is published for various parameters

together with different approaches like amperometric and luminescent concepts to measure the concentration of dissolved oxygen in cell cultures.

Though, there is a huge gap between LoC-systems for cell applications described in the literature and the systems that are actually used by biological or medical researchers. The main reason might be the complexity of the novel concepts, in which a few problems are solved by sophisticated methods while other issues remain unsolved. This includes for example the bulky and expensive external equipment such as incubators, pumps or control units. Furthermore, the vast majority of the devices is based on PDMS, which is not suited for mass production and is also problematic due to its porosity and the cytotoxic components. Thus, further research is required until the on-chip cell cultivation and cell analysis meets all requirements of the end-users.

3 On-chip Cultivation of Mammalian Cells

The cultivation of mammalian cells inside a microfluidic chip is an important process for many applications in pharmaceutical research. This chapter presents such a device for the long-term cultivation of mammalian cells which could be used as a platform for Lab-on-a-Chip. Nowadays, the gold standard of cell cultivation are culture flasks, well-plates and petri dishes. As a consequence, the main emphasis of such a microfluidic chip is the miniaturisation of these devices, which means that the chip has to fulfil the following properties:

- long-term cultivation (i.e. longer than 24 h)
- universal design that allows the cultivation of a variety of mammalian cells
- 2D-cell culture (an setup for 3D-cell cultures is though given in sec. 3.5.4)

Based on these aims, the requirements for such a device are analysed in sec. 3.1. Two concepts that fulfil the requirements are presented in sec. 3.2, followed by an overview about porous membranes in sec. 3.3. Subsequently, the implementation of these concepts including the design of the chips, the fabrication steps and the design of the assemblies are given in sec. 3.4. The experiments and the results with both chips are described in sec. 3.5. Both concepts are compared in sec. 3.6 and conclusions are given in sec. 3.7. In sec. 3.8, an outlook is present on future improvements.

The presented concepts and results have been published in parts in the following journal papers and conference proceedings:

- F. Bunge, S. van den Driesche, M. J. Vellekoop. Symmetric surficial phaseguides: a passive technology to generate wall-less channels by two-dimensional guiding elements. *Microfluidics and Nanofluidics*, 20(7), 2016 [12]
- F. Bunge, S. van den Driesche, M. J. Vellekoop. Microfluidic platform for the long-term on-chip cultivation of mammalian cells for lab-on-a-chip applications. *Sensors*, 17(7):1603, 2017 [14]
- S. van den Driesche, F. Lucklum, F. Bunge, M. J. Vellekoop. 3D printing solutions for microfluidic chip-to-world connections. *Micromachines*, 9(2):71, 2018 [105]

- F. Bunge, S. van den Driesche, M. J. Vellekoop. Hydrophobic self-assembled monolayers as guiding structures for agarose hydrogels in microfluidic chips. *Proc. μ TAS*, Korea, 2015 [10]
- F. Bunge, S. van den Driesche, M. J. Vellekoop. Gas supply through agarose walls in cell culturing microchips. *Advances in Science and Technology*, 100:115-119, 2016 [11]
- F. Bunge, S. van den Driesche, M. J. Vellekoop. Easy-to-use microfluidic chip for long-term 3D-cell cultures. *Proc. SPIE*, Spain, 2017 [13]
- F. Bunge, C. Habben, S. van den Driesche, M. J. Vellekoop. A novel on-chip element to provide mammalian cell cultivation and passaging to Labs-on-Chips, *Proc. IEEE Transducer*, Taiwan, 2017 [15]
- S. Reede, F. Bunge, M. J. Vellekoop. Integration of Silica Aerogels in Microfluidic Chips, *Proc. Euroensors*, France, 2017 [87]
- F. Bunge, C. Habben, S. van den Driesche, M. J. Vellekoop. Integration and characterization of nanoporous aluminium oxide membranes in microfluidic chips. *Proc. IEEE MEMS*, 2018 [9]

The concept and the experiments of silica aerogels in sec. 3.3.3 have been realised during a master project by Sina Reede that was supervised by the author.

3.1 Requirements

The aim of this section is to analyse the requirements for the design of a microfluidic chip for long-term cultivation of mammalian cells. The basic characteristic of mammalian cells is their metabolism. As a simplification, they take up oxygen, glucose and pyruvate and convert it into carbon dioxide, ammonium and lactate. The metabolism is influenced by the physical environment, such as used materials, temperature and pH-value of the surrounding liquid, but also by the biochemical environment like proteins, vitamins and salts. These parameters and the subsections, in which they are discussed, are summarised in fig. 3.1.

The chip shall be able to cultivate a large variety of mammalian cells which usually have different requirements. Here, the requirements and the design are investigated for MDCK cells that are often used as a model for other cells types. Consequently, the general results are also valid for other cell types.

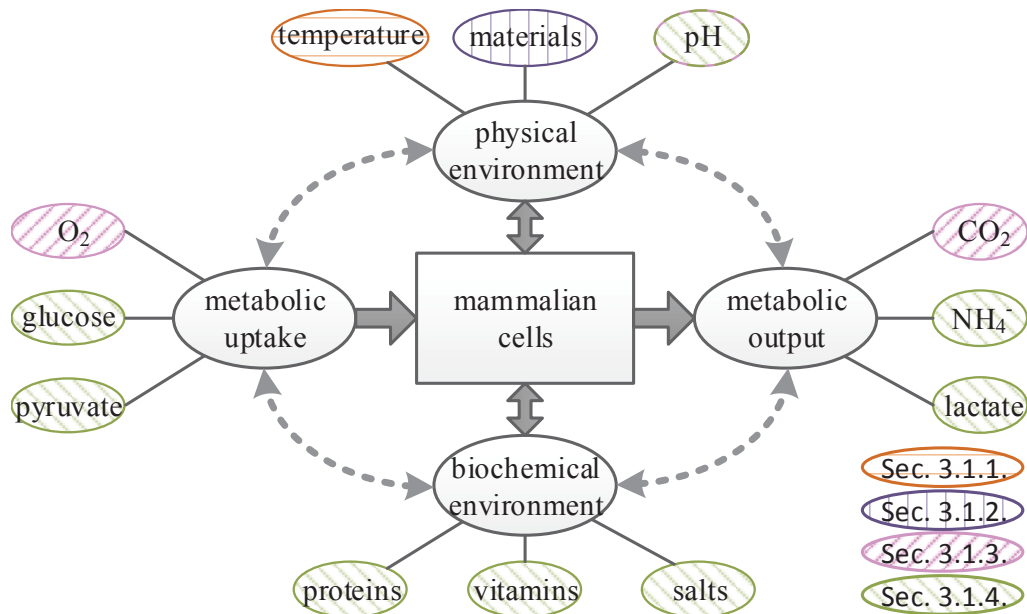


Figure 3.1: Overview about the main parameters that influence the cell growth and the section, in which they are discussed further.

3.1.1 General requirements

Dimensions

Labs-on-a-Chip require significantly less cells than common cell analysis methods. However, depending on the cells and on the investigated parameters, between 1000 and 50.000 cells are necessary to get reliable measurement results. Assuming that a cell is $20 \times 20 \mu\text{m}^2$ and 50 % of the area is covered, up to 1200 cells can be cultured on 1 mm^2 . As a consequence, the cell culture chamber should have a size of several mm^2 .

Optical inspection

The most common method to evaluate the cell growth is the optical inspection through a microscope. Consequently, either the top or the bottom of the chip has to be transparent (ideally both plates). Many other optical inspection methods are based on fluorescence. Therefore, the chip itself must not interfere with the measurements e.g. by fluorescence of the materials.

Transfer options

Obviously, the cells need to be inserted into the chip. Additionally, it is very useful for further analysis if the cells can be removed alive from the device after cultivation. This means that microfluidic cell cultures, in which the cells are embedded in a matrix, like cell-laden hydrogels [76] or 3D-cell cultures [50], are not suitable for the targeted device because cell harvesting is not possible. The same is valid for cell

encapsulation inside small hydrogel spheres [67]. Here, the hydrogel spheres with the cells can be removed from the chip but it is difficult to release the cells from the hydrogel. In contrast, adherent cell cultures usually allow the detaching of cells e.g. by enzymes.

Temperature

The growth and proliferation of mammalian cells depend strongly on the temperature. Obviously, the cultivation temperature depends on the application and the cell type. However, most mammalian cells show the highest growth rates at 37 °C either because their in-vivo temperature is also 37 °C (e.g. human cell lines) or because the cell lines are adapted to this temperature.

Usually, mammalian cells are able to survive lower temperatures like 20 °C for several hours but exhibit a significantly reduced growth rate and lower metabolism. In contrast, even short periods with slightly increased temperatures like 3 K more than the standard temperature might kill the entire cell culture. To sum it up, mammalian cells require constant temperatures above room temperature (usually 37 °C) for optimal growth while even higher temperatures must be avoided. [65]

3.1.2 Choice of materials

The chip should be designed in a way that the mammalian cells grow as good as in a conventional culture flask. According to ISO 10993-5, a material is claimed as non-reactive regarding the cytotoxicity if cell growth is not reduced, no cell lysis and no detectable zone with a change of size or appearance of the cells of is visible after 24 h. Every material of the entire assembly that is in contact with the cells or the cell medium must be non-cytotoxic or special measures like coatings have to be taken. Additionally, the bottom plate of the chamber has to allow adhesion of the cells.

Furthermore, the materials must not absorb ingredients of the culture media to avoid unknown concentrations and increased response times when the medium is changed. As mentioned in sec. 3.1.1, the top and / or bottom plate have to optically transparent and ideally not fluorescent.

Last but not least, the microfluidic chip should be fabricated with clean room technologies to enable low fabrication costs in case of mass production. Consequently, all materials have to be compatible with standard MEMS processes.

The mentioned requirements are fulfilled by e.g. hard materials such as glass and silicon. At the moment, almost all microfluidic chips for the long-term cell cultivation are based on polydimethylsiloxane (PDMS) for at least one layer of the chip. PDMS is permeable to gases (see also sec. 3.1.3) so that additional gas supply

structures are not necessary. Furthermore, it is easy to fabricate at low costs for small lot sizes because it is basically a mould process where the liquid PDMS is poured over a stamp. Subsequently, the oligomers are crosslinked by high temperatures or chemical crosslinkers to become solid.

However, up to 5% w/w of the reactive oligomers remain unlinked. These oligomers which are cytotoxic diffuse into the cell medium and impair the cell growth. Furthermore, PDMS also absorbs small hydrophobic molecules like estrogen which is an important hormone. In case of estrogen, up to 90% might be absorbed, which lower the concentration in the medium tremendously [41, 88]. Additionally, fluorescent molecules like Nile Red are absorbed as well and PDMS has slight background fluorescence so that fluorescent measurements are also affected [52, 93]. *Sackmann et al.* concluded that the "often cited biocompatibility of PDMS appears to be something of a misnomer" [92]. Therefore, PDMS is completely avoided in favour of the mentioned hard materials for the presented chips.

3.1.3 Supply with gases

Oxygen consumption

Mammalian cells need oxygen for their metabolism and produce carbon dioxide. Therefore, the microfluidic chip has to supply the cells constantly with new oxygen. The oxygen consumption rate (OCR) depends mainly on the cell type and varies between $1 \frac{\text{amol}}{\text{cell s}}$ and $350 \frac{\text{amol}}{\text{cell s}}$ while most cells are in the range of 10 to $50 \frac{\text{amol}}{\text{cell s}}$. The OCR correlates with the cell volume and protein mass which means that larger cells consume more oxygen. Furthermore, the OCR is much higher during the exponential growth phase in the beginning of the culture compared to the plateau phase later on (almost no cell growth). [112]

The cells are covered with culture media, meaning that the oxygen has to be dissolved in the solution. The solubility of oxygen depends strongly on the temperature and on the ionic strength. In case of 37 °C and an ionic strength of 200 mM, the solubility is approximately $200 \mu\text{M} = 200 \times 10^9 \frac{\text{amol}}{\text{mL}}$. Considering that common cell densities are in the range of $1 \times 10^6 \frac{\text{cell}}{\text{mL}}$ in the microfluidic chip, the dissolved oxygen is consumed within the order of 1 h.

The oxygen uptake depends also on the oxygen concentration in the medium and can be described with the Michaelis-Menten-kinetics:

$$\text{OCR}(c_{\text{O}_2}) = \frac{\text{OCR}_{\text{max}}}{\frac{K_{m,\text{O}_2}}{c_{\text{O}_2}} + 1}, \quad (3.1)$$

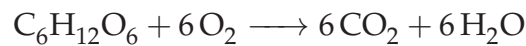
where OCR_{max} is the maximal OCR, c_{O_2} is the concentration of dissolved oxygen and K_{m,O_2} is the Michaelis-Menten-constant for the oxygen consumption. For

different cell types, K_{m,O_2} is in the range of 1 μM . Hence, the oxygen uptake is reduced by 50% when the concentration is as little as 1 μM . However, the OCR equals almost the maximal value for concentrations of 10 μM . As a consequence, the OCR is almost independent of the oxygen concentration unless concentrations are very low. [112]

To sum it up, the OCR of mammalian cells depend on many parameters but the dissolved oxygen in the medium is consumed within the order of 1 h. As a consequence, the constant supply of oxygen to the cells is indispensable.

Carbon dioxide

As part of the metabolism, the cells produce carbon dioxide while oxygen and glucose is consumed:



In doing so, the same amount of CO_2 is produced as O_2 is consumed which is usually in the range of 10 to 50 $\frac{\text{amol}}{\text{cells}}$. When CO_2 is dissolved in water, it forms carbonic acid and thus changes the pH-value. Therefore, the culture medium usually contains sodium bicarbonate (concentration 3.7 $\frac{\text{g}}{\text{L}}$) to form a pH-buffer. That ensures that culture medium usually has physiological pH-values if it is stored with air containing 5 to 10% CO_2 .

The solubility of CO_2 is 1.1 mM at 37 °C and a partial pressure of 0.05 atm. When the gas exchange to the air is avoided and the entire dissolved oxygen (i.e. 200 μM) is consumed by the cells, the carbon dioxide concentration increases by 200 μM or 18%. That results in a rise of the pH-value by only 0.07. On one hand, that shows the necessity to continuously remove the produced CO_2 to keep the pH-value stable. On the other hand, the removal of CO_2 is less important than the supply with oxygen due to its lower solubility.

3.1.4 Supply with nutrients

Mammalian cells are cultivated in special cell medium which is often Dulbecco's modified Eagle medium (DMEM) that is enriched with 10% v/v fetal bovine serum (FBS) and optional with 0.5% v/v antibiotics (usually Penicillin-Streptomycin). The DMEM medium contains various ingredients like seven different inorganic salts, seven vitamins, 15 amino acids as well as glucose and sodium pyruvate as energy sources [73].

The cell metabolism consists of several steps. In a simplified pathway, the glucose is enzymatically reduced at first to pyruvate and subsequently to lactate (so-called glycolysis). Afterwards, the lactate is consumed in the mitochondria while O_2 is

taken up and CO₂ and water are produced. In contrast to cells inside the body, the glycolysis dominates in in-vitro cell cultures which is the so-called Crabtree-effect [69]. Consequently, the OCR is lower than the glucose consumption rate. As an example, MDCK cells consume approximately $250 \frac{\text{amol}}{\text{cell s}}$ glucose [97] but only $20 \frac{\text{amol}}{\text{cell s}}$ oxygen [112]. Assuming a cell density of $1 \times 10^6 \frac{\text{cell}}{\text{mL}}$ and a common glucose concentration of $4500 \frac{\text{mg}}{\text{L}}$ (=25 mM), the glucose is consumed within 28 h.

During the glycolysis, lactate and ammonium ions are produced which diffuse into the cell medium. Lactate concentrations up to 20 mM do not affect the cells while concentrations above 40 mM inhibit the cell growth. Ammonium ions have a much stronger impact as already low concentrations of 2 mM impair the cell growth [2]. In case of MDCK cells, the lactate production rate was determined as $490 \frac{\text{amol}}{\text{cell s}}$ and the ammonium production rate as $11 \frac{\text{amol}}{\text{cell s}}$ [97]. Consequently, the acceptable limits (i.e. that do not impact the cell growth) for lactate and ammonium are reached after 11 h and 50 h, respectively.

Beside the cell metabolism, the proliferation of the cells also consumes nutrients. Basically, the carbon in cells originates partly from the glucose. Additionally, the cells need glutamine, which is an amino acid, for growth [80]. Glutamine is used mainly to form proteins which consists also of other amino acids. However, the consumption rates of these molecules differ between each cell type and depend as well on the culturing conditions [45].

The culture medium has to be exchanged after several hours according to the estimations above in contrast to conventional cell cultures where exchange intervals are usually two or three days. An easy method for microfluidic cell cultures is the continuous or discontinuous perfusion with fresh medium. Due to the viscosity, perfusion results in shear stress of the attached cells which influences growth and functioning of almost all cell types but in different ways. In general, mammalian cells align in the direction of the flow [42]. Stem cells differentiate differently compared to stress-free conditions [98]. *Burghoff et al.* described that human endothelial cells produce 327 proteins under laminar shear stress compared to 507 proteins under oscillating stress and 395 under static conditions [18]. To sum it up, there are various effects which might be advantageous or disadvantageous depending on the application and obviously correlate with the magnitude of the shear stress.

The majority of cell cultivation is still carried out in conventional culture plates without any shear stress. In this chapter, the aim is to miniaturise this gold standard of cultivation to a microfluidic chip. Consequently, this chip shall avoid shear stress as well, which means that continuous perfusion is no option. An attractive alternative are diffusion processes that benefit of the small dimensions in microfluidic devices. Diffusion is reliable, continuous and does not result in any

shear stress on the cells. Therefore, the exchange of the cell medium shall be based on diffusion.

3.2 Concept

Based on the requirements of sec. 3.1, two concepts for the cell cultivation in a microfluidic chip are investigated and realised, which differ by the arrangement of the supply structures around the cultivation chamber. In the horizontal concept (sec. 3.2.1), the supply structures are arranged horizontally around the cell growth chamber and are separated by vertical membranes. In the vertical concept in sec. 3.2.2, the supply channel is under the culture chamber so that the cells are supplied vertically through a horizontal membrane.

3.2.1 Horizontal supply concept

In the horizontal supply concept as shown in fig. 3.2, the chip contains a microfluidic chamber in which the cells grow [14, 15]. This chamber is connected to an inlet and an outlet that allows the filling and removal of the cells. Furthermore, two channels are arranged on each side of the chamber. One channel is used to supply

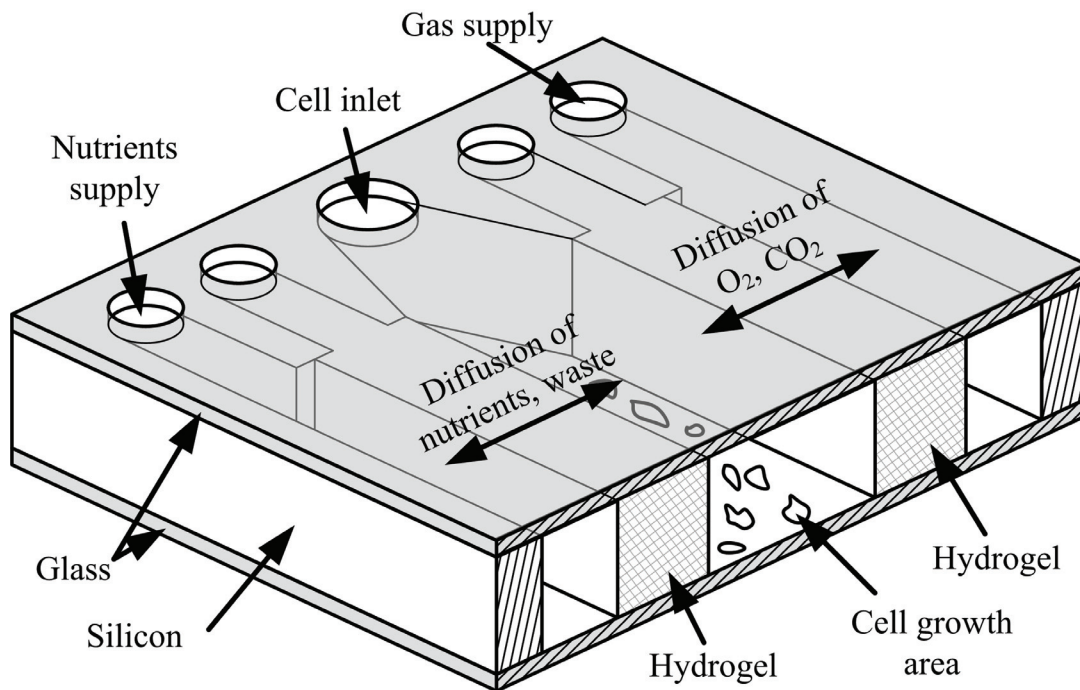


Figure 3.2: Cross-section of the microfluidic chip for the cultivation of mammalian cells with horizontal supply structures. The other half of the chip is identical to the shown structures.

the chamber with fresh medium and to remove the products of the metabolism. The other channel supplies the chamber with gases like oxygen and carbon dioxide. The separation of the channels and the chamber is realised with porous walls through which gases and nutrients can diffuse continuously. These walls should avoid leakage of the medium into the gas channel but also avoid perfusion of the cells with fresh cell medium. An attractive material for these porous membranes are hydrogels because of their high porosity, biocompatibility and their ability to form vertical, but permeable membranes inside closed microfluidic devices [83].

As the gas supply is integrated into the chip, hard materials like glass and silicon can be used for the fabrication. These materials are biocompatible and non-cytotoxic but also allow the usage of common microfluidic fabrication technologies. Glass is used as bottom and top plate allowing easy optical inspection, while the solid walls are made out of silicon.

3.2.2 Vertical supply concept

In the vertical supply concept, the porous membrane is arranged horizontally under the culture chamber (see fig. 3.3). In order to keep the design relatively simple, a second membrane is not considered here. Consequently, either nutrients (referred to as nutrient diffusion) or gases (referred to as gas diffusion) can diffuse through the membrane towards the cells. [9]

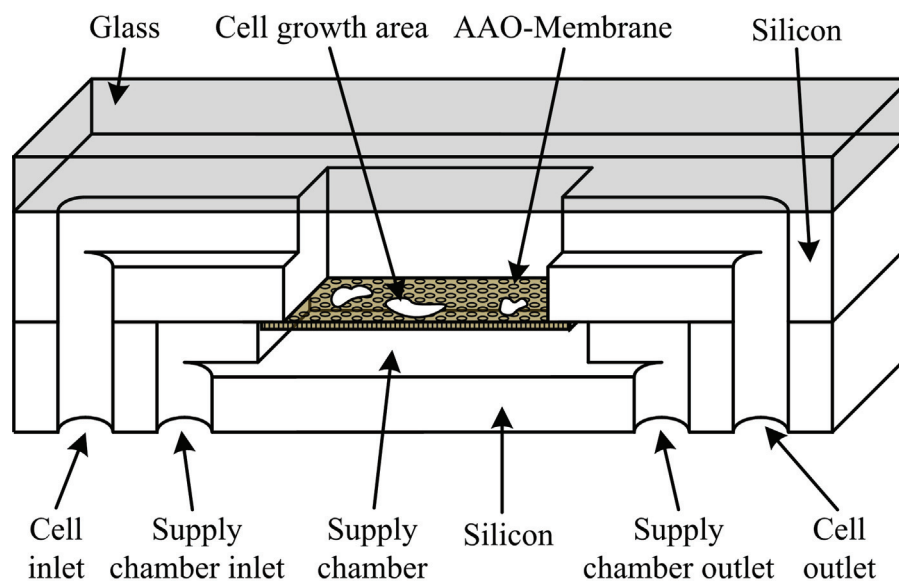


Figure 3.3: Cross-section of the microfluidic chip for the cultivation of mammalian cells with vertical supply. The other half of the chip is identical to the shown structures.

In case of the nutrient diffusion, the culture medium is pumped through the second chamber and the nutrients and the metabolic products are exchanged constantly through the membrane. This membrane needs a high porosity in order to achieve high exchange rates but small pores to eliminate the flow between both chambers and thus shear stress. As there is no second membrane for the gas, the cells can be supplied with oxygen that is already dissolved in the medium. However, most culture media are made for traditional cell cultures in the incubator and thus contain a sodium bicarbonate buffer that requires a high concentration of CO₂. Therefore, either a standard medium, where enough CO₂ and O₂ are dissolved, or a special medium for a CO₂-free culture system has to be used.

In case of the gas diffusion, the second chamber is filled with gas containing O₂ and CO₂. In doing so, the cells are supplied continuously and directly with the gases that are provided either from an incubator or from an external gas source. The culture medium in the chip has to be exchanged regularly to remove the metabolic products and to supply fresh nutrients. In this case, the membrane must be permeable for gases but must avoid leakage that would otherwise cause a filling of the second chamber.

An attractive material for the horizontal membrane of the gas and nutrient supply concepts is porous anodised aluminium oxide (AAO)¹. In this membrane, the pores are formed unidirectional during the anodisation with pore sizes in the range of nm. Furthermore, AAO is non-cytotoxic and used in other applications as interface to mammalian cells as well [7]. AAO is hydrophilic so that the pores are filled automatically with liquids. However, it requires a high pressure to press liquid out of the pores because the pores are orthogonal to the flat membrane surface. Consequently, leakage is avoided which is important for the gas diffusion. In addition, it is also mechanically and thermally stable and can thus be integrated monolithically in closed microfluidic devices. To use only non-cytotoxic materials, the chip consists of a glass layer to allow optical inspection and two layers of silicon.

3.3 Porous membranes

The horizontal and vertical concepts require the integration of at least one porous membrane. The horizontal supply concept is based on porous membranes out of hydrogel. These hydrogels are presented and characterised in sec. 3.3.1. The vertical supply concept contains a membrane of porous anodised aluminium oxide that is described in more detail in sec. 3.3.2. An alternative to the hydrogels are silica

¹A comparison with other porous materials is given in sec. 3.3.2.1.

aerogels that can be used for horizontal and vertical membranes as presented in sec. 3.3.3. Finally these porous materials are compared in sec. 3.3.4.

3.3.1 Hydrogels as porous walls

Hydrogels are a group of porous materials, in which the pores are filled with water. Their properties are described at first in sec. 3.3.1.1. An attractive integration method is the application of surficial phaseguides which is presented in sec. 3.3.1.2.

3.3.1.1 Properties of hydrogels

Hydrogels are materials which contain a 3D-crosslinked network of hydrophilic polymer chains. The crosslinked polymer is not soluble so that the network might retain water. The maximal water content depends on the hydrogel but usually varies between 20 % and 99 % [26]. Their origin might be natural (e.g. collagen or agarose) or synthetic (e.g. polyethylen-glycol). As hydrogels are a variety of polymers, the properties also vary tremendously. Some hydrogels respond to external effects like changes in temperature [27] or pH [37] by swelling which could be used for sensors. The pore sizes vary between the nanometer range [4] and several micrometer [40] depending on the type of hydrogel and the fabrication method.

The gelation, that is the formation of a solid gel by crosslinking the polymers, is based either on chemical, photo or thermal polymerisation [25]. The chemical polymerisation requires the mixture of two components with complementary groups or enzymes to start the reaction in which covalent interactions are formed. Typical chemical gels are made out of alginate. Although these gels are attractive due to their high stability, the chemicals might react with other substances and the formation of such gels at predefined locations inside a microfluidic chip is difficult to control. [26]

Photo-polymerised hydrogels require the addition of a photoinitiator that initialises the crosslinking of the polymer by absorbing light. Common gels are based on polyethylen glycol or polyethylen glycol diacrylate. These gels are attractive for microfluidic chips because the gelation can be easily controlled and even patterns are possible by using a photolithography process. Various photoinitiators are cytotoxic unless very low concentrations below 0.02 % w/w are used. However, such low concentrations restrict the crosslinking so that photo-polymerised hydrogels are considered as poorly suited for cell cultivation. [8, 33, 67]

Physical crosslinking is usually triggered by temperature changes and results in non-covalent bindings that are mechanically weaker than chemical or photo-crosslinked hydrogels. For example, 1 % w/w agarose (Type I) in water melts at approximately 65 °C and remains liquid until it is cooled below its transition

temperature around 30 °C where the gelation occurs. There are different types of agarose commercially available that all have different transition temperatures. The advantage of thermal hydrogels is the high biocompatibility due to the absence of toxic chemicals or photo crosslinkers [26, 44]. Consequently, these gels are very appealing for cell cultivation purposes in which all nutrients diffuse through the hydrogel. [61, 76]

The mechanical properties of agarose hydrogel depend on the thermal history among other factors like the concentration. Faster cooling results in higher Young's modulus which are up to 80 kPa for 2 % w/w agarose for low deflections and up to 200 kPa for high deflections with a failure strain of around 40 % [4]. The Young's modulus also rises with increasing concentrations of the agarose. [120]

The pore sizes of agarose vary but are in the order of 100 nm [4]. Increasing the agarose concentration results in lower pore diameter [77]. *Ling et. al* showed that the hydrogel allows sufficient diffusion of nutrients for the cultivation of mammalian cells that are embedded inside the agarose network [61]. The diffusion coefficient can be significantly increased by creating macropores of 200 μm . This can be achieved by adding high concentrations of sucrose before the gelation and dissolving them afterwards [76].

3.3.1.2 Integration based on symmetrical surficial phaseguides

Thermal hydrogels as described in sec. 3.3.1.1 are an ideal choice for porous membranes. The horizontal concept (see 3.2.1) requires two membranes in predefined areas. Therefore, the liquid hydrogel must fill only these areas prior to gelation. When entering the chip, hydrogel is surrounded with solid plates on the floor and ceiling and two empty chambers on each side which are filled later with the culture medium. As there is no solid wall between the liquid hydrogel and these empty chambers, the channel of the hydrogel is considered as a wall-less channel.

One method to create a wall-less channel within a closed microfluidic chip is the application of phaseguides [10, 12, 110]. Phaseguides are elements that are patterned on the bottom or the top plate and which require a higher capillary pressure for liquids to flow over. Liquids always propagates in the direction of the lowest pressure so that the melted hydrogel flow along the phaseguides instead of flowing over them. Consequently, common applications of phaseguides in microfluidic chips are the controlled filling, partially filling and emptying.

This property of higher capillary pressure at predefined locations can be achieved either by special geometries (i.e. geometrical phaseguides) [82, 111] or by using a different material (i.e. surficial phaseguides) [12, 22, 110]. Geometrical phaseguides are barriers with a rectangular cross-section which are either on the bottom or on

the top plate. The height of this barrier is usually about 25% of the total height of the channel [111]. As a consequence, the diffusion of compounds, which is the aim for the presented application, is lowered by the phaseguide because the effective diffusion area is reduced by the barrier. Furthermore, geometrical phaseguides are robust and easy to integrate in a device made out of polymers like SU8 or PDMS but not with hard materials as required for the presented concept (see sec. 3.1.2).

Surficial phaseguides are based on different materials with different wetting properties [22, 110] which are patterned on the top and / or bottom plate of the chip. As this is compatible with hard materials by using standard clean room technologies and enables maximal cross-section areas for the diffusion, surficial phaseguides fit very well to the requirements .

When a liquid is inserted between two identical plates, its interface to air forms a meniscus. The shape of the meniscus depends on the relative pressure within the liquid and on the contact angle. If the surface is hydrophilic, the contact angle θ_{gl} is below 90° meaning that the meniscus has a concave shape (see meniscus (I) in fig. 3.4). This concave shape results in a negative capillary pressure so that the liquid propagates further into the chip. If the surface is hydrophobic, the shape of the meniscus is convex (contact angle $\theta_{odt} > 90^\circ$). Thus, the pressure inside the liquid is positive meaning that the surface repels the liquid (meniscus (V) in fig. 3.4). The boundary between the hydrophilic and the hydrophobic surface is special because any contact angle θ_b with $\theta_{gl} \leq \theta_b \leq \theta_{odt}$ is possible depending on the applied pressure. Therefore, the shape of the meniscus is either concave, straight or convex (meniscus (II) - (IV) in fig. 3.4).

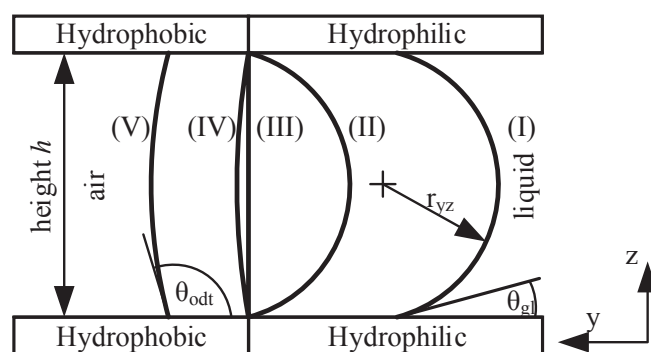


Figure 3.4: Sketch of different menisci (air is on the left of the meniscus and the liquid on the right) between two plates depending on the surface properties of a symmetrical top and bottom plate in the y - z -plane: (I) concave shape between two hydrophilic surfaces, (II) - (IV) concave, straight or convex shape at the boundaries between hydrophilic and hydrophobic surfaces depending on the applied pressure, (V) convex meniscus between two hydrophobic plates. [12]

The capillary pressure p of a liquid near the air-liquid interface is determined as:

$$p = \sigma \left(\frac{1}{r_{xy}} + \frac{1}{r_{yz}} \right), \quad (3.2)$$

where σ is the surface tension and r_{xy} and r_{yz} the radii of the curvatures of the surface. Here, the radii are defined as positive in case of a convex shape of the meniscus and negative for a concave shape. If the contact angles θ on both plates of the channel with the height h are identical, r_{yz} is found as

$$r_{yz} = -\frac{h}{2 \cos \theta}. \quad (3.3)$$

If the channel is straight in x-direction, the radius r_{xy} equals infinity and thus $\frac{1}{r_{xy}} = 0$. So, the capillary pressure of water with $\sigma = 72.75 \times 10^{-3} \frac{\text{N}}{\text{m}}$ in such a channel equals

$$p = \frac{2\sigma \cos \theta}{h}, \quad (3.4)$$

so that $p_I = -378 \text{ Pa}$ between hydrophilic glass plates surfaces ($\theta_{gl} = 16^\circ$ and $h = 380 \mu\text{m}$) and $p_V = 86 \text{ Pa}$ between hydrophobic surfaces ($\theta_{odt} = 103^\circ$). Thus, the liquid flows over a straight hydrophobic phaseguide if $p > 86 \text{ Pa}$, while the filling of the chip results in negative pressure.

3.3.2 Porous anodised aluminium oxide

The vertical supply concept is based on a horizontal membrane out of porous anodised aluminium oxide (AAO). At first, different porous materials that would be suited for the concept are compared in sec. 3.3.2.1. Subsequently, the pore formation for AAO is described in more detail (sec. 3.3.2.2) and finally, the main properties of this membrane are presented in sec. 3.3.2.3. [9]

3.3.2.1 Comparison of different porous materials

There is a wide range of different materials for porous membranes which can be categorised in three groups. The first group are polymer membranes such as cellulose acetate with a random network of pores that are formed by evaporation of the solvent. However, these membranes have a wide distribution of pore sizes and can be integrated into a chip only by clamping. A similar approach are track-etched polymer membranes. In this case, the pores are formed by irradiation with ions resulting in a narrow distribution of the pore size but a low porosity. Yet, the integration of these membranes is also based on clamping or thermal bonding to

other polymers and thus only poorly compatible with clean room technologies [114].

The second group are silicon nitride membranes which are the most common membranes in microsystems. Silicon nitride is formed by chemical vapour deposition before the silicon underneath is removed by etching. The pores can be formed either by E-beam lithography, track-etching or deep-UV-lithography in combination with dry-etching. Such a membrane is biocompatible and chemically and mechanically stable. Nevertheless, the aspect ratio, which is the ratio of the membrane thickness to the pore diameter, is limited resulting in either thin membranes or large pores. Additionally, the fabrication process for the pore formation requires high efforts and costs e.g. for E-beam lithography or for deep-UV-lithography. [48]

The third relevant group of materials are electrochemically anodised membranes. This process is mostly used for the formation of porous silicon and porous anodised aluminium oxide (AAO). The advantages of these materials are the monolithic integration and the easy control of the pore dimensions by adjusting the voltage or the current density. Silicon is anodised in hydrofluoric acid that is much more dangerous and thus disadvantageous compared to the anodisation of aluminium e.g. in oxalic acid. [43]

In conclusion, anodised aluminium oxide can be easily integrated into the chip and is fabricated with less efforts, costs and risks and better control of parameters compared to other materials. Therefore, AAO is chosen as membrane material for the vertical supply concept.

3.3.2.2 Formation of pores by anodisation of aluminium

The formation of the pores is based on a self-ordering electrochemical process as shown in fig. 3.5. The wafer, which consists of a bottom layer, e.g. out of silicon, and aluminium on top, is placed in an electrolyte (fig. 3.5(a)). Once a voltage is applied, a thin but uniform oxide layer is formed on top of the aluminium (fig. 3.5(b)). The surface roughness and local defects result in an inhomogeneous distribution of the electric field. At spots with focussed electric field, the oxide is dissolved and the formation of the pores begins (fig. 3.5(c)). Subsequently, the pores grow further due to the focussing of the electric field at the bottom of the pores. At this stage, the ions (Al^{3+} and O^{2-}) migrate through the oxide with approximately $1 \frac{\text{nm}}{\text{V}}$ while AAO is dissolved at the bottom of the pore. The mechanical stress of the volume expansion and the distribution of the electric field result in a self-ordering mechanism of the pores to arrange them in a hexagonal pattern. Consequently, the distance between the pores depends mainly on the applied voltage (fig. 3.5(d)) [46]. Once the entire aluminium is anodised, the pore growth stops so that the pores are open only at

the anodised side but not at the bottom (fig. 3.5(e)). In order to fabricate porous membranes, the bottom layer has to be removed by dry or wet-etching (fig. 3.5(f)). Finally, the pores are opened by wet-etching in phosphoric acid, that etches AAO. This step can be used to further widen the pores if desired. [49]

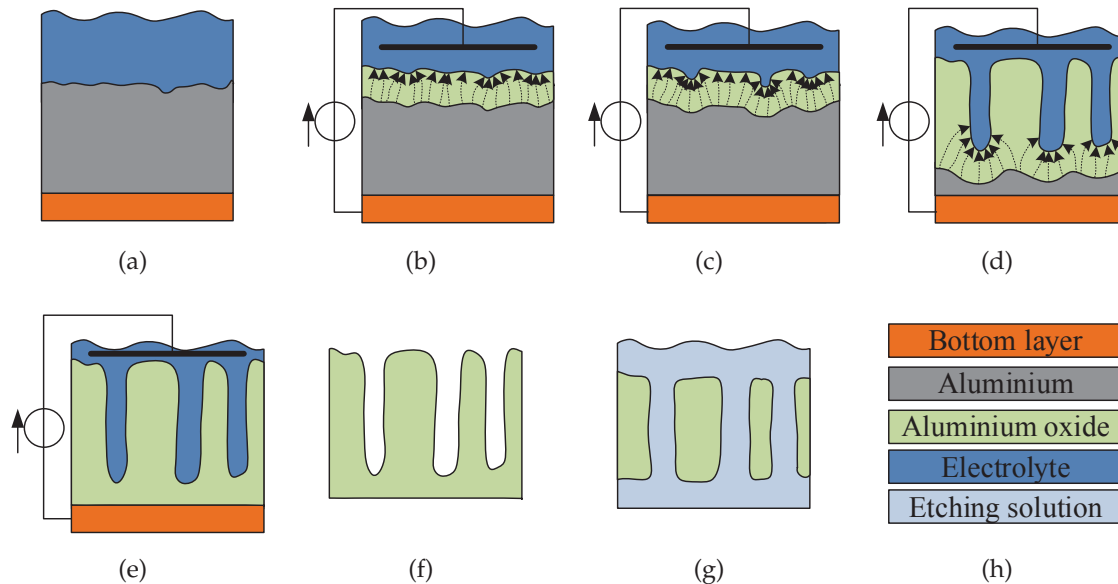


Figure 3.5: Principle of the pore formation during the anodisation of aluminium: (a) initial situation (b) formation of a thin AAO layer after applying a voltage (dotted arrows represent the electric field) (c) beginning of the pore formation at local defects (d) pore growth (e) end of the pore formation (f) removal of the bottom layer by dry or wet-etching (g) opening of the pores by wet-etching of AAO (h) legend.

The properties of the membrane are influenced by the process parameters as discussed below:

Temperature

Higher temperature values during the anodisation enhance the current densities and thus accelerate the anodisation (e.g. increasing the temperature from 20 °C to 30 °C doubles the speed). Furthermore, more AAO is dissolved resulting in bigger pore diameters. However, the inner pore distance, which is the distance between the centre of two neighbouring pores, is not influenced. [99]

Voltage

During the anodisation, the aluminium and the oxygen ions diffuse through the oxide. The maximal width of this diffusion increases with the voltage. Therefore, higher voltages result in wider regions of anodisation and therefore higher distances between the pores. In this case, the ratio of the pore distance to the voltage is

approximately $2 \frac{\text{nm}}{\sqrt{V}}$. In addition, more aluminium oxide is dissolved in higher electric fields than in lower. Consequently, the pores are wider at high voltages than at low voltages. By varying the voltage during the anodisation, the pore diameter might either change along the pore axis or the pore might even branch into smaller pores. [59]

Electrolyte

Aluminium can be anodised in various electrolytes like sulphuric acid, oxalic acid or phosphoric acid. The maximal voltage for the anodisation is limited by the "burning", which is a strong gas bubble formation due to very high current densities and which damages the membrane. This maximal voltage depends mainly on the electrolyte and is e.g. around 30 V in sulphuric acid and 200 V in phosphoric acid. Furthermore, higher concentrations of the electrolyte result in better ordering processes because of higher current densities. However, too high concentrations reduce this effect if the viscosity is too high. [74]

Surface preparation

The pore growth starts at local defects like concave spots or preformed pores. Consequently, very smooth surfaces, e.g. by electropolishing, result in a more uniform (hexagonal) arrangement of the pores. This effect can be even amplified by a two-step anodisation. In that case, the anodised aluminium oxide of the first step is removed by wet-etching which results in a very regular pattern of low pores under the barrier layer. The rest of the aluminium is anodised subsequently and a regular hexagonal pattern is formed.

3.3.2.3 Properties of anodised aluminium oxide

As already mentioned, AAO has a high porosity that might vary between 15 and 50%. The inner pore distance can be adjusted between 20 and 500 nm [49]. Furthermore, the pores are usually positively charged due to the anodisation process. As a consequence, negatively charged ions diffuse faster through the membrane than their positive counterparts. As an example, the diffusion coefficient of Cl^- is 2.2 times higher than its equivalent of Na^+ for pores with a diameter of 46 nm and a length of $63 \mu\text{m}$ [90].

Aluminium oxide resists all organic solvents and most acids except phosphoric acid and hydrofluoric acid. However, it is etched by bases which are e.g. part of the developers of photoresist. Furthermore, this material is thermally extremely resistant because of its high melting point above 2000°C . Last but not least, AAO is also mechanically stable with a very high Young's modulus of approximately

3000 GPa. If a thin pillar of AAO with pores in axial direction is formed, the maximal compressive stress is up to 1700 MPa before buckling occurs [71]. In addition, a porous membrane of 1 μm thickness and a diameter of 1 mm is stable up to 75 kPa with a flow rate through the pores (200 nm wide) of $3 \frac{\text{mL}}{\text{bar min cm}^2}$ [101].

AAO is optically transparent with optical transmission of more than 90% in a wavelength range of 300 to 900 nm for a pore diameter of 60 nm [121]. In contrast to aluminium that is cytotoxic, AAO is biocompatible. Various mammalian cells also adhere on AAO or at least if the surface is coated with proteins [7].

Usually, AAO has a very flat surface apart from the pores that are orthogonal to the surface. As aluminium oxide is hydrophilic, the pores are filled with water immediately after contact because of the capillary effect. Once the liquid (here: water) is pressed out of the pore, a convex meniscus is formed (see fig. 3.6) with the radius r with

$$r = \frac{d_p}{2 \sin \theta}, \quad (3.5)$$

where d_p is the pore diameter and θ is the contact angle of water on AAO. As a consequence, the capillary pressure p to press water out of the pore equals

$$p = \frac{4\sigma \sin \theta}{d_p}, \quad (3.6)$$

where σ is the surface tension. Assuming a pore diameter of 50 nm and a contact angle of 10° , the required pressure is in the order of 1 MPa. Obviously, a concave surface, larger pore diameter or even lower contact angles would reduce this pressure. The actual contact angle without the influence of the pores cannot be measured but is likely to be higher than 10° . Consequently, leakage of the membrane does not occur unless very high pressure is applied.

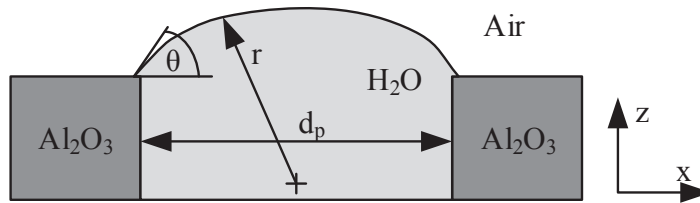


Figure 3.6: Interface between air and water that is pressed out of a pore.

3.3.3 Silica-aerogels as porous membranes

The above presented porous materials, such as agarose hydrogels or AAO, fulfil the requirements of the horizontal and vertical concepts. However, agarose hydrogels

have also a few drawbacks especially regarding the sample preparation, for which the concept of the surficial phaseguides requires many cleaning steps, and regarding the low mechanical stability of the hydrogels. In particular, low pressure differences between both sides of the hydrogel might result in detaching or breakage of the membrane. [87]

An alternative is the application of silica aerogels as porous membranes. This aerogel consists only of silicon oxide nanoparticles that form a porous network. The porosity is typically very high (80-99.8%) with pores in the range of 10 to 70 nm. The arrangement of the pores is random because of the sponge-like system of the nanoparticles. Silica aerogels exist as thin films but also as bulk material.

Due to the small pore sizes, the capillary pressure during the filling or emptying of a liquid might reach very high values. In combination with the low strength, this results in a high risk that the gel collapses. A suitable scenario to avoid this failure is, that the gel between the cultivation chamber and the nutrient channel remains wet all the time (i.e. no storage at dry conditions) and gel towards the gas channel remains dry. In this case, the emptying and filling of the aerogel with liquids is avoided. To avoid any penetration with watery solution, the gel must have a hydrophobic coating [28].

The fabrication consists of several steps. At first, precursors like tetraethyl orthosilicate (TEOS) or tetramethyl orthosilicate undergo a hydrolysis reaction that forms a sol (solution with silica nanoparticles). During the following condensation reaction, these nanoparticles form a network. The speed of the hydrolysis is increased significantly in acid regimes while the condensation reaction is accelerated in alkaline regimes. Therefore, a two step reaction is preferred for a better control of the gel, in which the pH-value is below 7 during the hydrolysis and above 7 in a second step to provide a better condensation reaction. Subsequently, the aqua- or alcogel² is aged in order to strengthen the gel before the surface is modified, e.g. with hexamethyldisilazane (HMDS), to form hydrophobic gels. Finally, the gel is dried. During this step, there is a high risk of breakage of the gel due to the capillary pressure. This risk can be avoided by using supercritical drying or by evaporating a liquid with low surface tension e.g. hexane instead of water. Furthermore, the gel shrinks up to 30% during the drying process.[28]

If such an aerogel is integrated and used as interface, e.g. between the cell culture and the gas supply, cracks or breakage due to shrinkage must be avoided. The shrinkage can be reduced by an extended aging process, the addition of polyethylene glycol (PEG) and surface modifications with HMDS. A feasible integration method is to fill powder blasted holes of a borosilicate wafer with a bottom layer of the Etertec XP-800-15 dry film resist with the sol (see fig. 3.7). By doing so, the sol

²Alcogel is a gel, in which the pores are filled with alcohol and aquagel accordingly a gel with water.

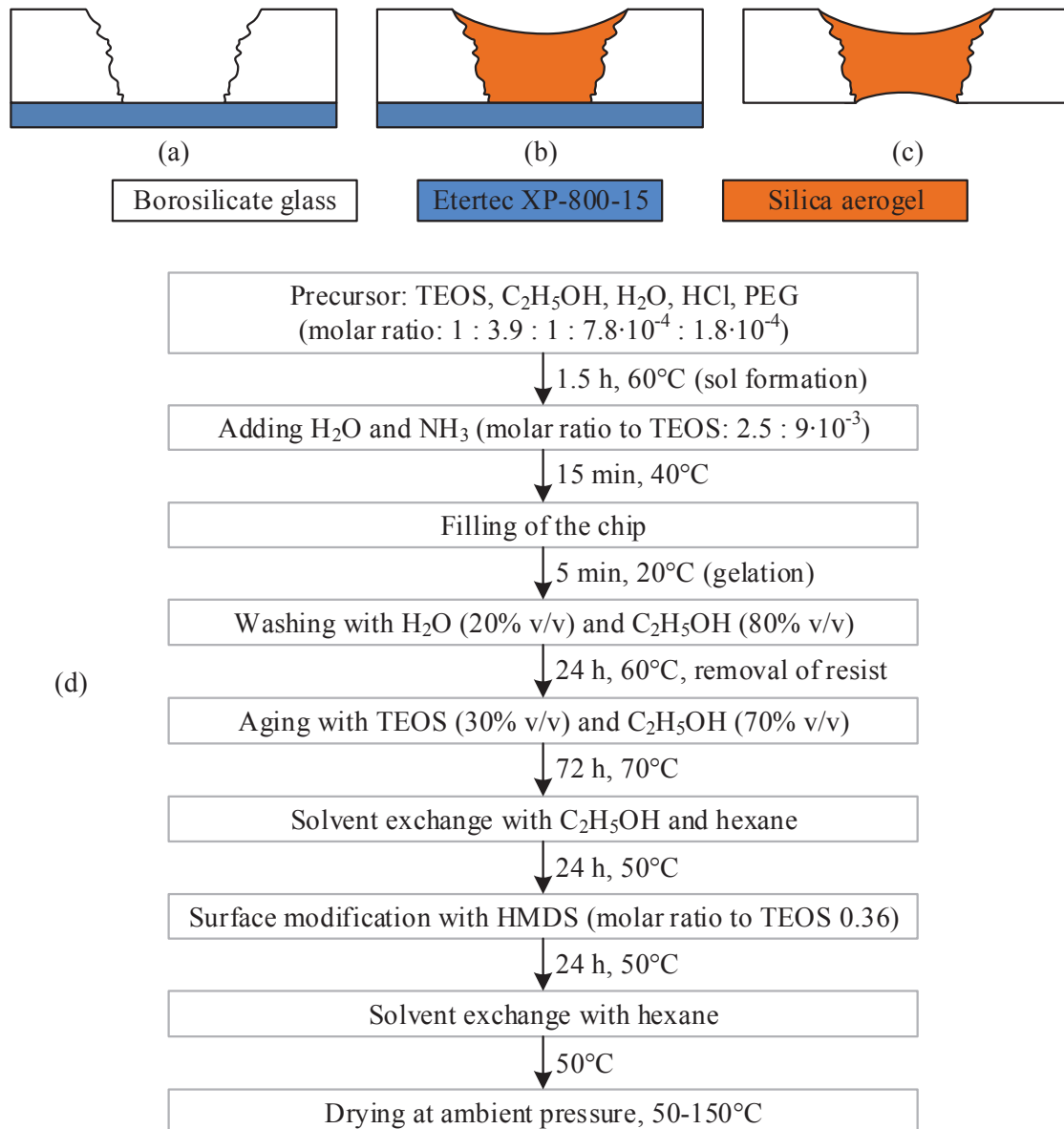


Figure 3.7: Fabrication of the silica aerogels as bulk material in holes of borosilicate glass: (a) borosilicate glass wafer with powder blasted holes and dry film resist Etertec XP-800-15 as bottom layer (b) formation of the aerogel inside the hole (c) removal of the resist (d) detailed process of the aerogel formation.

forms an alcogel before the bottom layer is detached because of the ethanol. In order to achieve a fast but controllable gelation, the gel formation is based on a two-step-process: first with HCl and later with NH_4OH . Finally, the alcogel is aged for 72 h, modified and dried to form the aerogel on-chip. The detailed process is presented in fig. 3.7(d).

Out of several experiments with different concentrations of the compounds and different process times, only the recipe of fig. 3.7 with and without PEG was



Figure 3.8: Powder blasted holes with a diameter of 1.2 mm, that are filled with silica aerogel with PEG with 80 % success rate. [87]

successful. Fig. 3.8 shows a piece of borosilicate glass with powder blasted holes with a diameter of 1.2 mm. Here, 4 of 5 holes are filled successfully with the silica aerogel with PEG.

The structure of the gel is shown in fig. 3.9(a). The network is porous with pores between 20 and 80 nm. The pores are arranged in a random network similar to a sponge. In comparison, fig. 3.9(b) shows aerogel without PEG but with higher ethanol concentrations (molar ratio to TEOS 7:1 instead of 3.9:1). This aerogel has a smooth surface without pores or with thin pores. Underneath the surface is a highly porous structure with nanopores between 30 and 90 nm and a few mesopores with diameters between 300 and 400 nm.

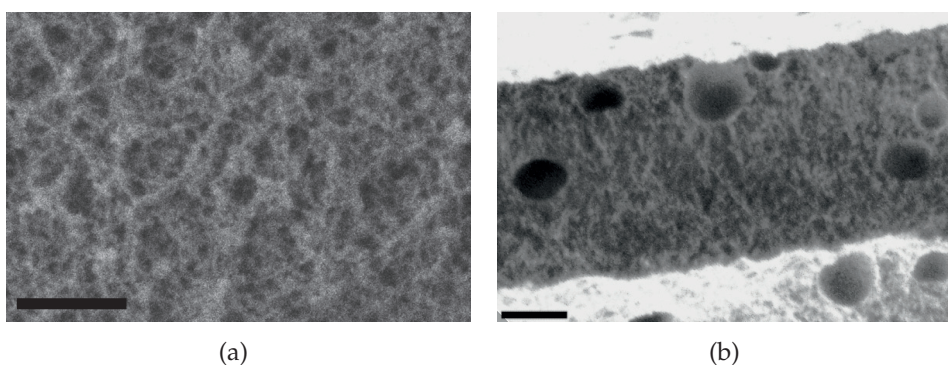


Figure 3.9: SEM-image of different silica aerogels (scale bar is 500 nm): (a) silica gel with addition of PEG (b) aerogel without PEG but with a higher ethanol concentration.

The density of a block of aerogel was determined as $0.44 \frac{\text{g}}{\text{cm}^3}$ which equals a porosity of about 78 %. This value is lower than the reported values between 80 and 99.8 % in the literature [86]. However, the presented aerogels are optimised regarding the low shrinkage and high stability. The contact angle of the aerogel is 136° as shown in fig. 3.10(a). The contact angle remains stable for at least 5 months which proves the successful coating with HMDS to form a hydrophobic surface.

A glass chip with different hole geometries is shown in fig. 3.10(b). 12 out of 15 circular holes with a diameter between 0.5 and 1.5 mm are filled successfully with the silica aerogel without PEG. Furthermore, oblong holes with the dimension 0.5

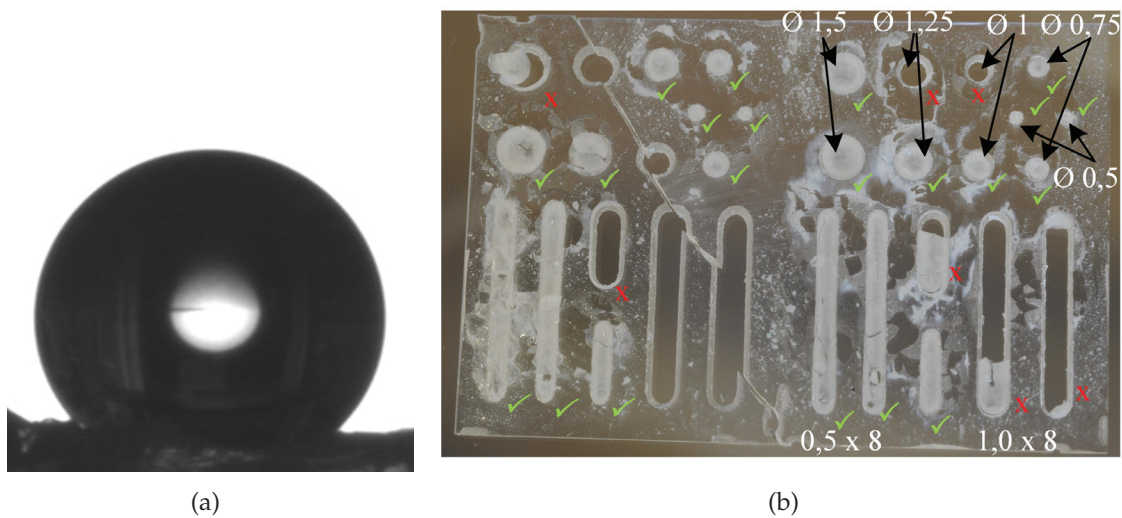


Figure 3.10: Successful aerogel: (a) water droplet is repelled by the hydrophobic surface of the silica gel with PEG (b) image of a chip with different hole diameter that are filled with aerogel without PEG (all dimensions are given in mm).

by 8 mm^2 work also fine while the aerogel did not adhere on oblong holes with the dimensions $1 \text{ by } 3.3 \text{ mm}^2$ or $1 \text{ by } 8 \text{ mm}^2$.

A exemplary hole with a diameter of 1.8 mm is shown in fig. 3.11. The gel is a bit inhomogeneous but clearly fills the hole. The surface profile indicates that the top and the bottom surfaces are concave. The top surface is up to $180 \mu\text{m}$ lower than the glass surface while the height difference at the bottom is up to $260 \mu\text{m}$ with a mean value of $160 \mu\text{m}$. Consequently, the thickness of the aerogel varies between $60 \mu\text{m}$ at its thinnest part and $500 \mu\text{m}$ on the outer sides.

The above presented aerogels are all horizontal and thus allow the diffusion in vertical direction. However, the vertical integration similar to the agarose hydrogels is also attractive as the amount of required layers could be reduced. In this case, the silica gel could benefit of geometrical phaseguides if the gel is filled into a channel prior to the gelation.

3.3.4 Comparison of the porous materials

The three different porous membranes - agarose hydrogels, anodised aluminium oxide and silica aerogels - fulfil the requirements of the horizontal and the vertical concept. The materials are compared in tab. 3.1 regarding the most important properties for the cell cultivation. In comparison, the integration of silica aerogels is more complex compared to the other materials. Therefore, the horizontal concept is realised with agarose hydrogels and the vertical concept with AAO for this work.

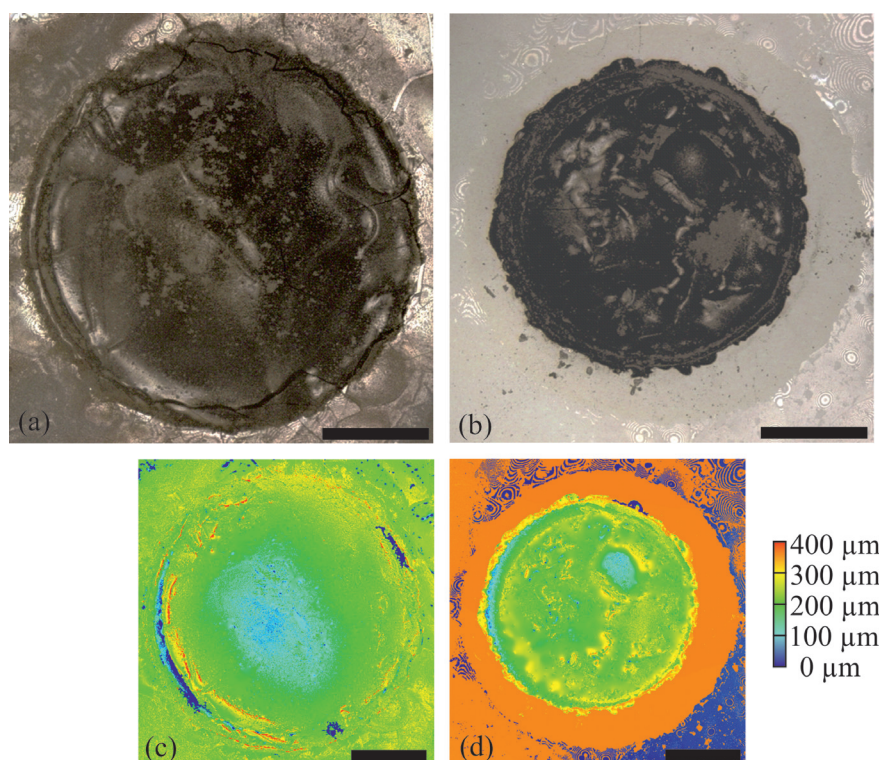


Figure 3.11: Circular holes with a outer diameter of 1.8 mm that are filled with aerogel without PEG (scale bar is 500 μm : (a) top view with microscope (b) bottom view (c) surface profile of the hole from top (d) surface profile from bottom.

Table 3.1: Comparison of presented porous materials - agarose hydrogel, anodised aluminium oxide (AAO) and silica aerogels.

	Agarose hydrogel	AAO	Silica aerogel
Material	Polymer chains	Aluminium oxide	Silicon oxide
Porosity	> 98 %	22 %	85 %
Mean pore diameter	≈ 100 nm	38 nm	50 nm
Pore arrangement	Random, sponge-like	Unidirectional, perpendicular to surface	Random, sponge-like
Membrane thickness	0.8 ... 1.1 mm	3 μm	0.05 ... 0.4 mm
Pore formation	Gelation by cooling	Anodisation	Sol-gel process
Membrane orientation	Vertical	Horizontal	Horizontal (vertical possible)
Mechanical stability	Low	High	Medium
Chemical stability	Low	Medium	High
Ease of fabrication	Simply	Medium	Complex
Special features	Easy to replace	Easy to tune	Hydrophobic surface

3.4 Implementation

This section describes how the concepts of sec. 3.2 are realised by using the porous materials of sec. 3.3. At first, the design aspects of the horizontal chip are discussed in sec. 3.4.1 and of the vertical concept in sec. 3.4.2. Subsequently, the fabrication processes of both concepts are presented in sec. 3.4.3. The final devices are mounted in holders to facilitate the handling. Therefore, the assemblies are described in sec. 3.4.4.

3.4.1 Design of the horizontal concept

The aim of this section is to find the optimal design for the concept with the horizontal supply as described in 3.2.1. The technology of surficial phaseguides is applied to create hydrogel membranes in the microfluidic chip. Sec. 3.4.1.1 analyses the influence of the design parameters (e.g. channel width, misalignment of the phaseguides, etc.) and determines the best values. Afterwards, the dimensions of the culture chamber are investigated in sec. 3.4.1.2 based on an analytical model. A reasonable design is very important to guarantee sufficient supply (especially of oxygen). The width of the chamber and of the hydrogel membrane as well as the chamber height are discussed regarding optimal growth conditions. Finally, the design of the chip is summarised in sec. 3.4.1.3.

3.4.1.1 Application of surficial phaseguides

Surficial phaseguides enable to create hydrogel membranes within a microfluidic chip as described in sec. 3.3.1.2. For a robust functioning, an optimal design regarding the width of the wall-less channel, alignment tolerances and width of the phaseguides, as well as a reasonable design of the intersections with solid walls is discussed in this section. In this section, all parameters are analysed for a channel height of 380 μm , which is the height of a standard silicon wafer. Later on, sec. 3.4.1.2 verifies the choice of this height. [12]

Width of the wall-less channel

The wall-less channel (see fig. 3.12) shall be filled by capillary pressure (i.e. $p < 0 \text{ Pa}$) which depends on the shape of the meniscus and hence also on its geometry. In the midsection of the liquid (i.e. $z = \frac{h}{2}$), the radii are calculated as $r_{xz} = -\frac{h}{2 \cos \theta_{gl}}$ and $r_{xy} = \frac{w_c}{2}$ with the channel width w_c . By using eq. 3.2, the minimal width for a

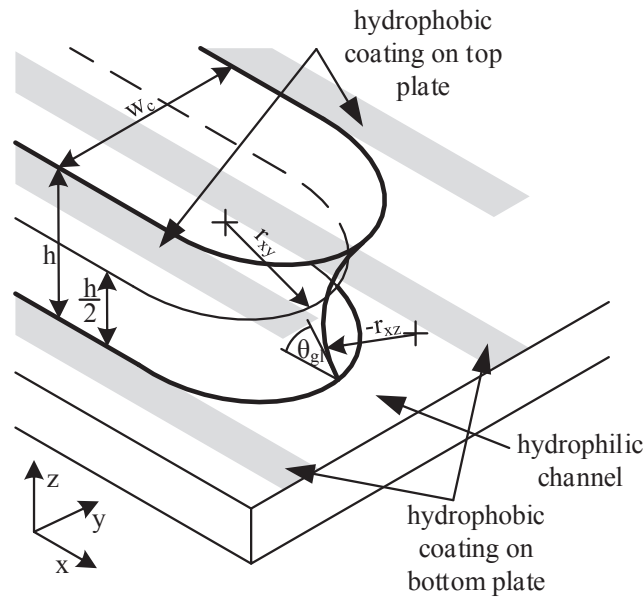


Figure 3.12: Sketch of the wall-less channel in which the hydrophobic coatings (in grey) surround the propagating liquid. The top plate is not depicted. [12]

given pressure p is found as

$$w_{c,min} = \left(\frac{p}{2\sigma} + \frac{\cos \theta_{gl}}{h} \right)^{-1}. \quad (3.7)$$

The channel of the microfluidic chip is $380 \pm 5 \mu\text{m}$ high (see also sec. 3.4.1.2) and the contact angle of the borosilicate glass is measured as $16 \pm 2^\circ$. Therefore, the minimal width is $395 \pm 9 \mu\text{m}$ if no external pressure is applied. However, wider channels result in lower capillary pressures during filling and thus a more robust channel. This robustness is required as dirt might influence the contact angle negatively and the inlets and outlets are weak points. In case of $w_c = 2h = 760 \mu\text{m}$ and $w_c = 3h = 1140 \mu\text{m}$, the capillary pressure during the filling is lowered to $p = -177 \text{ Pa}$ and -234 Pa , which gives a higher theoretical safety margin before the phaseguides fail³.

Alignment tolerance of the phaseguides

Ideally, the phaseguides at the bottom and the ceiling are perfectly aligned. In reality, misalignment occurs due to fabrication tolerances. Small misalignments $y_{mis,a}$ result in slightly inclined surfaces with the contact angles θ_{b1} and θ_{b2} with $\theta_{gl} < \theta_{b1} < \theta_{b2} < \theta_{odt}$ (see fig. 3.13(a)) if no external pressure is applied. In this case,

³In ideal conditions, the phaseguides fail for $p > 86 \text{ Pa}$, see also sec. 3.3.1.2.

$y_{mis,a}$ is limited to

$$y_{mis,a} \leq \frac{-h}{\tan \theta_{odt}}. \quad (3.8)$$

With a channel height of $380 \pm 5 \mu\text{m}$ and $\theta_{odt} = 103 \pm 1^\circ$, this limit is $84 \pm 4 \mu\text{m}$.

If the misalignment is larger, the liquid flows on the phaseguides with the width t_{ph} and stops when the meniscus is straight again (see fig. 3.13(b)). Yet, the concept of phaseguides still works if the liquid stops on the phaseguide and does not flow completely above the hydrophobic surface and thus if the misalignment $y_{mis,b}$ is

$$y_{mis,b} < t_{ph} - \frac{h}{\tan \theta_{odt}}. \quad (3.9)$$

Therefore, even large misalignments ($184 \mu\text{m}$) are acceptable for $t_{ph} = 100 \mu\text{m}$, although there is a high risk of overflow once additional pressure is applied.

To sum it up, the maximal misalignment of the phaseguides for the presented design with $h = 380 \mu\text{m}$ high channels and $100 \mu\text{m}$ wide phaseguides is $184 \mu\text{m}$. This misalignment tolerance is very high compared to the channel height of $380 \mu\text{m}$ and to common alignment tolerances during the fabrication process of microsystems.

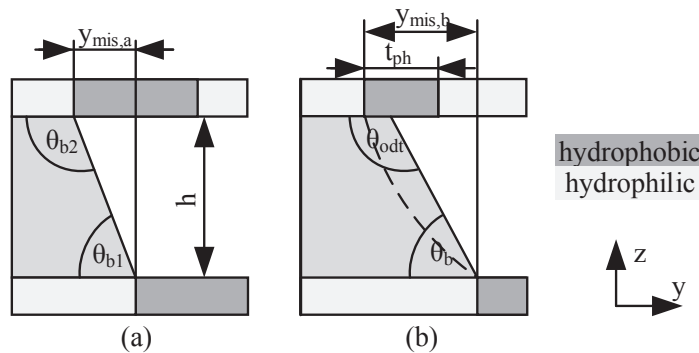


Figure 3.13: Sketch of resulting menisci if the upper and lower phaseguide are misaligned: (a) small misalignment and no pressure is applied (b) large misalignment with negative pressure (dashed) and without pressure (straight line). [12]

Width of the phaseguides

The principle of surficial phaseguides is based on different surfaces with different wetting properties. Unless high misalignment occurs, the liquid stops at the boundary between both surfaces, meaning that a one-dimensional phaseguide would be theoretically sufficient. Obviously, only two-dimensional structures can be fabricated and wider elements are more robust against fabrication errors.

When the liquid is inserted into the chip, the pressure might fluctuate due to a non-uniform filling speed or other effects. A temporarily high pressure results in an overflow of the phaseguides. If the phaseguides are wider than this overflow, the liquid is retracted once the pressure is lowered again. Consequently, wide phaseguides can compensate pressure fluctuations and thus result in a more robust design.

In our experiments, we managed to fill various chips with a phaseguide width of $100\ \mu\text{m}$ with a very high success rate. In contrast, $30\ \mu\text{m}$ wide phaseguides also work but require more care to fill.

Intersection with walls

The horizontal concept as described in sec. 3.2.1 contains porous walls out of hydrogel and also solid walls made out of silicon. Consequently, the wall-less hydrogel channel contains intersections with the silicon walls. The capillary effect occurs with every surface: the bottom and the top plate and also the solid walls that surround the microfluidic chip. The contact angle of the walls θ_w depends not only on the material but also on the surface texture. This angle cannot be measured within the chip because the meniscus is influenced by the top and bottom plate as well. Nevertheless, the walls that are made out of silicon can be assumed as hydrophilic, so that liquid is pulled along the wall forming a meniscus with the radius r_{xy} in the x-y-plane despite the hydrophobic phaseguides (see fig. 3.14).

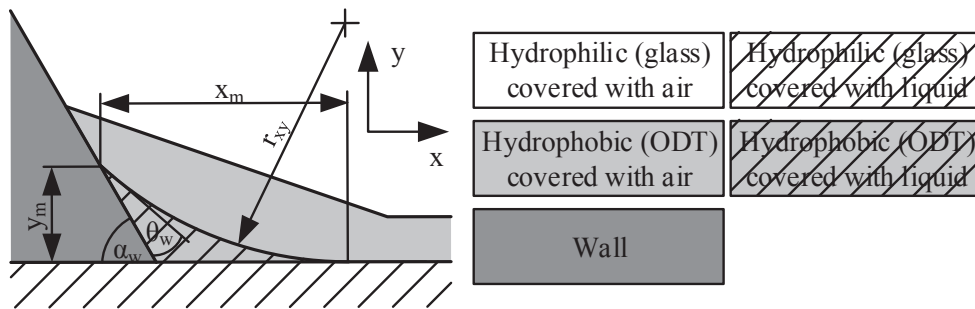


Figure 3.14: Sketch of the meniscus (top view) which is formed on a hydrophilic wall next to the phaseguide in the x-y-plane. [12]

The resulting radius r_{xy} with the wall is determined with eq. (3.2) and (3.3) as:

$$r_{xy} = - \left(\frac{p}{\sigma} - \frac{2 \cos \theta_{odt}}{h} \right)^{-1}. \quad (3.10)$$

The wall is inclined with the angle α_w in the x-y-plane regarding the direction of the phaseguides. Consequently, the dimensions of the meniscus in x- (i.e. along the

phaseguide) and y-direction (perpendicular to the phaseguide) are:

$$x_m = r_{xy} \sin(\alpha_w - \theta_w) \quad (3.11)$$

$$y_m = r_{xy}(1 - \cos(\alpha_w - \theta_w)). \quad (3.12)$$

As a consequence, the liquid forms no meniscus without additional pressure if $\alpha_w \leq \theta_w$. However, very sharp elements (i.e. very small α_w) are difficult to fabricate. As a trade-off, α_w is chosen as 30° which results in $x_m = 218 \mu\text{m}$ and $y_m = 29 \mu\text{m}$ for $\theta_w = 15^\circ$. As already described, the width of the phaseguides is chosen as $100 \mu\text{m} \geq y_m$, so that the intersections are sufficiently robust.

3.4.1.2 Diffusion of oxygen

The presented concept is based on the supply of gases and nutrients by diffusion. Consequently, the dimensions (especially the height and width) of the chamber have to be chosen in a way that allows sufficient diffusion. The key parameters, which are the diffusion coefficient and the exchange time (i.e. the time until they are completely consumed), are listed in tab. 3.2. Although oxygen has the highest diffusion coefficient, it is the most critical parameter due to the short time until the oxygen has to be refreshed (referred to as exchange time). Hence, the design is optimised for sufficient oxygen supply which results also in good supply with fresh medium because of the symmetric concept. [14]

Table 3.2: Overview of key reactants and products of the cell metabolism, the required exchange time (see sec. 3.1) and the diffusion coefficients in water.

Consumatives / waste	Exchange time	Diffusion coefficient
Oxygen	1 h	$2.4 \times 10^{-9} \frac{\text{m}^2}{\text{s}}$ [83]
Glucose	28 h	$0.6 \times 10^{-9} \frac{\text{m}^2}{\text{s}}$
Lactate	11 h	$1 \times 10^{-9} \frac{\text{m}^2}{\text{s}}$ [89]
Ammonium	50 h	$1.9 \times 10^{-9} \frac{\text{m}^2}{\text{s}}$

The following model (see also fig. 3.15), that is used later on to optimise the design, is based on the assumption, that

- The channel height is much smaller than the width. Therefore, the diffusion can be modelled 1-dimensional.
- All cells are equally distributed within the chamber and the OCR is independent of time, location and oxygen concentration. As explained in sec. 3.1.3, the OCR decreases only in case of very low concentrations of oxygen which shall be avoided with a good design of the chamber.

- The diffusion coefficient of oxygen in agarose hydrogel is assumed to be equal to the coefficient in water [83].
- Boundary condition 1: The oxygen concentration in the gas supply channel is constant ($c(x = -w_{HG}) = c_0$), where w_{HG} is the width of the hydrogel.
- Boundary condition 2: No oxygen diffuses from the nutrient channel towards the cells. So, $\frac{dc(x=w_{Gr})}{dx} = 0$, where w_{Gr} is either the width of the culture chamber or the point, where $c(x = w_{Gr}) = 0$, because all cells would be dead for $c = 0$. This condition is a worst-case scenario and might not be true if oxygen is dissolved in the media and fresh media is supplied continuously.

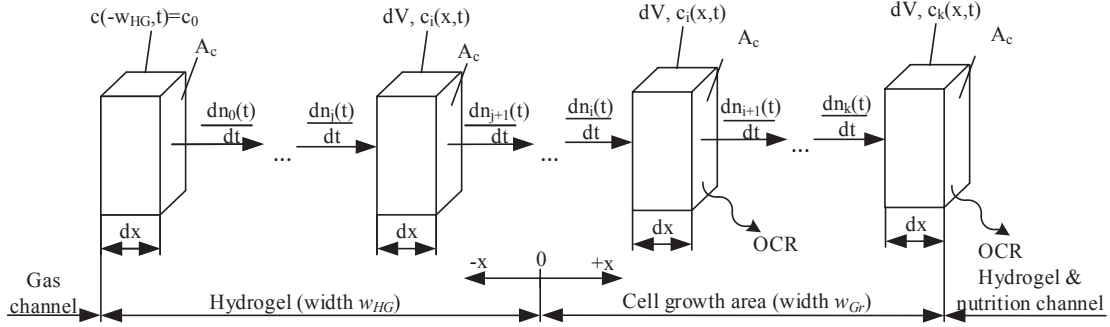


Figure 3.15: Model of oxygen supply by diffusion through the hydrogel and the growth area and the consumption by the cells.

The diffusion of a substance in liquids is based on a concentration gradient that results in a flux density:

$$-D \frac{dc}{dx} = \frac{1}{A_c} \frac{dn}{dt} \quad (3.13)$$

where D is the diffusion coefficient, c the concentration, A_c the cross-section that is perpendicular to the direction of diffusion and n the amount of substance. The flux density enables a change of concentration in a small volume $dV = A_c dx$ unless the substances is consumed as

$$\frac{dn}{dt} = \left(\frac{dc}{dt} - \frac{\gamma_f OCR}{A_z h} \right) A_c dx, \quad (3.14)$$

where OCR is the oxygen consumption rate of a single cell, A_z the area of a cell, h the chamber height and γ_f the filling factor that describes the area occupied by cells relative to the total culture area. Inserting eq. 3.14 in eq. 3.13 results in the

differential equation of the system as

$$-D \frac{d^2c}{dx^2} = \frac{dc}{dt} - \frac{\gamma_f OCR}{A_z h}. \quad (3.15)$$

The survival of the cells is mainly limited in the stationary state because the media is enriched with dissolved oxygen during the first filling process. In the stationary state, $\frac{dc}{dt} = 0$ and thus simplifies eq. 3.15 to

$$-D \frac{d^2c}{dx^2} = -\frac{\gamma_f OCR}{A_z h}, \quad (3.16)$$

with the solution for c as

$$c(x) = \frac{\gamma_f OCR}{2A_z h D} x^2 + k_1 x + k_2. \quad (3.17)$$

The real system consists of two parts: the hydrogel with $OCR = 0$ for $-w_{Hg} \leq x < 0$ and the culture chamber with $OCR > 0$ for $0 \leq x < w_{Gr}$. At the boundary of both parts, the concentration is continuous and continuously differentiable. Considering this together with the general boundary conditions, the concentration in the system is found as

$$c(x) = \left\{ \begin{array}{ll} k_1 x + k_2 & -w_{Hg} \leq x < 0 \\ \frac{\gamma_f OCR}{2A_z h D} x^2 + k_1 x + k_2 & 0 \leq x < w_{Gr} \end{array} \right\}, \quad (3.18)$$

with

$$k_1 = \frac{-\gamma_f OCR w_{Gr}}{A_z h D} \quad (3.19)$$

$$k_2 = c_0 - \frac{\gamma_f OCR w_{Gr} w_{Hg}}{A_z h D}. \quad (3.20)$$

The oxygen concentration decreases linearly within the hydrogel and parabolically within the culture chamber. Fig. 3.16 shows exemplary the spatial course of the oxygen concentration in case of $h = 380 \mu\text{m}$, $w_{Hg} = 1140 \mu\text{m}$ and a culture chamber width of 5 mm for different filling factors. If the filling factor is above 0.21 (i.e. 21 % of the chamber area are covered with cells), the width of the growth area is lower than the chamber width. In case of $\gamma_f = 0.5$, the oxygen concentration decreases to 0 within 2.9 mm which means that 42 % of the culture area is not supplied with oxygen.

The ideal design is obviously as wide as possible to provide space for a high number of cells but narrow enough to supply all cells equally with oxygen. So, the

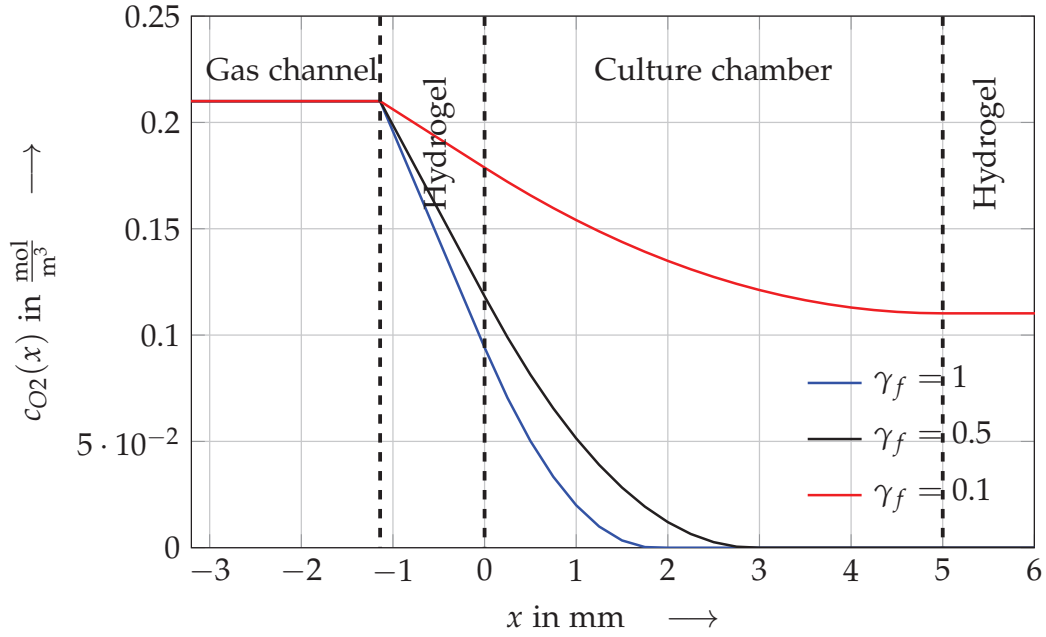


Figure 3.16: Course of the oxygen concentration for different filling factors γ_f which describe how much area is covered with cells for $h = 380 \mu\text{m}$, $w_{Hg} = 1140 \mu\text{m}$ and the width of the culture chamber of 5 mm.

ideal width of the culture chamber equals w_{Gr} . As a consequence, the maximal width of the growth area w_{Gr} is found as

$$w_{Gr} = -w_{Hg} + \sqrt{w_{Hg}^2 + \frac{2c_0A_zhD}{\gamma_fOCR}}. \quad (3.21)$$

This equation shows the main relationship between the design parameters. In general, the width of the growth area increases with...

- ...thinner hydrogels ($w_{Hg} \rightarrow 0$) towards the upper limit $\sqrt{\frac{2c_0A_zhD}{\gamma_fOCR}} = 2.8 \text{ mm}$ (for $h = 380 \mu\text{m}$) as shown in fig. 3.17(a).
- ...higher culture chambers ($h \rightarrow \infty$). As explained in sec. 3.4.1.1, the width of the hydrogel has to increase linearly with the height ($w_{Hg} = \alpha_{PG}h$). So, the width of the growth area converges to the upper limit $\frac{c_0A_zD}{\alpha_{PG}\gamma_fOCR} = 3.4 \text{ mm}$ (for $\alpha_{PG} = 3$) as shown in fig. 3.17(b).
- ...lower filling factor γ_f (i.e. less area is covered with cells) as shown in fig. 3.17(c). The maximal width of the growth area converges to infinity for $\gamma_f \rightarrow 0$.
- ...smaller cells because OCR is proportional to the volume V_z of the cell so that $OCR \sim V_z \sim r_z^3$ (r_z is the dimension of the cell) while $A_z \sim r_z^2$ [112].

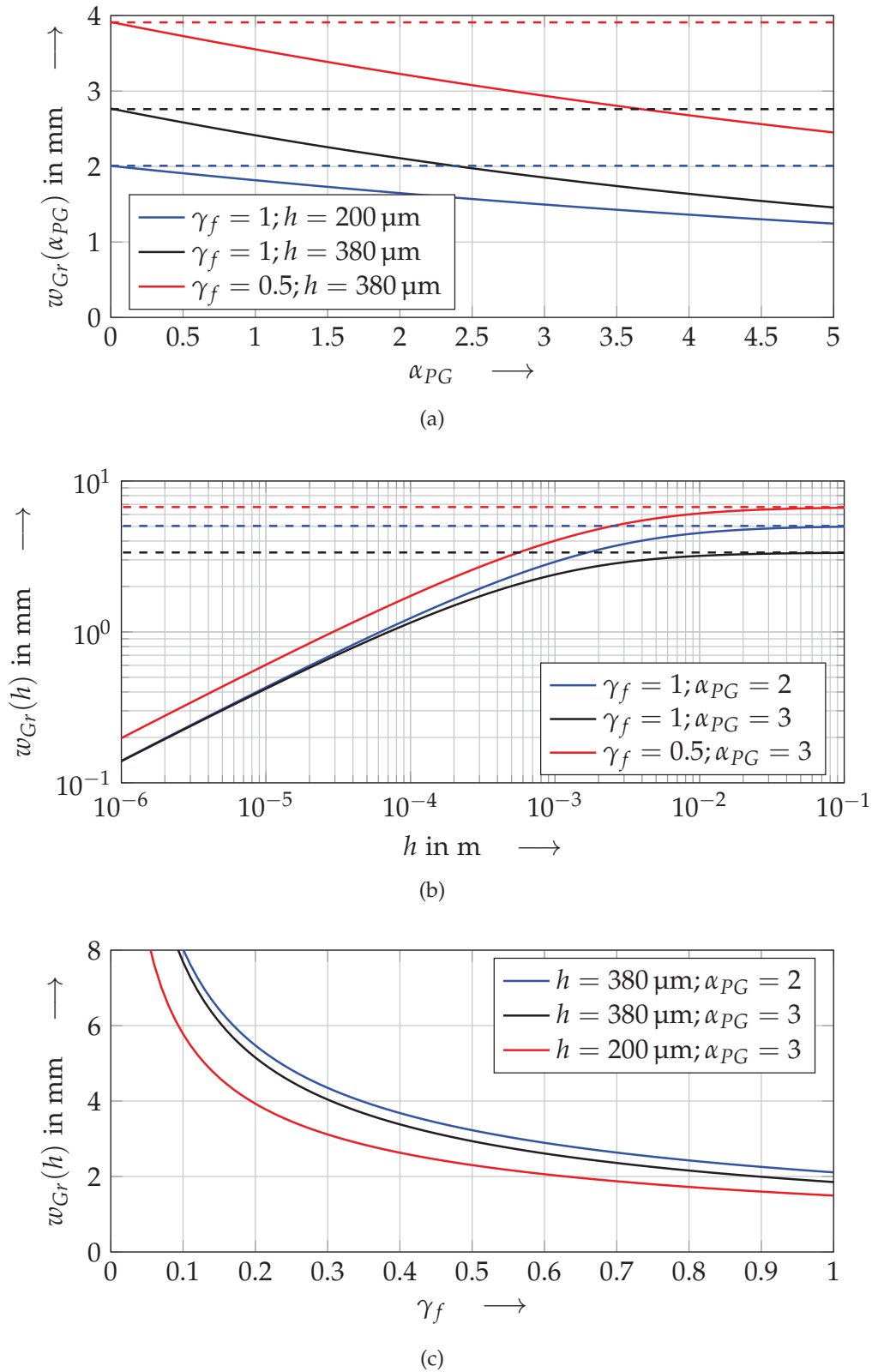


Figure 3.17: Dependency of the width of the growth area w_{Gr} on: (a) the width of the hydrogel membrane relative to the chamber height ($\alpha_{PG} = \frac{w_{HG}}{h}$), where the theoretical upper limits are dashed (b) the chamber height h (the theoretical upper limits are dashed) (c) different filling factors γ_f , which describe the relative amount of the surface covered with cells.

The limits above are calculated with $c_0 = 0.21 \frac{\text{mol}}{\text{m}^3}$, $D = 2.4 \times 10^{-9} \frac{\text{m}^2}{\text{s}}$, $OCR = 20 \times 10^{-18} \frac{\text{mol}}{\text{cell s}}$, $A_z = 4 \times 10^{-10} \text{ m}^2$ and $\gamma_f = 1$.

As a conclusion, the height of chamber shall be chosen as high as possible. Silicon wafers, which define the chamber height, are commercially available with different thickness between 200 μm and 1000 μm . As described in sec. 3.4.1.1, lower channel heights result in more robust wall-less channels. The usage of standard silicon wafer with a height of 380 μm , which are also cost-effective, is considered as good trade-off between robust phaseguides and large growth areas. The width of the hydrogel membrane has only a minor influence on the growth area. As wider hydrogels are more robust, a reasonable compromise between robustness and a sufficiently large growth area is $\alpha_{PG} = 2 \dots 3$ and so $w_{Hg} = 760 \dots 1140 \mu\text{m}$.

The filling factor is obviously no design parameter but an operational parameter. Limiting e.g. $\gamma_f < 0.5$ means that a part of the cells have to be removed from the chamber once 50% of the area is covered with cells. Mammalian cells require uncovered areas to grow and divide. If the entire area is already covered with cells, further cell division might result in stress on the cells or even changes of the cells. Consequently, the filling factor should be limited to 0.5.

Considering the mentioned parameters, the maximal width of the growth area is found as 3 mm and so that the culture chamber should be 3 mm wide.

3.4.1.3 Detailed design of the chip

The design of the chip of the horizontal concept is developed as shown in fig. 3.18 with respect to the design considerations of sec. 3.4.1.1 and 3.4.1.2. The chip is 13 mm by 17.5 mm large and contains 10 circular inlets with a diameter of 1.2 mm and one additional inlet for air of 7.8 mm by 1.2 mm. The culture chamber has a width of 3 mm including two 100 μm wide phaseguides and an entire culture area of 24 mm^2 . Assuming a cell size of 20 μm by 20 μm , up to 30,000 cells can be cultured inside the chip considering the maximal filling factor of 0.5. The channels of the hydrogel are 0.8 mm wide, which is a good compromise between stability and fast diffusion.

3.4.2 Design of the vertical concept

As explained in sec. 3.2.2, the chip of the vertical supply concept consists of two silicon layers with chambers and channels and the unmachined glass layer as shown in fig. 3.19. The bottom layer contains four inlets with a diameter of 0.5 mm and the bottom chamber with channels to the inlets with a height of 200 μm . The membrane is attached on the middle layer and is wider than the top chamber (height 380 μm). This chamber is connected to the inlets via 200 μm deep channels that are on the

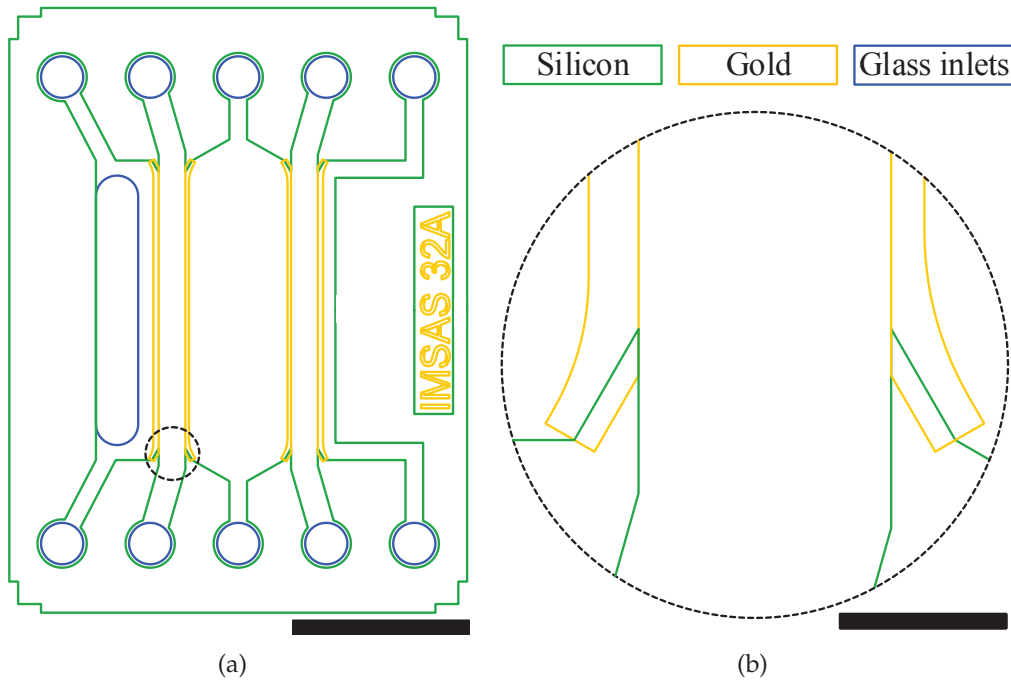


Figure 3.18: Top view of the final design of the horizontal concept showing the silicon structures (green), the phaseguides out of gold (yellow) and the powder blasted glass inlets (blue): (a) entire chip (scale bar: 5 mm) (b) detail view of the intersection of the hydrogel channel and the silicon wall (scale bar 500 μm).

opposite side of the layer. The chip has the outer dimensions of 9 mm by 6.5 mm by 1.3 mm. Four different designs are realised with different dimensions of the membrane which are compared in tab. 3.3. [9]

Table 3.3: Overview about the different designs of the vertical supply concept and their geometrical properties.

	1 mm width	2 mm width	Honeycomb	Serial
Figure	3.19(b)	3.19(a)	3.19(c)	3.19(d)
Width of membrane	1 mm	2 mm	0.6 mm	1 mm
Area of membrane	2.6 mm ²	6.4 mm ²	5.7 mm ²	5.2 mm ²
Area of bottom chamber	9.1 mm ²	14.8 mm ²	16.7 mm ²	11.1 mm ²

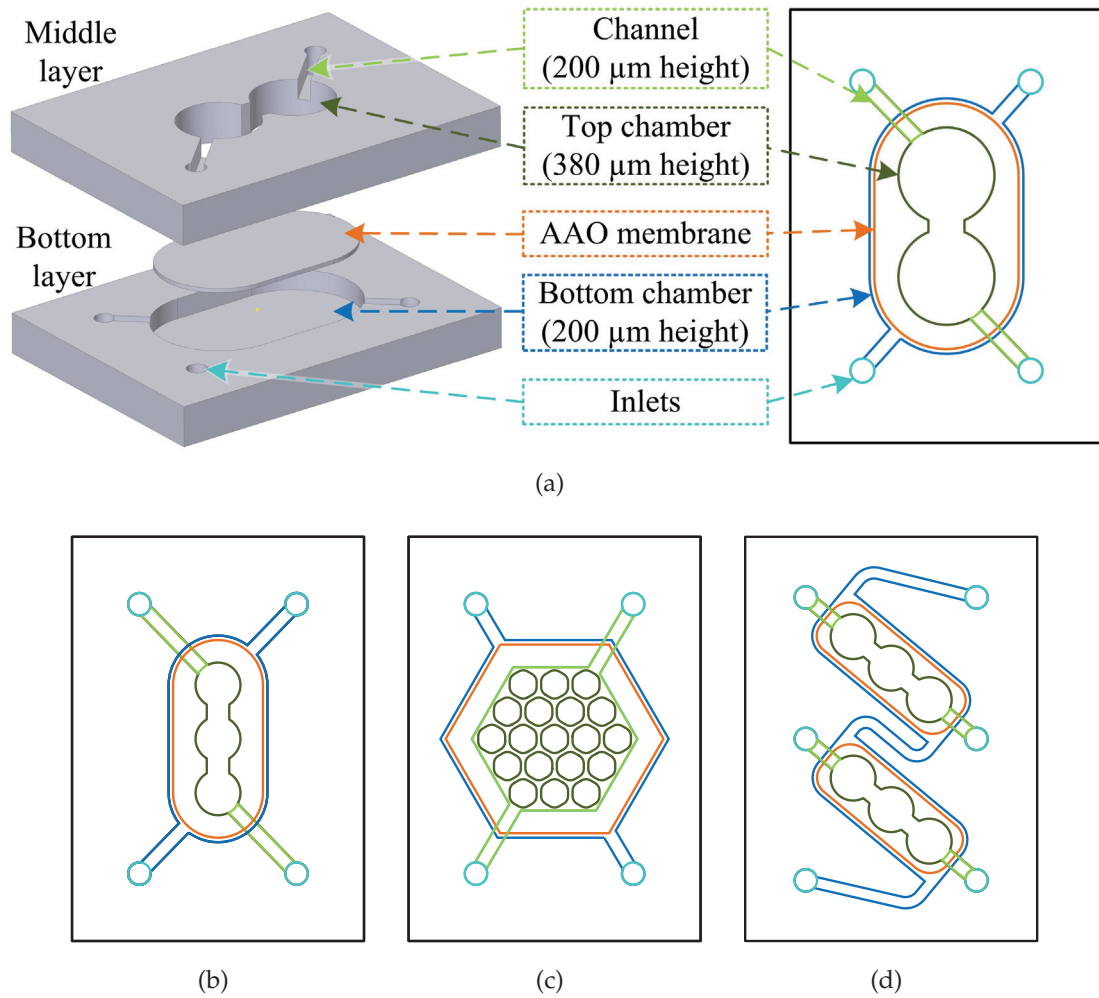


Figure 3.19: Design of the vertical supply concept with the outer chip dimensions of 9 mm by 6.5 mm by 1.3 mm: (a) CAD-rendered image of the silicon layers, in which the top glass layer is not shown (left) and top view of all layers (right) for the 2 mm wide chamber, (b) top view of the 1 mm wide chamber (c) top view of the honey-comb design (d) serial arrangement of two chambers.

3.4.3 Fabrication

The devices are fabricated with common clean room processes. The flowchart and the processes are described at first for the horizontal concept (sec. 3.4.3.1) and subsequently for the vertical concept (sec. 3.4.3.2).

3.4.3.1 Horizontal concept

The chip is designed as a sandwich structure of glass-silicon-glass as summarised in fig. 3.20. At first, two 500 μm thick borosilicate glass wafers are coated with 10 nm titanium nitride and 40 nm gold by sputtering. Titanium nitride is used as adhesion layer. In contrast to more common adhesion layers like chromium or titanium, titanium nitride is also a diffusion barrier [70]. Consequently, the gold layer remains pure and is not contaminated with the adhesion promoter even after being heated to high temperatures during the anodic bonding process. Photoresist AZ1518 from MicroChemicals is spin-coated at 4000 rpm, baked at 100 °C, exposed for 6 s with a foil mask of Zitzmann GmbH at an intensity of 10 $\frac{\text{mW}}{\text{cm}^2}$ and developed with AZ400K. Afterwards, the gold is etched for 3 min in Au Etch 200 purchased from NB Technologies GmbH and the titanium nitride is removed in a mixture of 1 M HCl and 1.8 M H₂O₂. Once the photoresist is removed with AZ100 remover of MicroChemicals, the bottom wafer is finished. The back side of the top wafer is laminated with the dry film resist i-HE of HARKE Germany Services GmbH & Co. KG at 80 °C and exposed for 10 s. After developing with warm water, the front side of the wafer (containing gold elements) is glued on a silicon wafer for protection. Subsequently, the holes are powder blasted with a grain size of 25 μm . The resist is removed in an ultrasonic bath at 70 °C for 2 h. Finally, both glass wafers are cleaned with acetone and isopropanol prior to the anodic bonding. [14]

A standard 380 μm thick silicon wafer is coated with 1 μm aluminium by sputtering that is used later on as an etching stop during the DRIE-process. Photoresist AZ9260 is spin-coated on the other side of the wafer at 2400 rpm, baked for 165 s at 110 °C, exposed for 150 s and developed in AZ726MIF. Afterwards, the silicon is dried-etched using the Bosch-process. Finally, the photoresist is removed with an oxygen plasma and the aluminium is etched in phosphoric acid.

In the last step, the silicon wafer is anodically bonded at first to the bottom glass wafer and finally to the top glass wafer. The phaseguides made out of gold and the silicon are slightly overlapping. Therefore, the temperature during the anodic bonding process has to be set below 360 °C. Otherwise, eutectic bonding of gold and silicon occurs at 369 °C, in which parts of the gold structures flow away (see fig. 3.21). During the first bonding process, it is sufficient to apply a voltage of 600 V. In contrast, the second bonding process is run at higher voltages of 1100 V for

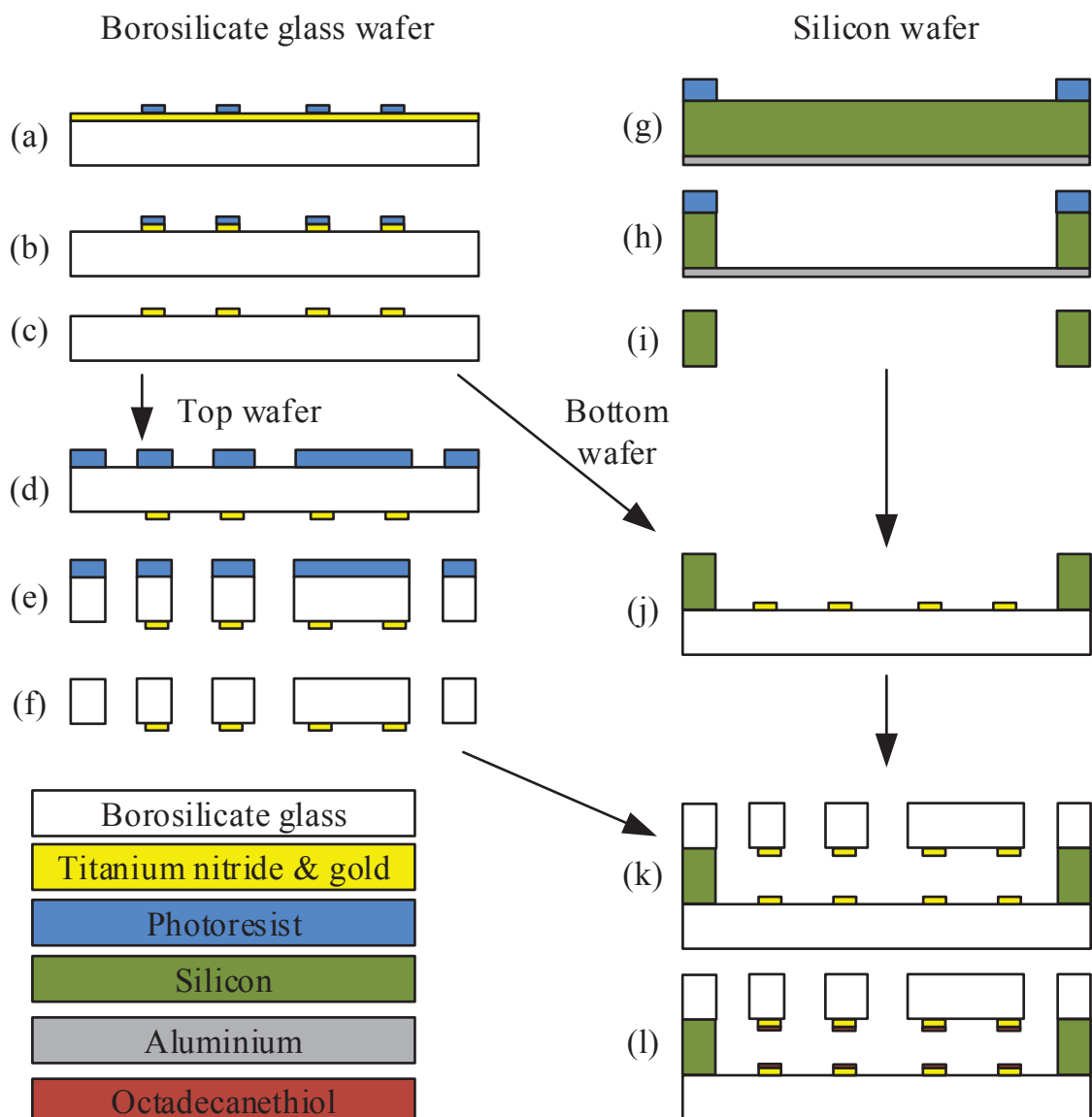


Figure 3.20: Flowchart of the fabrication process where (a) to (c) are carried out for the bottom glass wafer, (a)-(f) for the top glass wafer, (g)-(i) is valid for the silicon wafer and (j)-(l) are the bonding and coating processes: (a) Sputtering of 10 nm titanium nitride, 40 nm gold and patterning with 1.8 μm photoresist on a glass substrate. (b) wet-etching of gold and titanium nitride (c) removal of the resist (d) patterning of dry film resist on the back side (e) powder blasting of glass (f) removal of resist (g) sputtering of aluminium on a silicon wafer and patterning of 10 μm photoresist on the other side (h) DRIE-process (i) removal of aluminium and the photoresist (j) anodic bonding of the bottom wafer and the silicon wafer (k) anodic bonding of the wafer from (j) to the top wafer (l) coating of gold elements with octadecanethiol.

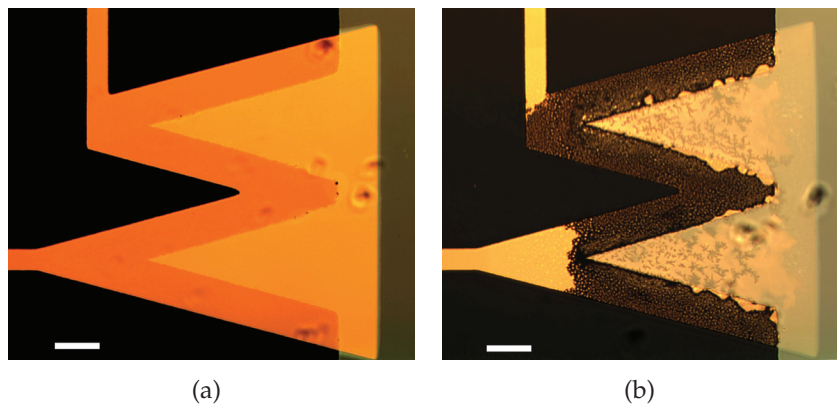


Figure 3.21: Examples of the overlap of gold and silicon after bonding (top view) (scale bar is 100 μm): (a) successful structures without any gold-silicon-eutectic (b) the gold-silicon eutectic is formed during the anodic bonding process which damages the phaseguides.

sufficient bonding strength because the silicon wafer is isolated from the electrode by the first glass wafer. The powder blasting of the top wafer created the holes but also high stress and micro cracks. Due to the high voltage and thus high load during the bonding process, the wafer is likely to break at certain points. However, each wafer contains 21 chips so that only a few systems might be affected by the cracks.

The bonded wafers are diced and each chip is dip-coated for 2 min in ethanol which contains 1 $\frac{\text{g}}{\text{L}}$ of octadecanethiol. Here, only gold surfaces are covered with a self-assembled monolayer of octadecanethiol. As a consequence, the gold becomes hydrophobic with a contact angle of $103 \pm 1^\circ$ (see fig. 3.22(a)). The glass remains hydrophilic with a contact angle of $16 \pm 2^\circ$ (see fig. 3.22(b)) showing that octadecanethiol does not adhere on glass. [12]

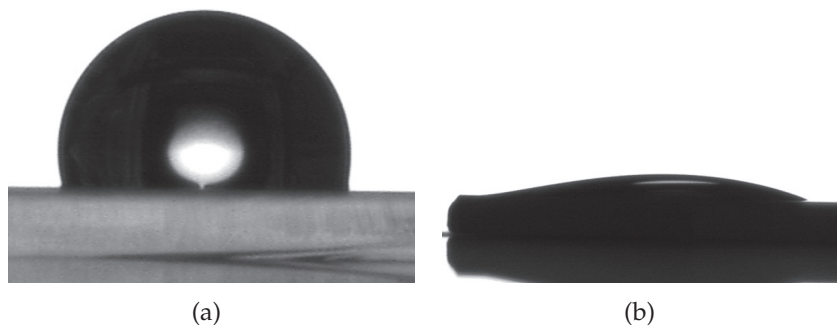


Figure 3.22: Contact angle of DI-water on: (a) gold covered with octadecanethiol: $103 \pm 1^\circ$ (b) glass surface: $16 \pm 2^\circ$. [12]

Fig. 3.23 shows two different chips after the fabrication process. One channel in each chip is filled with water containing a low concentration of indigo carmine for a better visualisation of the hydrogel channels.

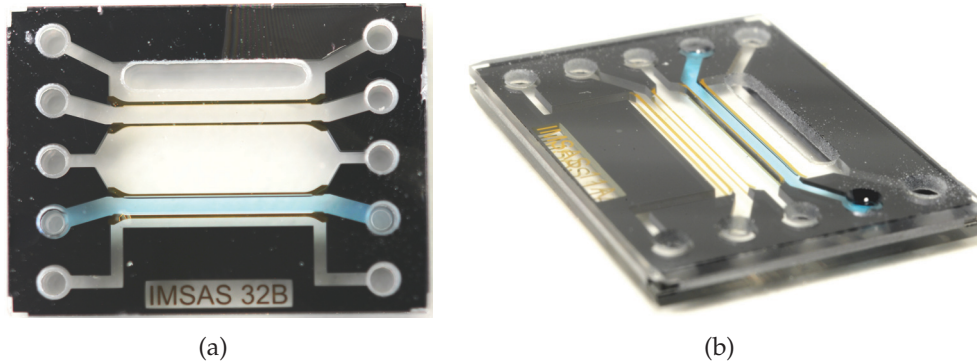


Figure 3.23: Images of two chips of the horizontal supply in which one channel for the hydrogel membrane is filled with water containing a blue dye for visualisation. The outer dimensions are $13 \times 17.5 \times 1.4 \text{ mm}^3$ [15]_{©2017 IEEE}

3.4.3.2 Vertical concept

The vertical concept requires three wafers: two silicon wafers with the channels, inlets and the membrane and an unstructured glass wafer to close the channels. The main processes are the fabrication of the membrane by anodisation, the dry-etching of the channels and the eutectic bonding of the silicon (see fig. 3.24). [9]

At first, the silicon wafer with the membrane is oxidised to form a 500 nm oxide layer. This layer is coated with $1.8 \mu\text{m}$ AZ1518 photoresist and the oxide is removed by wet-etching in Oxide Etch 7:1 of Honeywell Specialty Chemicals. Immediately, 10 nm of chromium and 200 nm of gold are sputtered on the wafer before native oxide is formed. Otherwise any silicon oxide between the metal and the silicon would hamper the eutectic bonding. $1.8 \mu\text{m}$ of AZ1518 is deposited and patterned on the metal layer and the gold is etched with Au Etch 200 and the chromium with Chrom Etch plus of Candor Chemie GmbH. The photoresist is removed with AZ remover and $2 \mu\text{m}$ of aluminium is sputtered on the wafer. $10 \mu\text{m}$ of AZ9260 is patterned on the aluminium and another layer of AZ9260 is deposited on the back side. Subsequently, the wafer is anodised at 30 V in 0.3 M oxalic acid at room temperature. The silicon of the back side would also be oxidised which is avoided by a layer of photoresist on the back side. After approximately 30 min of anodisation, the current decreases significantly which indicates that the entire aluminium is oxidised. The photoresist is removed with acetone and another $10 \mu\text{m}$ thick layer of AZ9260 is patterned on the back side of the silicon. The developer of the resist is a base and thus attacks the aluminium oxide. However, the etching is much slower

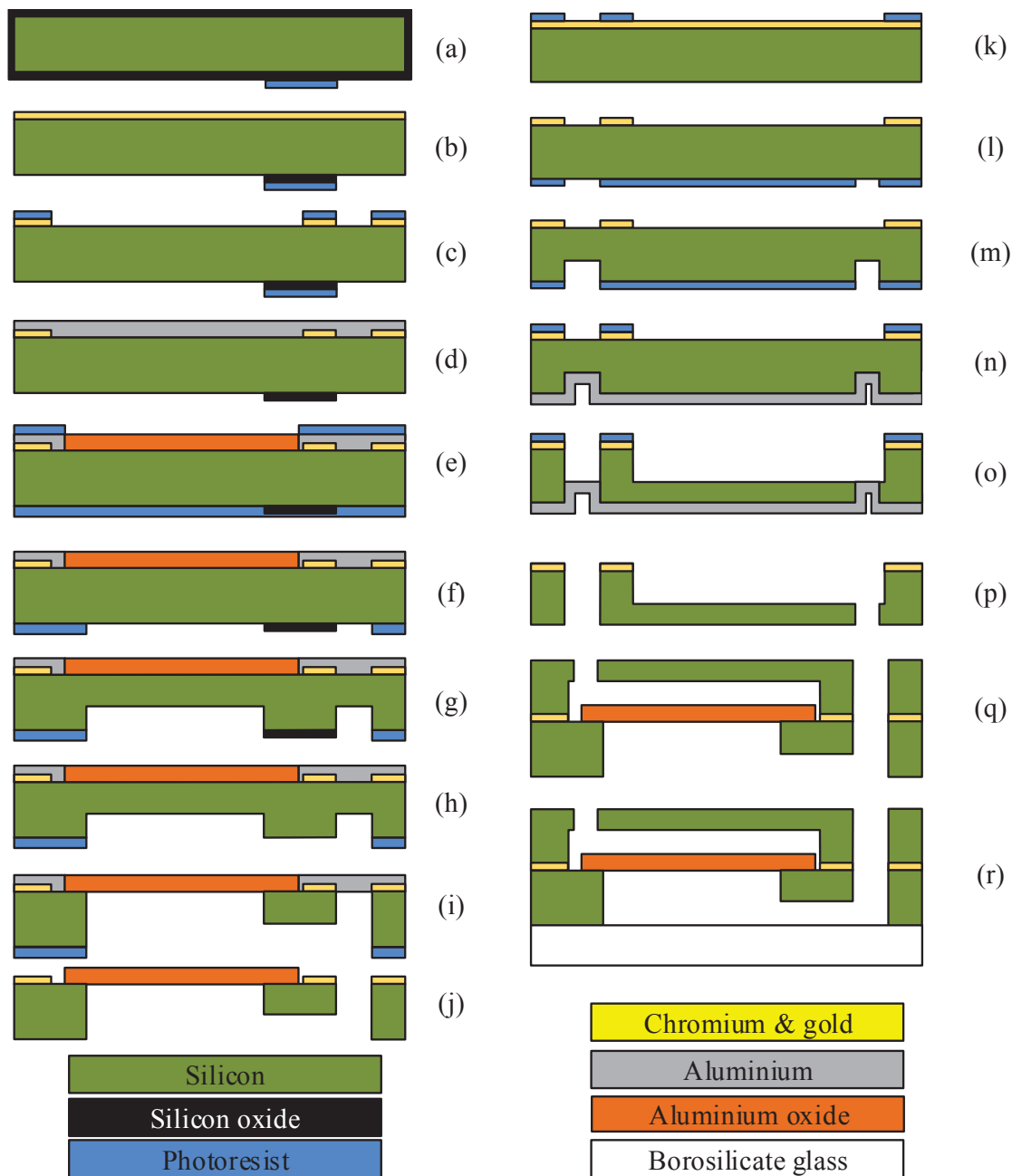


Figure 3.24: Flowchart of the fabrication process for the vertical concept: (a) silicon wafer with 500 nm of SiO₂ and 1.8 μm photoresist (b) wet-etching of the SiO₂ and immediate sputtering of 10 nm chromium and 200 nm gold (c) photolithography and wet-etching of gold and chromium (d) removal of the photoresist and sputtering of 2 μm aluminium (e) 10 μm photoresist on both sides and anodisation (f) 10 μm photoresist (g) 200 μm DRIE-etching (h) dry-etching of SiO₂ (i) 180 μm DRIE-process (j) removal of the resist and of the aluminium and opening of the pores (k) silicon wafer with chromium, gold and photoresist (l) wet-etching of the metals and photolithography (m) 200 μm DRIE-etching (n) sputtering of aluminium and photolithography (o) DRIE-etching (p) removal of the resist and aluminium (q) eutectic bonding (r) anodic bonding with a borosilicate glass wafer.

than the development time so that the damages are minor. Afterwards, the silicon is dry-etched with a DRIE-process. After 200 μm of etching, the oxide is removed with dry-etching before another 180 μm of silicon are removed with a DRIE-process. Finally, the resist is removed with acetone and the remaining aluminium is etched with 1.5 M hydrochloric acid. As a last step, the pores are opened by etching with 0.8 M phosphoric acid for 10 min. Here, it is important to monitor if the pores are already open by SEM-images. If the etching lasts too long, the membrane is etched away. On the other hand, the pores are still closed if the etching is too short.

The native oxide of the second silicon wafer is removed by wet-etching before 10 nm of chromium and 200 nm of gold are deposited. These layers are patterned by wet-etching with a mask of 1.8 μm of AZ1518. The resist is removed with AZ-remover and 10 μm of AZ9260 are added on the back side of the wafer as a mask for the 200 μm deep DRIE-etching of the silicon. Subsequently, the resist is removed and 1 μm of aluminium are sputtered on the structured side. This layer is used as etching stop for the DRIE-etching of the channels also with 10 μm AZ9260 photoresist as mask. Finally, the resist and the aluminium are removed.

In a last step, both silicon wafers are bonded together by eutectic bonding. Here, gold and silicon form an eutectic at 369 $^{\circ}\text{C}$ that bonds both wafers. However, the application of energy either during the sputtering of the aluminium or during the dry-etching of the silicon also results in a thin gold-aluminium-intermetallic, which hampers the eutectic bonding. This intermetallic could be avoided e.g. by a lift-off process of the aluminium on top of the gold directly after its deposition. Nevertheless, the eutectic bonding of the wafers at 500 $^{\circ}\text{C}$ results in a sufficiently strong bonding for most chips. Finally, a borosilicate glass wafer is bonded anodically on the silicon wafer with 600 V at 350 $^{\circ}\text{C}$. Images of the final chip are shown in fig. 3.25.

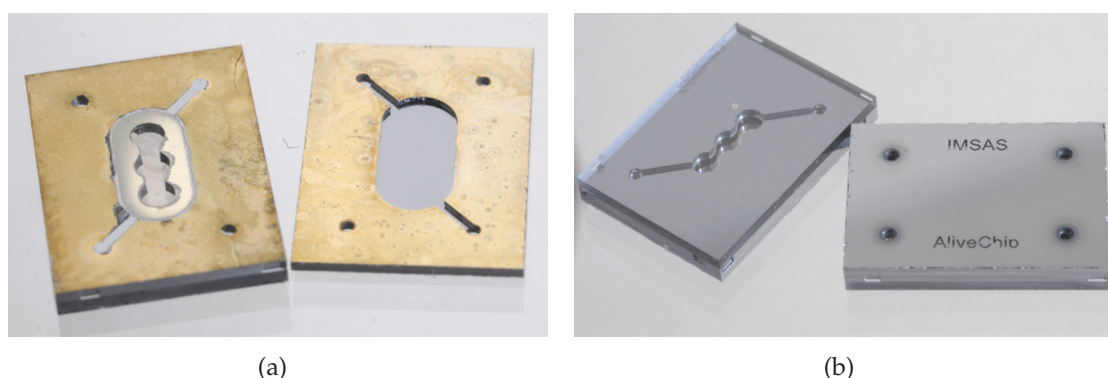


Figure 3.25: Images of two chips with the vertical concept: (a) chip, where the eutectic bonding did not occur (b) front side (left) and back side (right) of a successfully fabricated chip with the outer dimensions of 6.5 x 9 x 1.3 mm^3 . [9]©2018 IEEE

3.4.4 Assembly

The microfluidic chips need to be connected to the macroscopic world. An attractive method are 3D-printed holders which enable an easy assembly for a specific chip design, which is also reversible and thus allows the exchange of the chips. Additionally, these holders are fabricated faster and at lower costs by 3D-printers compared to micromilling or injection moulding [105].

The assembly of the horizontal concept is presented at first in sec. 3.4.4.1 and subsequently, the assembly for the vertical concept is explained in sec. 3.4.4.2. In both cases, the holders are fabricated with stereolithography 3D-printing. To overcome the cytotoxicity of the used materials, the printed holders are coated with Parylene, which is described in sec. 3.4.4.3.

3.4.4.1 Horizontal supply concept

The microfluidic chip as described above is ready to use but difficult to handle. Therefore, 3D-printed holders are designed and realised to facilitate the handling and the filling of the chip. This assembly consists of a bottom and two top parts. The top holders contain three microfluidic reservoirs each, in which the nutrients or suspended cells can be pipetted. The bottom part is used to hold the chip and to enable the clamping. The connection between the chip and the top holder is sealed with small O-rings made out of ethylene propylene-diene monomer rubber (EPDM) and purchased from Parker Hannifin GmbH. These O-rings are chosen because the material is biocompatible and non-cytotoxic. The sealing with O-rings withstands reproducibly a pressure of at least 7 bar without leakage [105]. The assembly with the dimensions $22 \times 29 \times 8 \text{ mm}^3$ is shown in fig. 3.26(a). [14, 105]

Both holder elements are fabricated by 3D-printing out of acrylic plastic (see fig. 3.26(b)). The bottom part is printed with a Form1-printer with the resin Clear01 of Formlabs Inc. The printing of the top holders is done with the resin HTM140 in the Perfactory Micro HiRes from Envisiontec GmbH.

3.4.4.2 Vertical supply concept

The chip for the vertical supply concept is also clamped between two 3D-printed holders (see fig. 3.27). As the inlets into the chip are on the back side, the microfluidic channels are integrated into the bottom holder. Two different bottom holders are designed - one with reservoirs on each side and another one with tubes as connection to the macroscopic world. Both holders are clamped together with four M3 screws. Identical to the assembly of the horizontal concept, the connections are sealed with O-rings. The outer dimensions of the assembly are $22.5 \times 21 \times 7 \text{ mm}^3$. [9]

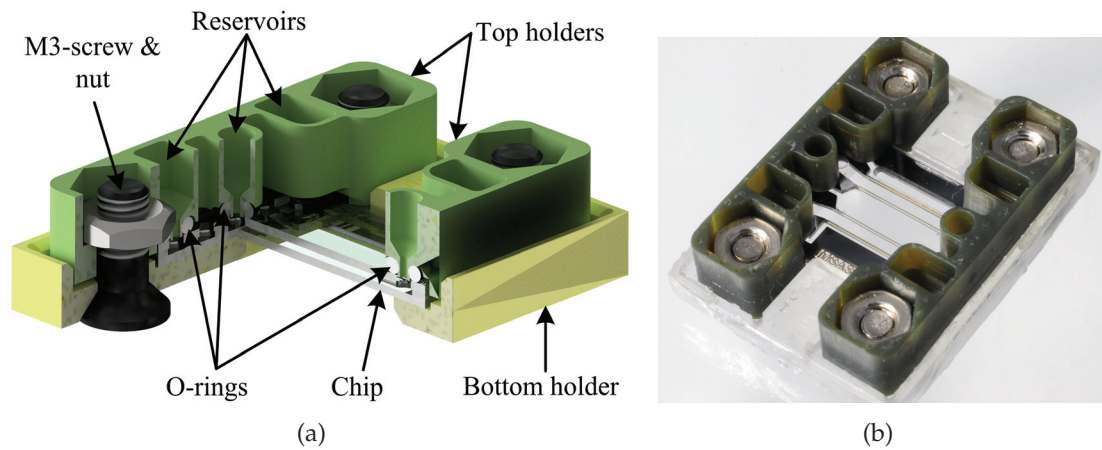


Figure 3.26: Assembly for the horizontal supply concept: (a) CAD-image of the assembly containing the holder structure, the chip as well as sealing and fastening elements (b) photo of the final assembly. [15]_{©2017 IEEE}

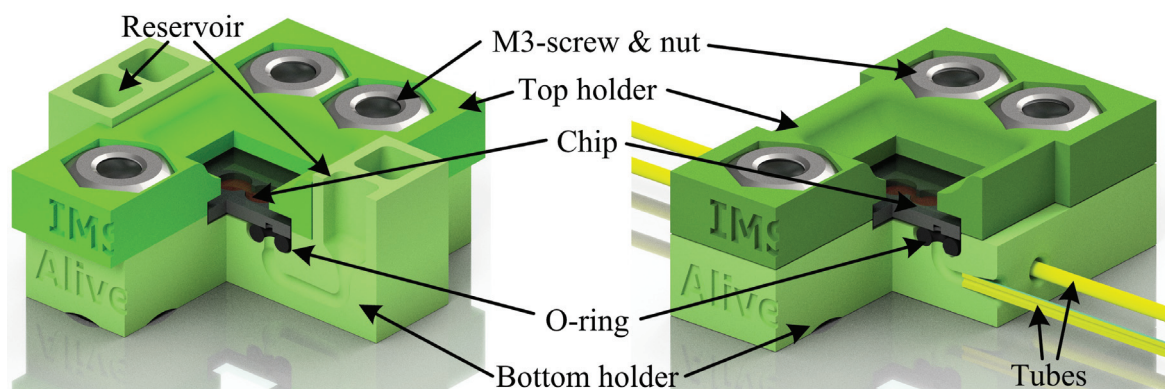


Figure 3.27: CAD-image of the two assemblies for the vertical concept which consists of a chip that is clamped between the holders with O-rings as sealing.

3.4.4.3 Parylene coating

The resins of both 3D-printers are cytotoxic probably due to the high concentration of photoinitiators that leak into the culture media and preclude the proliferation of cells. To prevent this effect, the holders are coated with a 10 μm thick layer of Parylene C. Parylene C is a highly biocompatible and non-cytotoxic polymer [55] that is deposited by a CVD-process, which works even in closed channels with a penetration depth of up to 50 times of the channel height [34]. If several μm are deposited, the film is pinhole-free and thus allows the encapsulation of the toxic material. Therefore, all parts of the assembly that are in contact with the culture media are coated with Parylene to make them biocompatible and non-cytotoxic. [105]

The effectiveness of the coating is verified by cytotoxicity tests with MDCK and HaCaT cells. MDCK cells are cultivated in a well-plate and a holder without (fig. 3.28(a)) and with (fig. 3.28(b)) coating as well as a negative probe without a holder. No living cell can be found in the well with the uncoated holder after 24 h of cultivation. In contrast, no difference is visible between the culture with the coated part (viability 84 %) and the negative sample (viability 85 %). The same effect occurs to HaCaT cells where also all cells die if the liquid is in permanent contact with uncoated parts while the viability is above 95 % for the sample with the parylene coating and the control group [105].

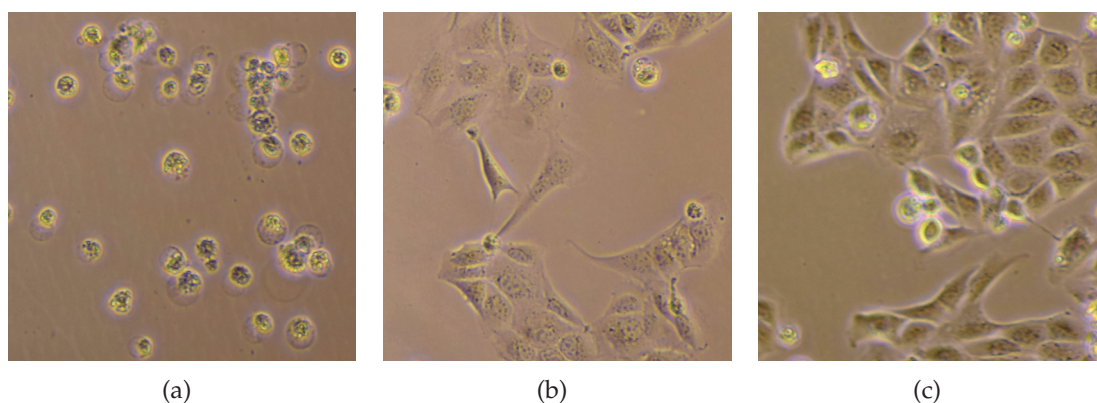


Figure 3.28: Cytotoxicity test over 24 h where a printed holder was immersed in the culture medium of a MDCK cell culture: (a) no cell is alive if the liquid is in contact with the holder after 24 h (b) high cell viability if the holder is coated with 10 μm of Parylene C (c) negative sample without holder. [14]

3.5 Experiments and results

This section presents the conducted experiments and their results. At first, the horizontal supply chip and the vertical supply chip are characterised in sec. 3.5.1 and 3.5.2. The experiments and the results of the 2D-cultivation of mammalian cells inside the chip are discussed in sec. 3.5.3. The horizontal supply concept can also be used for 3D-cell cultivation inside the hydrogel if the design is slightly modified as shown in sec. 3.5.4.

3.5.1 Characterisation of the horizontal supply chip

Sec. 3.4.1.1 described the theoretical design limitations of the surficial phaseguides e.g. regarding the width of the channel. At first, these models and predictions are verified in sec. 3.5.1.1. Furthermore, the diffusion of oxygen through the hydrogel membrane is analysed in sec. 3.5.1.2.

3.5.1.1 Phaseguides

Sec. 3.4.1.1 predicts the design for the wall-less channels based on a theoretical model. Here, the prediction of the width and the (mis-)alignment are verified quantitatively and the intersection with walls qualitatively by experiments. All devices in the experiments are fabricated as described in sec. 3.4.3 and contain 380 μm high channels. [12]

Width of the wall-less channel

The width of the wall-less channel depends mainly on the height of the channel, the contact angle on hydrophilic surfaces and the applied pressure. Considering the contact angle of $16 \pm 2^\circ$, the minimal, theoretical width is $395 \pm 9 \mu\text{m}$ without additional pressure.

For verification, a wall-less channel is designed, in which the width decreases from 1400 μm constantly to 380 μm . Water containing a low concentration of Indigocarmin for a better visualisation is provided at the inlet with $p = 0$ and is pulled into the horizontal aligned chip by capillary pressure. Here, the liquid flows reproducibly into the device until the width is only 390 μm (see fig. 3.29(a)).

In a second experiment, the chip is arranged vertically so that liquid is pulled into the device against gravity and stops at a channel width of 510 μm (see fig. 3.29(b)). In this case, the liquid rises reproducible $8 \pm 0.5 \text{ mm}$ above the liquid level provided at the inlets. Considering the applied pressure of $p = -78.5 \pm 4.9 \text{ Pa}$ due to the gravity, the minimal, theoretical channel width is determined as $502 \pm 15 \mu\text{m}$ (see also sec. 3.4.1.1) and is in very good agreement with the experimental results.

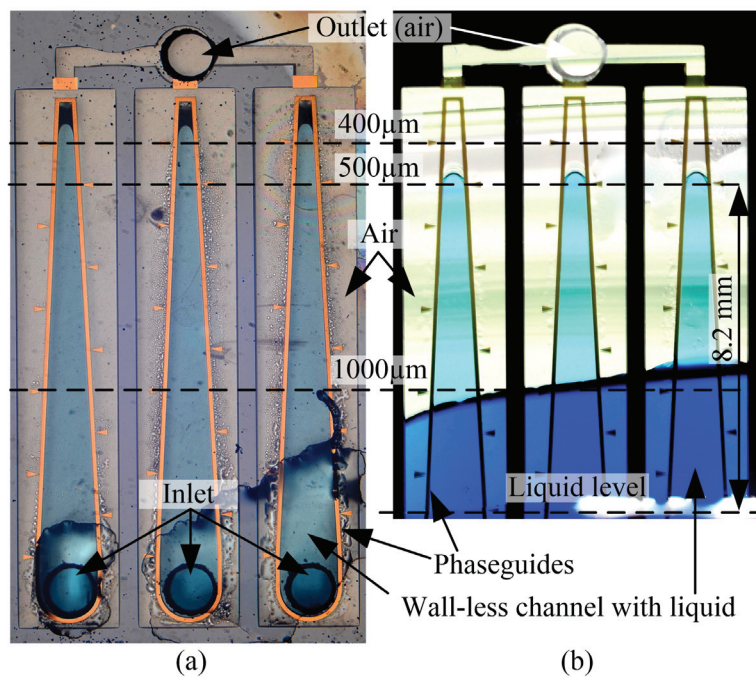


Figure 3.29: Experimental verification of the width of the wall-less channel: (a) horizontal arrangement of the chip ($p = 0$) where water with a blue dye is pulled into the wall-less channel up to the width of approximately $390 \mu\text{m}$ (b) vertical arrangement of the chip, where the liquid is pulled into the wall-less channel against gravity ($p < 0$), in which the minimal channel width is $510 \mu\text{m}$. [12]

Alignment of the phaseguides

The acceptable misalignment between the phaseguides on the bottom and the ceiling depends on the applied pressure, the height and the contact angle of the phaseguides. Without any applied pressure, the maximal, theoretical misalignment for the given dimensions is $184\ \mu\text{m}$.

For verification, a chip is designed, in which the misalignment increases from $0\ \mu\text{m}$ near the inlets up to $500\ \mu\text{m}$ at the end of the $8\ \text{mm}$ long and $1.14\ \text{mm}$ wide channel. Due to the large width, the pressure inside the wall-less channel is negative so that further liquid is pulled into the channel. Water is provided with a rate of $0.1\ \frac{\mu\text{L}}{\text{s}}$. As shown in fig. 3.30, the wall-less channel is stable even for very large misalignments up to $420\ \mu\text{m}$. The determined misalignment is much larger than the predicted value, but the applied pressure in the experiment is negative and thus lower than for the calculated value. Though, the experiments verify the theoretical model.

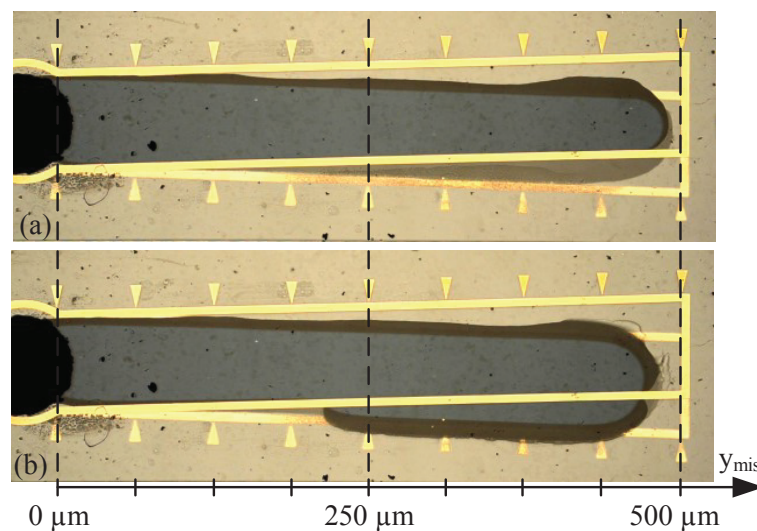


Figure 3.30: Experimental verification of the acceptable misalignment of the wall-less channel: (a) water is pulled into the wall-less channel by the capillary pressure despite the significant and increasing misalignment (b) when the misalignment exceeds $420\ \mu\text{m}$, the liquid flows above the phaseguides. [12]

Intersection with walls

When the wall-less channel intersects with a solid wall, the phaseguides either have to be designed extra wide or the angle of the wall-less channel and the solid wall must be small e.g. by adding tip structures.

Such a tip structure is added on the intersection with the wall as shown in fig. 3.31(a). Here, the tip has an angle of 30° (i.e. $\alpha_w = 15^\circ$) so that the intersection

works reliable. In a second example, the tip is omitted and the liquid flows above the phaseguides for $\alpha_w = 100^\circ$ and $\alpha_w = 80^\circ$ (see fig.3.31(a)) as predicted by the theoretical model.

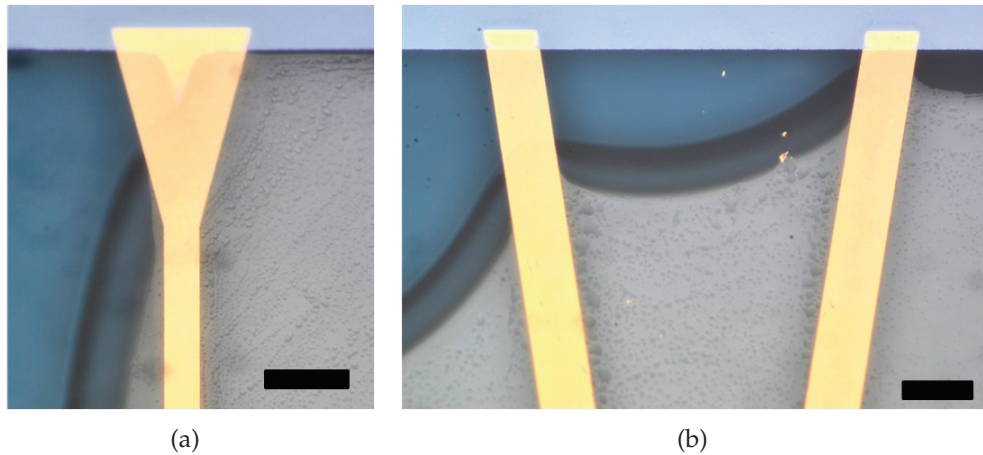


Figure 3.31: Intersection of the phaseguide with the wall (scale bars are 250 μm): (a) a tip is added to the wall ($\alpha_w = 15^\circ$) and the liquid does not flow over the phaseguides (b) the liquid flows over the phaseguides for $\alpha_w = 100^\circ$ on the left and 80° on the right. [12]

3.5.1.2 Oxygen supply

The supply of oxygen by diffusion through the hydrogel is crucial for the cultivation of mammalian cells (see sec. 3.1.3) and limits the width of the culture area (see sec. 3.4.1.2). The direct measurement of oxygen concentration and gradients within microfluidic chips is difficult and would require the integration of sensing elements as described in chapter 4. An alternative is the "blue-bottle-experiment" that can be used as qualitative verification of the oxygen supply and consumption within the chamber. A mixture of 10 $\frac{\text{g}}{\text{L}}$ glucose, 0.5 $\frac{\text{g}}{\text{L}}$ methylene blue and a glycine-NaOH-buffer (pH is 12.6) is filled into the chamber. The glucose is oxidised to gluconic acid while methylene blue is reduced to the colourless leucomethylene blue. In the presence of oxygen, leucomethylene blue is reoxidised to methylene blue. Consequently, the solution consumes oxygen and is blue in the presence and colourless in the absence of oxygen. The reaction speed depends mainly on the pH and thus requires a pH-buffer for constant conditions. The entire reaction is summarised in fig. 3.32. [11]

A membrane of 1 % w/w agarose is made in a microfluidic chip, as described in sec. 3.4.1.3, with a chamber width of 6 mm and the width of the hydrogel of 760 μm . The rest of the chip, which is clamped in a holder (see sec. 3.4.4), is filled with the glucose-methylene-blue-solution as described above (see fig. 3.33(a)). The oxidation

Furthermore, the experiment shows also the stability of the membrane over several hours. Although a small leakage (approximately 2 μL) occurs, the membranes remain intact and provide a stable interface between the liquid and the air.

3.5.2 Characterisation of the vertical supply chip

The vertical supply chip is characterised regarding the pores of the membrane (sec. 3.5.2.1) and regarding the mass transport through the membrane (sec. 3.5.2.2). [9]

3.5.2.1 Properties of the pores

The pores of the membrane are analysed with a SEM prior to the bonding process. The side that is anodised is shown in fig. 3.34(a) and the other side which is revealed by the DRIE-process is given in fig. 3.34(b). The pores of the DRIE-etched side are arranged more regularly in a hexagonal pattern than those on the other side. The higher regularity is caused by the self-ordering mechanism during the anodisation. The diameter of the pores is almost identical on both sides (anodised side: $38 \pm 6 \text{ nm}$, DRIE-side: $39 \pm 5 \text{ nm}$). The porosity, that is the ratio of the area covered with pores to the total area, is about 22 % and similar on both sides. The height of the membrane is determined as 3.3 μm which is an increase of about 65 % regarding the height of the original aluminium layer. The increase in volume is driven by the lower molar volume of aluminium oxide compared to pure aluminium. Furthermore, the inner surface of the membrane is about 75 times higher than its footprint.

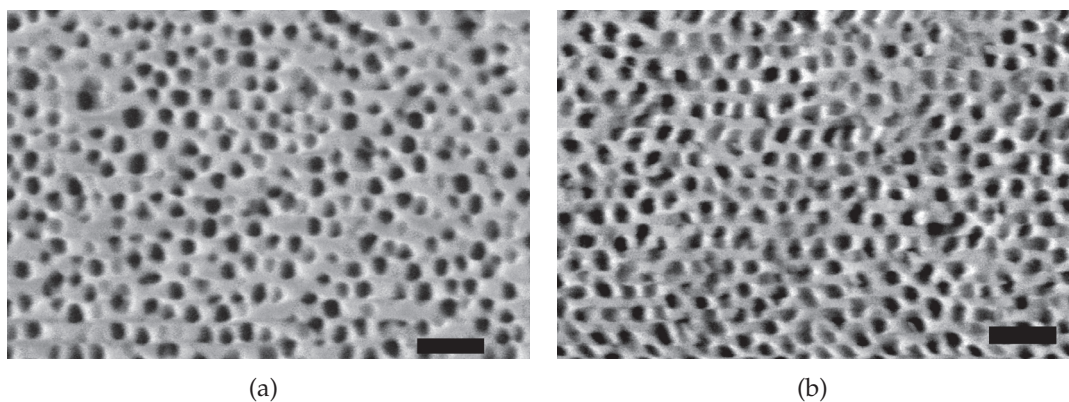


Figure 3.34: SEM images of the membrane (scale bar is 200 nm): (a) anodised side of the membrane (b) DRIE-side of the membrane. [9]^{©2018 IEEE}

3.5.2.2 Diffusion through the membrane

The mass transport through the membrane with a thickness of about $3\ \mu\text{m}$ and $1.5\ \mu\text{m}$ is analysed with indigo carmine, which is a blue dye. Water containing this dye is filled into the upper chamber with a height of $380\ \mu\text{m}$ while pure water is flushed through the lower chamber. The dye diffuses through the membrane and is also flushed away which results in a continuous decolouration. The colour of the chamber is recorded with a camera every 10 s and at three spots with a size of about $0.2\ \text{mm}^2$, the mean value is analysed. Assuming a linear correlation between the colour and the concentration, the decay of the concentration is shown in fig. 3.35.

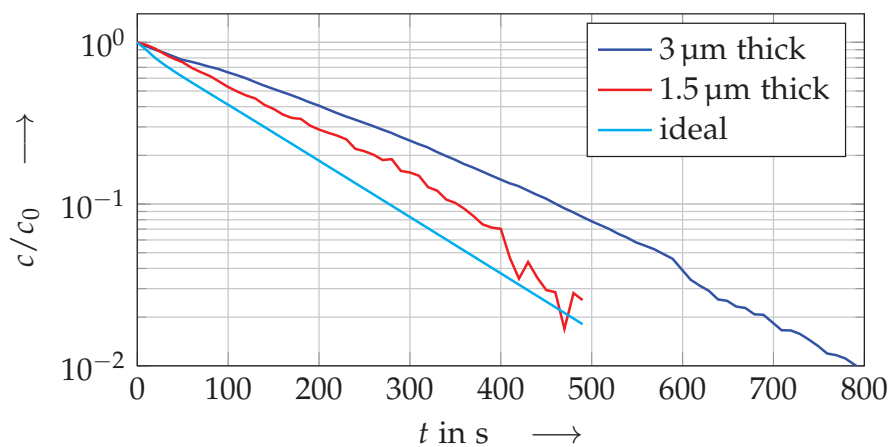


Figure 3.35: Diffusion of indigo carmine from the upper chamber (height $380\ \mu\text{m}$) through the membrane with different thicknesses to the lower chamber where it is flushed away and through an ideal membrane without any diffusive resistance.

95% of the dye are removed within $560 \pm 10\ \text{s}$ in case of the $3\ \mu\text{m}$ membrane and within $410 \pm 10\ \text{s}$ in case of the $1.5\ \mu\text{m}$ membrane. Consequently, the time constants of the diffusion equal $169 \pm 3\ \text{s}$ and $137 \pm 3\ \text{s}$. In comparison, it would take about $365\ \text{s}$ to remove the same amount of the dye by diffusion through an ideal membrane with $0\ \mu\text{m}$ thickness (time constant $121\ \text{s}$).

Considering the thickness of membrane and the height of the chamber, the diffusion coefficient of indigo carmine is determined as $6.7 \pm 0.1 \times 10^{-12}\ \frac{\text{m}^2}{\text{s}}$ ($3\ \mu\text{m}$ membrane) and about $26 \times 10^{-12}\ \frac{\text{m}^2}{\text{s}}$ ($1.5\ \mu\text{m}$ membrane). The diffusion coefficient of the dye through water is $5.5 \times 10^{-10}\ \frac{\text{m}^2}{\text{s}}$ [118]. Considering that only 22% of the membrane are covered with pores, the diffusion coefficient through the pores is approximately 5.7% of the one in water through the thick membrane and about 23% through the thin membrane.

Indigo carmine has a molar mass of $466\ \frac{\text{g}}{\text{mol}}$, which is higher than the mass of all vitamins and at least two times heavier than all proteins of the DMEM-medium

for cell cultivation. Therefore, it can be assumed that the diffusion of all nutrients through the membrane is fast enough to exchange the medium in the chamber sufficiently.

3.5.3 2D-cell cultivation

Both concepts are tested for the cell cultivation purposes. MDCK cells are cultured in the horizontal supply chip (sec. 3.5.3.1) and HaCaT cells in the vertical supply chip (sec. 3.5.3.2).

3.5.3.1 Horizontal supply chip

Before the cell cultivation is carried out, the chip, the O-rings and the top holders are cleaned and sterilised with isopropanol and ethanol. Once the solvents evaporate, the assembly is mounted in a sterile workbench as described in sec. 3.4.4. The hydrogel is prepared by mixing low-gelling agarose with DI-water to a concentration of $10 \frac{\text{g}}{\text{L}}$. The solution is heated up to 100°C in order to melt the gel and to sterilise the hydrogel, before it is cooled down to 50°C . Subsequently, about $6 \mu\text{L}$ of the liquid gel are inserted into each channel and cooled to room temperature to form the hydrogel membranes. [14]

The hydrogel membrane contains a significant amount of water which has to be replaced with culture medium prior to cell seeding. Therefore, the culture chamber and the nutrient channel are filled with fresh medium that is replaced 3 times within 30 min.

The procedure of cell cultivation experiments is summarised in fig. 3.36(a). A solution of MDCK cells in culture medium is inserted into the culture chamber of the device (see fig. 3.36(b)). Because the field of depth of the microscope is lower than the chamber height, not all cells are sharp at the same focus level since they do not settle immediately after filling. After 4 h, the first cells attach on the bottom (fig. 3.36(c)). After 24 h, all cells are attached and show significant proliferation (fig. 3.36(d)).

In order to detach the cells, the culture chamber is filled with TrypLE, which is a solution that contains cell-dissociation enzymes to detach mammalian cells. Therefore, TrypLE is similar to the more common Trypsin but Trypsin is less gentle and harms the cells in case of longer exposure. All compounds diffuse into and out of the hydrogel, which slows down the exchange of the medium. As a consequence, the complete exchange of liquid that would be required after the Trypsin-treatment is not possible, which means that TrypLE is much more appropriate. During the detachment process, the cells change their shape from flat to round as shown in fig. 3.36(e) and fig. 3.36(f) for 12 min and 30 min of TrypLE treatment.

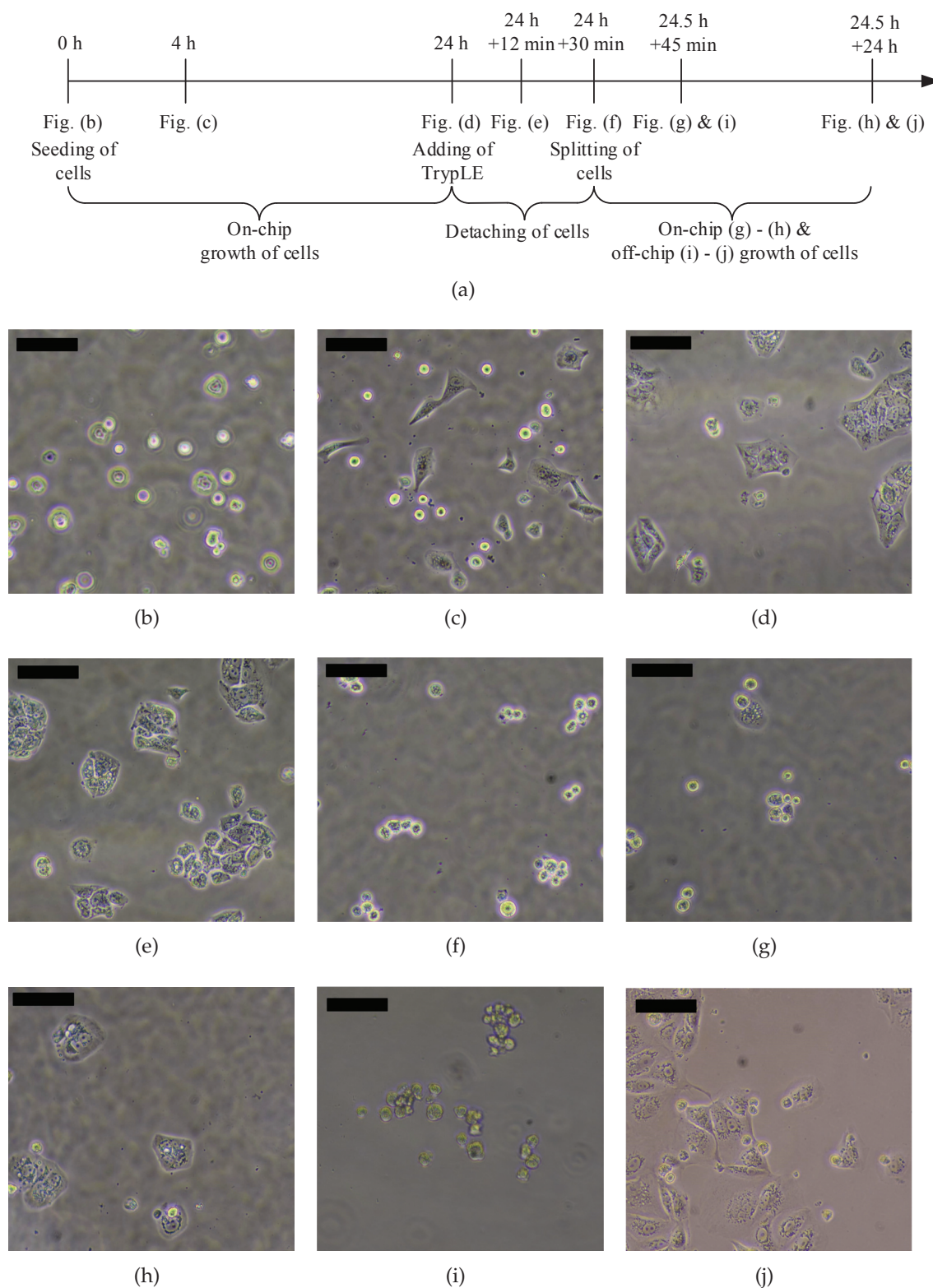


Figure 3.36: Culture of MDCK cells (scale bar is $100\ \mu\text{m}$): (a) overview about the experimental procedure (b) $t = 0$ h: seeding of the cells inside the chip (c) $t = 4$ h: cells adhere on the bottom plate (d) $t = 24$ h: cell growth inside the chamber (e) $t = 24$ h (culture) + 12 min incubation with TrypLE: first cells detach from the plate (f) $t = 24$ h + 30 min incubation with TrypLE: Detaching of almost all cells (g) $t = 24.5$ h + 45 min: A few cells remain inside the chip after the splitting (h) $t = 24.5$ h + 24 h: on-chip growth of the cells (i) $t = 24.5$ h + 45 min: the majority of the cells is removed from the chip after splitting and added in a 24-well plate (j) $t = 24.5$ h + 24 min: off-chip growth of the cells. [14]

After 30 min, approximately 90% of the cells are detached and removed from the chip. These cells are cultivated further on a common well-plate and show a very high viability and growth rate (see fig. 3.36(i) and 3.36(j) 45 min and 24 h after seeding). The remaining cells in the chip (fig. 3.36(g)) are supplied with fresh medium and cultured further. These cells proliferate as well within 24 h (fig. 3.36(h)) after the splitting.

This experiment shows the capability of the horizontal chip for the long-term cell cultivation and the cell passaging. Once the cell adhere on the bottom plate, which occurs a few hours after the filling, the number of cells increases because of the cell division. This indicates the sufficient supply with gases and nutrients as the cells die otherwise. Additionally, the cells survive the detaching process and show a similar growth on-chip and off-chip after splitting.

3.5.3.2 Vertical supply chip

As explained in sec. 3.2.2, the membrane of the vertical supply chip can be used either for diffusion of nutrients or for diffusion of gases. Both ideas are realised below.

Nutrient diffusion

In case of the nutrient diffusion, the lower chamber of the honeycomb design is filled with HaCaT cells and the other chamber with fresh medium. The medium is replaced twice a day to provide fresh medium with sufficient dissolved gas.

2 h after filling the device, the cells are still round and not attached on the membrane (see fig. 3.37(a)). After 20 h of on-chip cultivation, the majority of the cells adhere and start to spread (fig. 3.37(b)). The first colonies are formed after 48 h (see fig. 3.37(c)). Furthermore, cell survival and cell growth are visible which indicate at least sufficient nutrient and gas supply. However, the majority of the cells are dead after 78 h (see fig. 3.37(d)). Additionally, some other cells detach and are flushed away during the medium exchange. Consequently, the number of cells per spot remains constant or decreases (see fig. 3.37(e)) although splitting of some cells is recorded. The reason might be an insufficient supply with oxygen.

Oxygen diffusion

In case of the oxygen diffusion, the cells are seeded into the upper chamber onto the membrane and while the lower chamber remains empty and is thus filled with air containing sufficient CO₂. Here, the chip with a 2 mm wide membrane is used. The medium is replaced twice a day for the first 7 days and once per day afterwards.

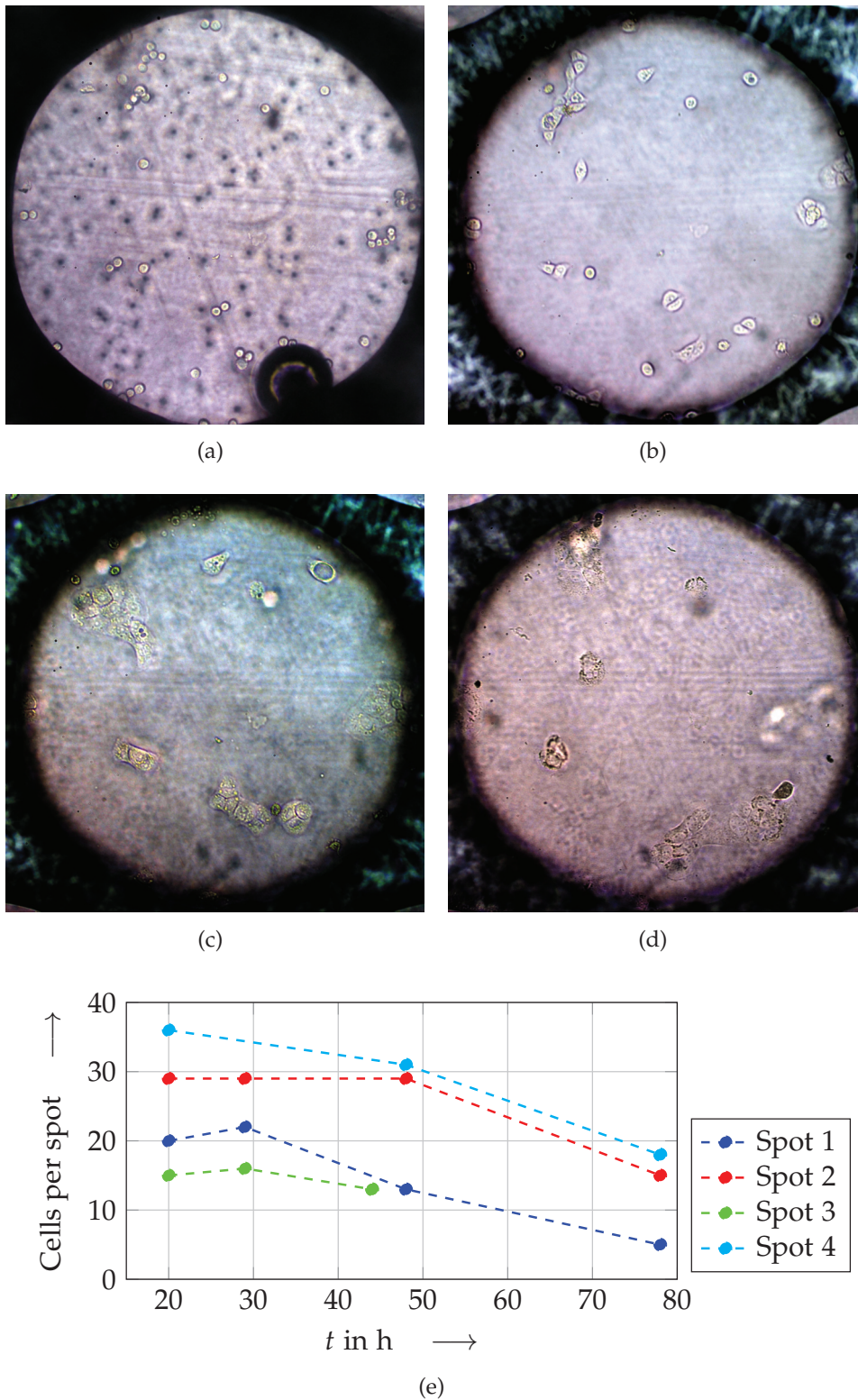


Figure 3.37: Culture of HaCaT cells in the honey-comb chip of the vertical supply concept, in which both chambers are filled with medium and the medium is replaced twice in 24 h (the chamber in each image is 600 μm wide): (a) 2 h after filling the chip (b) cell attachment and growth after 20 h (c) further growth after 48 h (d) cell death after 78 h (e) number of cells during the experiment at four exemplaric spots.

In this experiment, the cells are cultured over two weeks. During this time, the cells show significant growth, which results in large colonies of several hundred cells (see fig. 3.38(a)-3.38(d)). During the first four days, the area covered by the cells increases by approximately 70 % per day (see fig. 3.38(e)). As the colonies become bigger, the growth of the covered area slows down and the cells split less often because of the missing space.

In a reference experiment, HaCaT cells are seeded in a 24-well plate and the growth is observed at a specific spot. Here, the cells grow faster during the first 3 days (increase of approximately 100 % per day) before the growth slows down.

After 14 days of cultivation, the cells are removed from the chip with TrypLE similar to the procedure described earlier (see sec. 3.5.3.1). In contrast to culture flasks, in which the detaching takes about 15 min, the majority of the cells are detached from the membrane after 80 min. This indicates the very good adhesion on the membrane. The removed cells are cultured afterwards successfully in a well plate.

3.5.4 3D-cell cultures

The aim of in-vitro cell cultures is to investigate and manipulate biological processes in a controlled environment. These results are only valid if they can be transferred to the in-vivo behaviour of mammalian cells. Common 2D-cell cultures are easy to handle, to access and provide reproducible conditions. However, the shape of in-vitro cells differs from their in-vivo counterparts, the interactions with the extra-cellular matrix (ECM) are missing, the cell-to-cell interactions are reduced and the mechanical properties of the surfaces differ. As a consequence, the cells in 2D-cultures show discrepancies e.g. in the response to drugs or the over- or underexpression of certain proteins compared to 3D-cultures. [11, 53, 81, 95]

Consequently, 3D-cell cultures are more and more of interest for biological analysis. In this case, the cells are embedded in a matrix out of hydrogel like agarose or collagen to mimic the ECM. Usually, the melted hydrogel containing mammalian cells is filled into the microfluidic chip, where the gelation occurs. All nutrients and gases are supplied by diffusion, meaning that the hydrogel must leave parts of the channel empty which are used later as supply channels. This problem is solved by some authors by using an array of micropillars either inside the hydrogel [108] or on the outer sides of the gel [1, 50]. Here, the liquid fills the region between the pillars at first because of the lower capillary pressure compared to the rest of the chip. Obviously, these pillars reduce the area of the interface to the supply channels and thus hinder the diffusion.

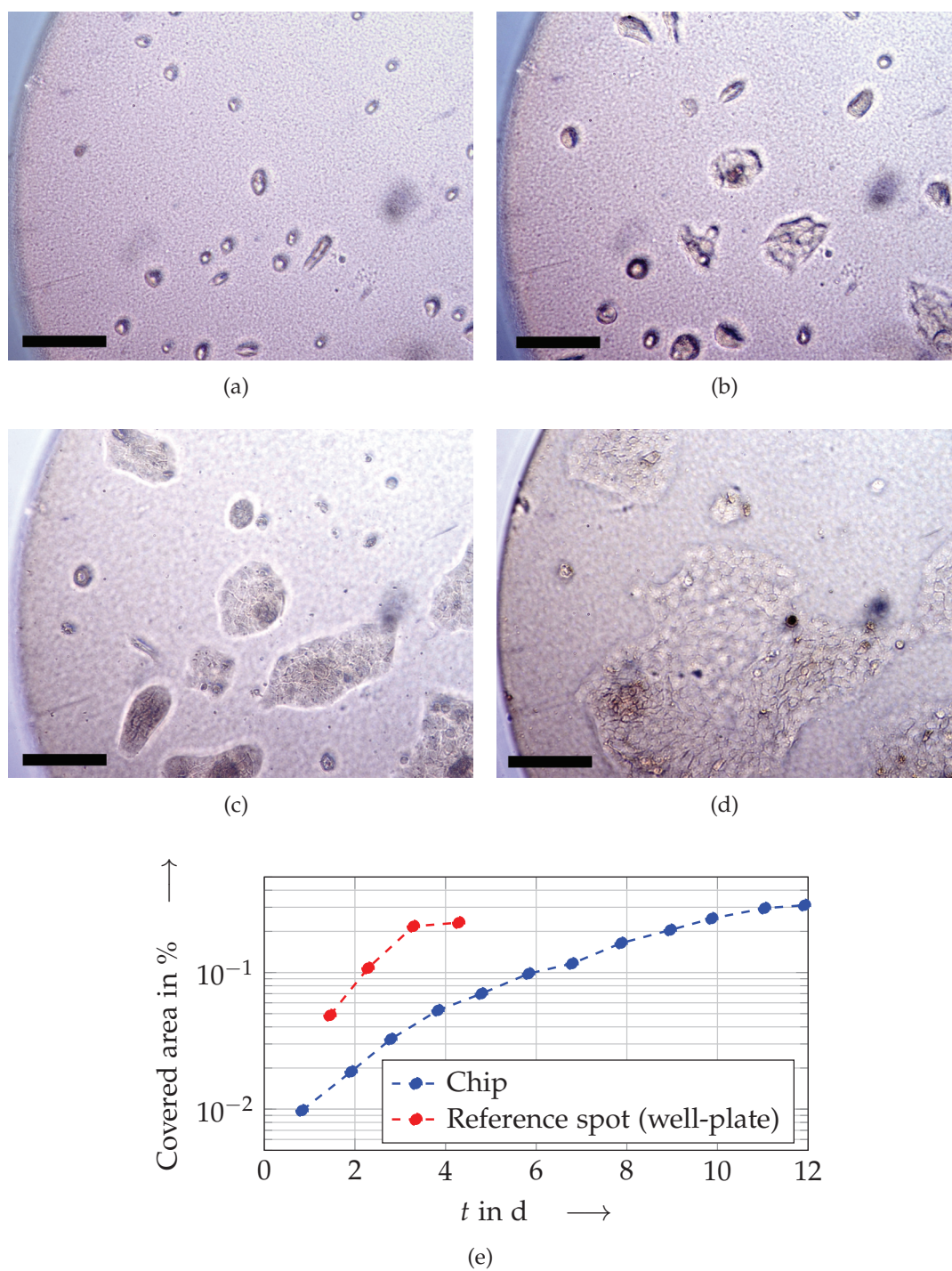


Figure 3.38: Culture of HaCaT cells on the AAO-membrane where the upper chamber is filled with medium that is replaced every day and the lower chamber contains the air of the incubator (scale bar is $200\ \mu\text{m}$): (a) 1 d after seeding (b) 4 d after seeding (c) 8 d after seeding (d) 12 d after seeding (e) area of the membrane that is covered with cells (blue) and a reference spot of a well plate (red).

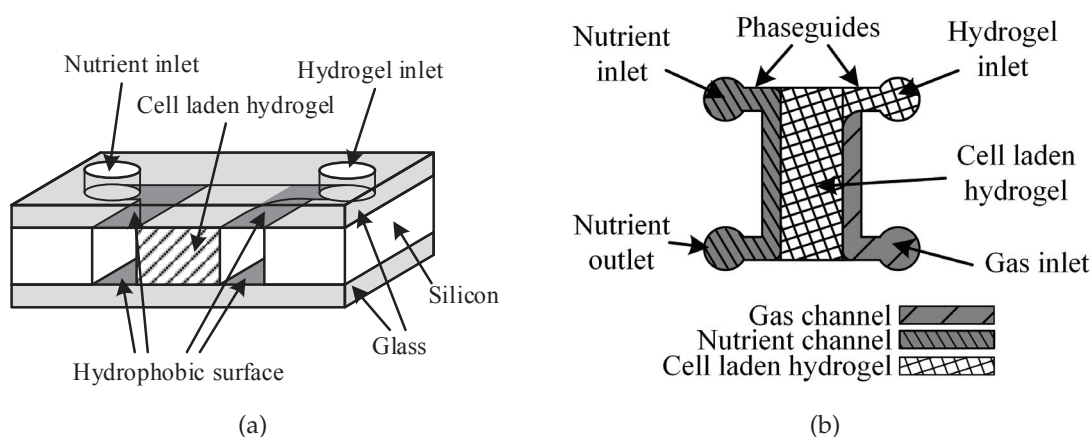


Figure 3.39: Concept of a microfluidic chip for a 3D-cell culture: (a) cross-section showing the arrangement of the phaseguides, the channels and the hydrogel inside the chip (b) top view on the chip. [13]

An attractive alternative to arrays of micropillars is the technology of surficial phaseguides (see sec. 3.3.1.2). Thus, a similar but simplified concept of the horizontal supply (see sec. 3.2.1) can be used as presented in fig. 3.39(a).

Here, only one hydrogel channel is needed and the phaseguides are used directly as channels for the nutrients and gases. Even the separate inlets for the hydrogel are not required by using one inlet of the gas channel (see fig. 3.39(b)) to insert the hydrogel. This channel is completely hydrophobic, but the side walls out of silicon are hydrophilic. So, the liquid hydrogel is pulled into the chip if the inlets are narrow enough so that the capillary pressure is still negative. Once the liquid reaches the hydrophilic hydrogel channel in the middle, this area is filled instead of the gas channel. As soon as the entire 3D-cell culture area is covered with hydrogel, the filling has to be stopped. As a result, the gas channel has only one inlet but no outlet. However, the diffusion of gases inside air is sufficiently fast to provide enough O_2 and CO_2 to the cell culture.

The chip with the outer dimensions of 13 mm by 17.5 mm by 1.4 mm contains two separate chambers for 3D-cell cultures. The channels are 500 μm and the chamber is 2.5 mm wide, and both are 4 mm long. So, the volume of the 3D-cell culture is 2.3 μL . The fabrication of this chip is based on the same processes as described in sec. 3.4.3 with the only difference, that the gold is substituted with platinum. The advantage is that eutectic bonding cannot occur but the platinum requires more intensive cleaning prior to coating the ODT. The final chip is clamped in a holder which is based on the same principle as described in sec. 3.4.4. The assembly and the chip are presented in fig. 3.40.

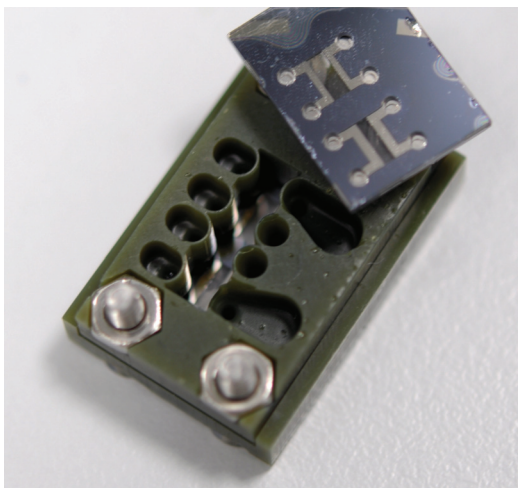


Figure 3.40: Image of the holder and the chip containing two separate microfluidic chambers for the 3D-cell cultures. [13]

As a proof of concept, HaCaT-cells are cultivated in a 3D-cell culture in 1% w/w low gelling agarose. Here, agarose is dissolved in PBS to a concentration of $10 \frac{\text{g}}{\text{L}}$. After melting the gel and cooling it down to 35°C , HaCaT cells are added and the solution is stirred gently. The liquid 3D-cell culture matrix is filled into the chip and the hydrogel gels by cooling it to room temperature (see fig. 3.41(a)). Subsequently, the cells are provided with culture media (here DMEM medium with high glucose, 10% v/v FBS and 1% v/v Penicillin-Streptomycin) and the assembly is placed in an incubator to supply the cells with O_2 , CO_2 and stable temperature. The medium is exchanged every 4 to 8 h.

After 24 h, most of the cells look viable (see fig. 3.41(b)), although the shape of the cells differs significantly from the 2D-cell cultures (see sec. 3.5.3). The viability of the cells is proved by adding TrypanBlue. This dye stains dead cells blue but not viable ones. This test shows that only a low number of cells died either because of insufficient supply or the filling process, which indicates the good growth conditions (see fig. 3.41(c)).

The experiment shows that mammalian cells can be cultured in a 3D-cell culture that is embedded in a matrix out of agarose hydrogel. Compared to the state of the art, this concept with surficial phaseguides provides better growth conditions because the diffusion is not hampered by any obstacles like the micropillars. Furthermore, the gas is supplied directly to the cells instead of using PDMS as gas-permeable, but toxic material. The advantage of 3D-cultures is that they mimic in-vivo conditions better than 2D-cultures. However, the seeding of cells is more difficult and harvesting is even impossible. Furthermore, the optical inspection is also more difficult because the depth of field of common microscopes is narrower

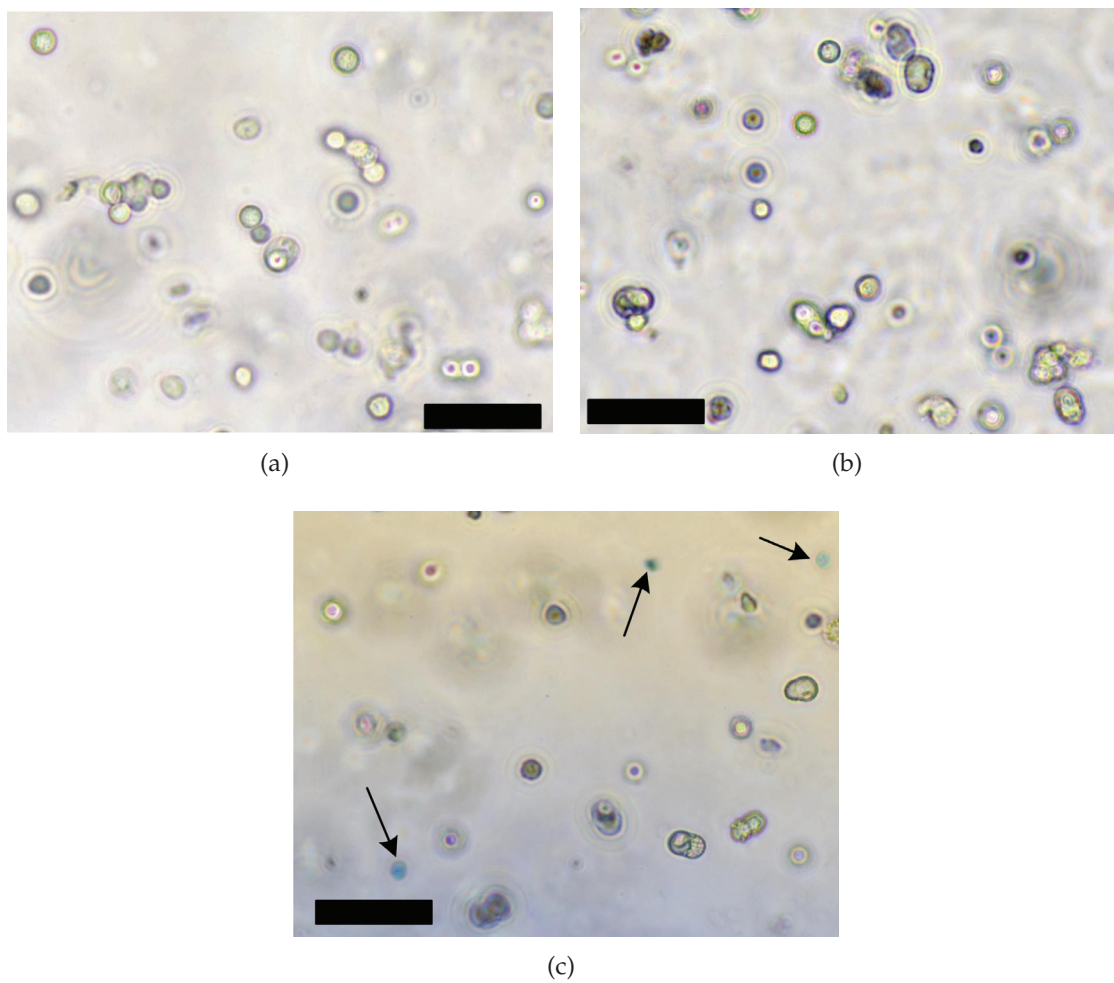


Figure 3.41: Images of HaCaT cells that are cultured in a 3D-cell matrix out of 1 % w/w agarose hydrogel (scale bars are 100 μm): (a) after the gelation of the hydrogel (b) 24 h after seeding the cells (c) staining of dead cells (indicated with an arrow) with TrypanBlue. [13]

than the height of the matrix. Though 3D-cell cultures are an attractive extension of the presented concept of cell cultivation.

3.6 Comparison of both concepts

The horizontal concept and the vertical concept differ regarding the arrangement and the choice of the porous membrane, but follow the same idea of a microfluidic cell culture device out of hard materials with integrated supply structures based on diffusion. The experiments prove that both concepts fulfil the mentioned requirements and enable proliferation as well as passaging of mammalian cells. Though, there are a few differences regarding the applicability as discussed below.

Supply of the cells

In the horizontal concept, the supply of gases and nutrients is separated which allows good and individual controllability regarding the supply rates and the composition. However, the diffusion distances are rather long (up to several mm), which results in slow exchange times but also in gradients. The gradient implies that cells that are close to the gas channel experience higher oxygen concentrations but worse nutrient supply and worse removal of metabolic waste compared to cells next to the nutrient channel. Likewise, the cultured conditions are not uniform within the chamber. The gradient depends on the supply rates and concentrations but also on the metabolism of the cells and on the number of the cells. Consequently, the gradient is hard to control externally. However, a low filling factor and thus a low number of cells results in only small differences of the supply which does not affect cell growth for most applications.

The vertical concept contains only one membrane in order to facilitate the fabrication. Hence, either gases diffuse through the membrane and the medium is exchanged by perfusion or the gas is dissolved and diffuses together with the nutrients through the membrane. In both cases, the supply is very uniform and short diffusion distances favour fast exchange times of seconds up to several minutes. Though, the degree of freedom regarding the supply schemes is reduced due to the missing second supply channel. However, it is feasible to integrate an additional membrane and chamber to overcome this disadvantage.

Scalability

The cultivation area of the presented horizontal concept (24 mm²) is larger than of the vertical concept (6.4 mm²). The chamber width of the horizontal concept is limited by the diffusion of oxygen. It could be designed wider e.g. in case of a

higher chamber or thinner hydrogels but the margin is very narrow. The length of the chamber might be extended as desired. However, this dimension is limited by the robustness of the hydrogel membrane for which its risk of failure due to breaking increases with the length.

The limiting parameter for scaling of the vertical concept is the stability of the membrane as well. Large membranes are more likely to break during the fabrication or due to pressure differences between the chambers. A possible solution is the usage of a support structure, as in the honeycomb-design, or a thicker membrane.

Downscaling, i.e. the fabrication of smaller devices, is easily possible with both concepts.

Tunability of the membrane

The properties of the hydrogel membrane are hard to tune. The concentration and the cooling rate influence the mechanical stability and the pore size. However, tuning the cooling rate is relatively difficult because of the small dimensions and the bad accessibility for cooling aggregates. Moreover, the stability and the pore size are hard to determine on-chip.

The pore size of AAO-membranes can be easily manipulated during the fabrication, as described in sec. 3.3.2.3. Furthermore, the cell adhesion can be improved with coatings like poly-L-lysine by rinsing the chip prior to the cultivation [7].

Fabrication

The fabrication of both concepts is based on standard clean room processes. Both designs are based on a sandwich structure of three wafers. However, the horizontal concept is easier and thus cheaper to fabricate because the bottom layer contains only metal elements, the middle only dry-etched structures and the top layer metal elements and powder blasted inlets. In this concept, the microfluidic channels are all in one layer which benefits more of the 2D-character of MEMS-processes.

The vertical concept is based on four dry-etching processes that result in three layers with different microfluidic elements. Consequently, the fabrication of this design is more expensive and time consuming. However, it must be mentioned that fabrication and integration of the membrane of this concept is part of the fabrication process which lowers the efforts during usage (see ease of use).

Materials

The chips of both concepts are made out of non-cytotoxic materials such as silicon, glass, gold, agarose hydrogel and aluminium oxide. The horizontal concept contains in addition a hydrophobic coating of ODT, for which neither positive nor negative results are reported in the literature. However, this coating is only a monolayer

meaning the amount of ODT in the chip is very low. During the experiments, the contact angle remains stable over several weeks unless high temperatures or aggressive chemicals are used. Hence, it can be assumed that ODT does not dissolve in the cell culture and will thus not harm the cells.

The chips of the vertical concept did also contain pure aluminium in the first process steps that is known to be cytotoxic. However, remaining aluminium is removed by wet-etching so that the devices are aluminium-free during the experiments.

The resin of the 3D-printed holder has a strong impact on the cell growth. However, this effect is overcome by coating the parts with Parlyene. Consequently, the culture medium is not in contact with any cytotoxic material, which is essential for successful cell cultivation.

Ease of use

Several preparation steps are required prior to cultivate cells in the horizontal supply chip. First of all, the concept of surficial phaseguides needs clean surfaces. After cleaning with isopropanol in an ultrasonic bath, the hydrophobic elements need to be refreshed by rinsing with octadecanethiol. Subsequently, the chip has to be rinsed again with DI-water to remove any remaining isopropanol. Finally, the melted agarose is filled into the chip and the chip is ready to be used after the gelation. However, the hydrogel membrane has a high risk of breaking or detaching from the surface in case of a pressure difference between both sides of the membrane. Therefore, the chip has to be filled and handled gently.

The chip for the vertical supply already contains the membrane after fabrication. Consequently, the chip has to be sterilised e.g. by heat or rinsing with isopropanol or ethanol. Furthermore, the membrane is more stable compared to the hydrogel membrane. Though, care has to be taken to avoid breakage of the membrane because of pressure differences. Further care is required to avoid air bubbles. Especially the honeycomb design has a high risk that an air bubble is trapped in one or two combs. Though air bubbles store oxygen, trapping a bubble is no solution for long-term gas supply due to the limited volume. For example, if one out of 19 combs of the honeycomb design is filled with air, the amount of oxygen inside the chip, that is thus available for the mammalian cells, is increased by 200 %, which means that the medium exchange would be required e.g. after 3 h instead of 1 h.

Reusability

The horizontal concept chip can be reused several times. The hydrogel is removed by heating the chip and melting the membrane. After the following cleaning steps, the chip is ready to be used again. Consequently, reusing of the chips is possible.

The vertical concept chip can also be reused as long as the membrane remains intact. Ideally, the cell residues are removed with TrypLE that detaches the cell membranes from the chip so that they can be flushed away. The remaining residuals can be removed with a diluted solution of chlorine cleaner. However, the repair or renewal of the membrane in case of damage is not possible.

3.7 Conclusion

Mammalian cells consume gases and nutrients for their metabolism. As the volumes of on-chip cell cultures are much lower than the traditional cultures, the gases and nutrients have to be refreshed in the range of hours instead of days. Two concepts for on-chip cell cultures with integrated supply structures are shown, for which the supply is based on diffusion. Diffusion-based systems are advantageous compared to perfusion systems as the chemical environment, including messenger signals, is not flushed away and any mechanical stress on the cells is avoided.

Diffusion based supply systems require the integration of one or ideally two porous membranes inside the microfluidic chip. These membranes can be arranged either vertically where the supply takes place horizontally (horizontal supply concept) or vice versa (vertical supply concept). Suitable materials are either agarose hydrogels, anodised aluminium oxide or silica aerogels. The hydrogels benefit of their easy on-chip fabrication method, based on the concept of surficial phaseguides. These surficial phaseguides are an attractive way to integrate the hydrogel membrane while maintaining maximal diffusion rates due to the maximal diffusion cross-section and the relatively thin membranes. The design and the dimensions of the phaseguides are given by analytical considerations and are verified experimentally. AAO is integrated on a wafer scale and is promising due to its easy control of the pore properties and the very thin membrane. The integration for silica aerogels is not realised for the proposed devices because the fabrication is more complex. Though, these aerogels are well suited for the gas-liquid interface and could replace other membrane materials in future applications.

The key factor of the horizontal concept is the design of the chamber and the fabrication of the hydrophobic elements. The width of the chamber is limited by the diffusion distances of oxygen. The maximal width depends mainly on the filling factor and on the height of the chamber as proven by the analytical model of the chip. In contrast, the key factor of the vertical concept is the fabrication based on the anodisation, several dry-etching steps and the eutectic wafer bonding.

The cell cultivation experiments show the successful realisation of both concepts. Both chip concepts enable the entire passaging of seeding, cell growth as a result

of feeding with nutrients and gases and removal of the cells. The vertical concept allows two different application modes - either the oxygen diffusion or the nutrient diffusion. In case of the latter option, the cells are supplied only by dissolved oxygen from the culture medium. In corresponding experiment, the number of cells decreases and the cells die probably because of insufficient oxygen supply. In contrast, the HaCaT cells grow continuously in case of the oxygen diffusion and the covered area increases by 31 times within 12 days. Consequently, the continuous supply of oxygen is more important for the survival of the cells than the continuous supply of nutrients. The cells in the well-plate grow faster than on the AAO-membrane. A reason might be the strong adherence of the cells on the porous membrane, which reduces the spreading of the cells. While the reduced growth rate might be negative for some experiments, the strong adhesion is advantageous in other cases.

The horizontal concept benefits from the easy fabrication and from the integration of two membranes. Yet, the supply with gases and nutrients result in a gradient. The vertical concept requires a more complex fabrication, although the concept is simplified by using only one membrane, but it is easier to use and provides a uniform supply.

Both concepts follow a different idea than the state of the art because the long-term cultivation is based solely on diffusive supply through porous materials inside a chip out of hard materials instead of using PDMS. PDMS, an often used material in academic research, has some disadvantages such as the absorption of small molecules, cytotoxic components that harm the cells and the infeasibility for mass-production. Therefore, the presented concepts are based on hard materials that are non-cytotoxic and enable a mass production with standard clean room processes. Thus, both concepts have their right to exist and the choice of the proper concept depends on the final application.

3.8 Outlook

Both concepts are a significant progress towards the ideal LoC cell cultivation. However, the following issues might be addressed before the concepts are combined with analysis methods and used in applications of biological or medical research.

Adhesion of the hydrogel membrane

In the horizontal supply concept, the agarose hydrogel adheres on the glass plates. However, the adhesion is relatively weak so that the membrane is prone to peel off and move sideways in case of a pressure difference. Due to the low strength

of the hydrogel, the membrane is likely to break once it is bended. A solution is either to use an adhesion promoter or to integrate a support structure. The adhesion promoter has the advantage that the diffusion is not hampered. However, such a promoter must not interfere with the hydrophobic phaseguides and must not harm the cells or hamper the adhesion of cells on the glass.

The integration of a support structure could absorb the load on the hydrogel and keep it in place. These elements could be integrated with 2-photon-polymerisation similar to 3D-printing techniques which allows unlimited designs, but the non-cytotoxicity and the interference with the surficial phaseguides have to be analysed at first. An alternative is to fabricate the elements by dry-etching. In this case, the silicon layer is bonded on the patterned glass wafer. Subsequently, the silicon is structured by dry-etching and e.g. pillars are arranged in the middle of the hydrogel membrane. Occurring problems might be notching during the DRIE-process and the interaction with the surficial phaseguides. Furthermore, both integration methods reduce the diffusion because the cross-section for the diffusion is smaller.

Coating of AAO

The HaCaT cells adhere very well on the AAO-surface as proven by the very slow detaching. However, it also takes more time until they start to adhere. This might be overcome by coating of the surface e.g. with poly-L-lysine. Some other cell types require such a coating. [7] A coating of porous materials with hydrogels also reduces e.g. biofouling and improves the filtration properties [54]. For the presented purpose of cell cultivation, the cells might adhere better on a thin hydrogel layer, e.g. out of collagen, and the device could be cleaned easier by removing the hydrogel.

Integration of a heating element

The presented concepts contains integrated supply structures. However, there is no control of temperature, so that the devices were placed inside an incubator to maintain the temperature of 37 °C. Consequently, an heating element and ideally also a temperature sensor should be integrated in order to realise proper LoCs, for which as much external equipment as possible is avoided. An easy integration method is to pattern heating elements out of platinum on the back side. This approach is described in the following chapter (sec. 4.3.2).

Porous membrane out of silica aerogels

As mentioned above, the hydrogel membrane lacks stability and shows slight leakage in case of the interface to the gas. These problems might be solved by using membranes out of silica aerogel, instead of the hydrogel. However, future work is required to achieve a robust and easy integration of these aerogels.

4 Cell Monitoring: Measurement of the Oxygen Consumption Rate of Cells

Various parameters of living mammalian cells can be analysed inside a microfluidic device. In this thesis, the focus is laid on the measurement of oxygen consumption that indicates cell respiration, which is one of the most important processes of living cells. This analysis is based on the measurement of dissolved oxygen with a photoluminescent sensing principle.

Sec. 4.1 explains the theoretical background of such a sensing scheme, different read-out methods and the sensing materials. Backed by these frame conditions, the concept including the requirements is described in sec. 4.2. Based on these ideas, sec. 4.3 expresses the implementation, thus, the detailed design, the fabrication, the entire assembly and the electronics. Subsequently, sec. 4.4 shows the characterisation of the device and the results of experiments with cells. Finally, the conclusion are drawn in sec. 4.5.

The presented concept and results are based on the following publications:

- S. van den Driesche, F. Lucklum, F. Bunge, M. J. Vellekoop. 3D printing solutions for microfluidic chip-to-world connections. *Micromachines*, 9(2):71, 2018 [105]
- F. Bunge, S. van den Driesche, A. Waite, U. Mirastschijski, M. J. Vellekoop. μ respirometer to determine the oxygen consumption rate of mammalian cells in a microfluidic cell culture. *Proc. IEEE MEMS*, 2017. [16]
- F. Bunge, S. van den Driesche, A. Waite, U. Mirastschijski, M. J. Vellekoop. Microfluidic oxygen sensor based on silica gels for longterm experiments. *Proc. IEEE MEMS*, 2018. [17]

Furthermore, the phase shift read-out method and its results have been developed during the master project of Camilla Konermann from April to October 2017, that was supervised by the author.

4.1 Theoretical background

In this section, an overview of the theoretical background in general is given. At first, the sensing principle is described in sec. 4.1.1. The main properties regarding the cross-sensitivity and the temperature dependency are summarised in sec. 4.1.2. The sensing principle allows the application of different read-out methods as explained in sec. 4.1.3. Last but not least, a summary about the different sensing dyes, that might be used (sec. 4.1.4) is presented, as well as the matrices, in which the dye is embedded (sec. 4.1.5).

4.1.1 Principle of photoluminescent oxygen sensing

Photoluminescence describes the physical effect of light emission after the absorption of a photon. This absorption excites the molecule from ground state (S_0) to a higher state (S_1) within femtoseconds. The transition back to the ground state might occur on the direct way within nanoseconds which is called fluorescence (see fig. 4.1). In this case, the wavelength of the emitted light is close (but higher) to the absorbed light. In contrast, the phosphorescence occurs by the transition via an intermediate energy level. This process takes more time than fluorescence (in the range of microseconds to several seconds). At the same time, the Stoke's shift, which describes the difference between absorbed wavelength and emitted wavelength, is higher. [84]

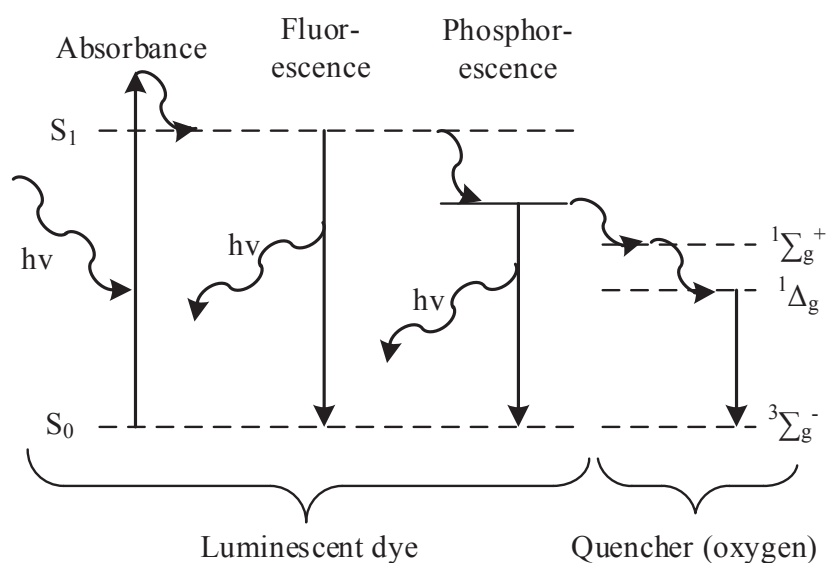


Figure 4.1: Jablonski-diagram showing energy levels of the participating molecules during fluorescence, phosphorescence and quenching.

Some phosphorescent dyes are sensitive to oxygen. That means, that oxygen quenches the excited molecules which is then recovered to its ground state without light emission after the energy transfer to the quencher. Consequently, the oxygen gets excited and converted to the so-called singlet oxygen. This means, that two electrons, that are on the same orbital but with different spin in the ground state ($^3\Sigma_g^-$), are now in two separate, degenerated orbitals, either with the same ($^1\Delta_g$) or a different spin ($^1\Sigma_g^+$). The excited oxygen releases its energy either by emitting IR-light or by chemical reactions (i.e. photo-oxidation). In any case, the phosphorescent dye does not emit light after the quenching, meaning that the intensity and the lifetime of the luminescence decreases with increasing oxygen concentrations. [84]

4.1.2 Sensor properties

The sensitive dyes are not only quenched by oxygen but also by various other substances like gases (Cl_2 , I_2 , Br_2 , SO_3 , NO_x), ions (Br^- , I^- , SO_4^{2-}) and water (especially water vapour). For the targeted application, these gases are only present as trace elements and thus do not influence the measurement. The cross-sensitivity to water and the dissolved ions is eliminated by embedding the dye in a hydrophobic matrix [113]. Because this matrix has to be porous at the same time, water is not absorbed, which means that the pores contain only gases. This results in the following consequences:

- The oxygen has to be dissolved from the liquid sample into the gas of the pores and diffuse into the porous matrix. This diffusion takes time and results in a much slower response time between milliseconds and several seconds compared to the lifetime of the phosphorescence.
- The sensor measures the gaseous oxygen and not the dissolved one. Therefore, the phosphorescence depends on the partial pressure p_{O_2} . The dissolved concentration is $c_{\text{O}_2} = k_{d\text{O}_2} p_{\text{O}_2}$, where $k_{d\text{O}_2}$ is the solubility that depends on the temperature and the ionic strength [103]. As an example, c_{O_2} decreases from $9.1 \frac{\text{mg}}{\text{L}}$ to $6.8 \frac{\text{mg}}{\text{L}}$ in DI-water when the temperature increases from 20°C to 37°C while the partial pressure remains constant.
- The sensing dye is embedded in the porous matrix so that the sensing takes place in the entire volume and not only on the small interface between the film and the liquid. Consequently, the sensor could be considered as "functionalised volume" and thus avoids typical problems of functionalised surfaces, such as low stability, high susceptibility for contamination, low sensitivity, etc.

The phosphorescence of oxygen sensors is also influenced by the temperature. This dependency is based on different physical effects like lower luminescence,

higher quenching constants, lower solubility of oxygen in the matrix, but faster diffusion of oxygen in case of increasing temperatures. These effects differ for every dye and also for every matrix, making a general statement impossible. Therefore, the sensor has to be calibrated at different temperatures and the temperature has to be known during the final experiments. [113]

4.1.3 Read-out methods

Basically, there are two different read-out methods to sense the oxygen via the fluorescence: the measurement of the intensity I and of the lifetime τ . Both parameters increase with decreasing oxygen concentration as described with the Stern-Volmer equation:

$$\frac{I_0}{I} = \frac{\tau_0}{\tau} = 1 + K_{sv}c_{O_2}, \quad (4.1)$$

where I and I_0 are the intensities with and without oxygen, τ and τ_0 are the lifetimes with and without oxygen, K_{sv} is the Stern-Volmer quenching constant and c_{O_2} is the concentration of oxygen.

The measurement of the intensity is the most common method used in academics due to its simplicity. The intensity is measured either with a photodiode or with a camera in order to get information about the two-dimensional distribution of oxygen. However, this method has some disadvantages. First of all, the emitted light depends on the absorbed light meaning that changes of the background light or excitation light source lead to measurement errors. This effect might be levelled out by using a second dye that absorbs at the same wavelength but emits light at a different wavelength. Consequently, the ratio of the both dyes is used to determine the oxygen concentration [104]. Furthermore, the sensitive film shows a slight photodegradation [31] and the results are also influenced by the autofluorescence of other particles (e.g. bacteria) or materials of the setup.

In contrast, the determination of the lifetime requires a more complex setup. The lifetime results in a delay of the luminescence after excitation. Therefore, the phase delay could be measured that occurs for harmonic excitation [19]. In case of the dye Platinum tetrakis(pentafluorophenyl)porphyrin (PtTFPP), a phase shift of 30° between oxygen saturated water and water without oxygen was determined by *Chatni et al.* [19]. The phase delay φ and the lifetime τ correlate with the frequency f as

$$\tau = \tan \frac{\varphi}{2\pi f}. \quad (4.2)$$

Alternatively, the sensitive film could be excited with pulses and the decay is measured directly [78].

In general, the lifetime measurements overcome the disadvantages of intensity measurements. However, such a sensor requires higher brightness of the film than the intensity read-out in order to get a high signal-to-noise ratio because the sensing time is limited to a few ms. Furthermore, receiving a spatial resolution of the oxygen concentration is difficult unless sophisticated cameras are used [23].

4.1.4 Sensing dyes

At the moment, more than 100 dyes are known for which the luminescence depends on the presence of oxygen. Basically, there are different groups of such dyes [84, 113]:

- Polycyclic aromatic hydrocarbons (PAH): PAH, especially pyrene and its derivatives, possess a lifetime in the range of 200 ns, high quantum yield and good sensitivity. However, there is a lack of stability, because the dye usually diffuses out of the matrix and evaporates, resulting in a degradation of the luminescence.
- Fullerenes: Fullerenes C_{70} shows a thermally activated E-type delayed fluorescence which is used in oxygen sensors for very low concentrations down to ppb. The quantum yield is fairly low, but the decay time is very high with values up to 20 ms.
- Transition metal polypyridyl complexes: The most common transition metal of these complexes are Ru(II) and here especially tris(4,7-diphenyl-1,10-phenanthroline) ruthenium (II) complex ($[Ru(dpp)_3]^{2+}$). The lifetime is around 6.4 μs and the luminescence relatively bright (quantum yield around 0.3). $[Ru(dpp)_3]^{2+}$ absorbs light of 400-480 nm and emits above 600 nm. However, the resolution is usually rather low because of the limited stability and low sensitivity.
- Metalloporphyrins: The most common oxygen sensitive dyes are Pt(II) and Pd(II) porphyrins due to their strong phosphorescence and large difference between absorption and emitting wavelength. Platinum tetrakis(pentafluorophenyl)porphyrin (PtTFPP) shows a very high photostability, and thus good stability in general.
- Cyclometallated complexes: Common examples of these complexes contain Ir(III) or Pt(II), which have a high quantum yield but usually require excitation with the UV-A or UV-B light.

- Other with various central atoms, that are rarely used: In contrast to the mentioned dyes, there are other complexes with aluminium, copper, lead or gold that possess also oxygen dependent luminescence. These dyes are usually less expensive compared to platinum or palladium complexes, but show worse performance.

Although many substances could be used for oxygen sensing, only Pt(II) and Pd(II) complexes with some porphyrins including OEP and TFPP as well as $[\text{Ru}(\text{dpp})_3]^{2+}$ are commercially available at reasonable prices. [84]

A direct comparison between two dyes is difficult as the sensing properties depend strongly on the matrix. Nevertheless, it can be said, that PtTFPP is more stable and shows less photo-oxidation because of the high number of fluor atoms that are part of the complex. Furthermore, PtTFPP-films are usually more sensitive and therefore assumed as suited better for the measurement of the oxygen consumption rate of mammalian cells. [113]

4.1.5 Matrix

The sensing dyes, as summarised in previous section, have to be embedded in a matrix. This matrix has to fulfil the following requirements:

- permeable for gases,
- high diffusion coefficients for oxygen,
- high transparencies for the excitation light as well as for the emitted light,
- good solubility of the sensing dye without leakage,
- stability regarding the exposure to light and possible singlet oxygen as well as to high temperatures during the fabrication process,
- hydrophobic surfaces to avoid the uptake of water and ions.

In general, suitable matrices are polymers and silica gels which might be applied directly as bulk material or as nanoparticles that are dissolved in the liquid or embedded in another matrix.

Polymers

There are a few polymers, that fulfil the mentioned criteria, out of which silicon rubber and polystyrene (PS) are the most common ones. Silicon rubbers have an excellent oxygen permeability but are either difficult to fabricate inside a microfluidic device or only stable at temperatures below 200 °C (e.g. PDMS).

Sensing films out of PS are fabricated by dissolving the dye and polystyrene in an organic solvent and the subsequent evaporation of the solvent. PS is more stable than other polymers regarding the photo-oxidation, but this degradation still occurs and consumes oxygen [31]. The photo-oxidation might be suppressed by adding a stabiliser like 1,4-Diazabicyclo[2.2.2]octane (DABCO). However, DABCO evaporates at 174 °C and is thus not compatible with standard clean room fabrication processes. In general, polystyrene films are often used in microfluidic chips because of its easy fabrication and stability [30].

Silica gels

Silica gel is a porous material that is formed by a sol-gel process out of the precursor TEOS or TMOS. In contrast to silica aerogels as bulk material, as described in detail in sec. 3.3.3, the gels are used here as a thin film in which the dye is embedded. The film has to adhere on the substrate while cracks or other failures because of shrinkage do not matter. Therefore, the process of fabricating bulk silica aerogels is simplified as ageing, extensive exchange of medium and special drying processes are not needed. Hence, the gel is considered as xerogel. [38, 51]

Silica gels are chemically and thermally stable, and the photo-oxidation is eliminated as silicon oxide cannot be oxidised. However, the gel is also hydrophilic meaning that water interferes with the dye, which makes measurements of dissolved oxygen impossible. Therefore, pure silica gels can only be used for gas measurements. [113]

This disadvantage can be overcome by adding a hydrophobic, organically modified precursor, such as octyl-triethoxysilane (octyl-triEOS). The octyl-group remains on the silicon atom while the three ethoxy-groups are replaced by oxygen forming the SiO₂-network. The additives avoid the uptake of ionic species and the gel remains permeable to gases. [113]

4.2 Concept

In this section, the concept is presented how to analyse respiration of living cells. At first, the requirements for such a measurement are discussed in sec. 4.2.1. Subsequently, a suitable layout is derived from these specifications in sec. 4.2.2.

4.2.1 Requirements

The objective of the sensor is the determination of oxygen uptake of cells by measuring the decay of the oxygen concentration. This results in the following requirements:

- The microfluidic chamber has to be closed so that the change of oxygen concentration is only due to the consumption of the cells and not due to the diffusion in or out of the system.
- The oxygen sensing film has to be integrated into the chamber and has to be in contact with the sample liquid.
- The sensing film must be stable to allow reproducible measurements up to several hours because the dissolved oxygen is consumed within several minutes to hours depending on the number of cells. The measurement range of the partial oxygen pressure is between 0 and 0.21 atm (i.e. equivalent to a concentration of 21 % in air or $9.1 \frac{\text{mg}}{\text{L}}$ of dissolved oxygen at 20 °C)
- All materials including the sensing film must be non-cytotoxic and thus not harm the cell growth or influence the respiration. Furthermore, the cells must be able to adhere on the channel.
- All materials except of the matrix of the sensing film must not be permeable for oxygen to enable reproducible conditions with known amount of oxygen inside the chamber prior to the measurement.
- The temperature of the chip must be controlled because the respiration depends on the temperature and because the sensing principle is temperature dependent. The relevant temperatures are between 20 °C and 40 °C.

4.2.2 Sensor layout

The requirements are fulfilled with a microfluidic chip as shown in fig. 4.2. Such a chip consists of a microfluidic chamber that is etched into silicon and closed with a top plate made out of glass. Therefore, the chamber is sealed and no oxygen can diffuse in or out of the sample liquid. Furthermore, both materials are known as non-cytotoxic. The chip also needs an inlet and an outlet for the cell suspension. Here, care has to be taken to eliminate a flow of the liquid during the measurement as well as diffusion of oxygen in or out of the chamber through the inlets. [16, 17]

The oxygen sensing film is also non-cytotoxic, but the cells do not adhere on it. Therefore, the film is patterned on the top plate while the cells sink (and possibly adhere) on the bottom of the chamber. The film itself consists of a suitable matrix (Polystyrene or silica gel) and PtTFPP as sensing dye because it is commercially available, sufficiently stable and provides a good sensitivity. As the glass plate is transparent, the excitation light source and the read-out detector are placed above the chip. In case of PtTFPP, the excitation wavelength is 395 nm and the emitted wavelength 650 nm.

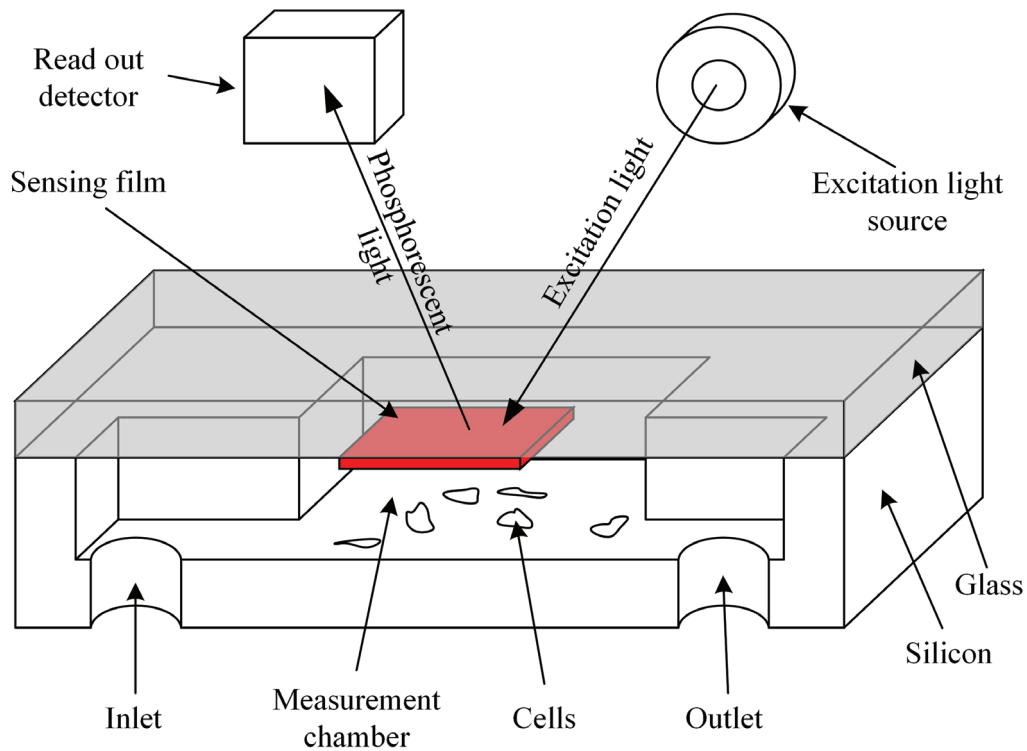


Figure 4.2: Principle of a microfluidic chip to measure the oxygen consumption rate of living cells with phosphorescent film.

Electrical heating and sensing elements, that are not shown in fig. 4.2 are placed on the outside of the silicon chip underneath the chamber. As silicon is a good thermal conductor and as distance between the heater and the chamber is small, the temperature of the chamber can be assumed as identical to the back side, where the sensor and the heater are placed.

Two different read-out methods are implemented: The read-out of the intensity with a Raspberry Pi camera as detector and of the phase shift with a photo diode. With the latter method, the lifetime of the dye is determined indirectly by measuring the phase between the phosphorescent signal and the excitation signal.

4.3 Implementation

In this section, the implementation of the presented concept is described, which includes the design of the chip regarding its microfluidic components (sec. 4.3.1) and its electric components (sec. 4.3.2) for the temperature control. Subsequently, the fabrication of the sensing film (sec. 4.3.3) and of the chip itself with clean room technologies is discussed in sec. 4.3.4. The temperature control and the read-out systems including their electrical circuits are presented in sec. 4.3.5. Finally, the

assembly and the holder structure, that contains the optical components and the chip, are described in sec. 4.3.6.

4.3.1 Chip design

The concept is realised with a microfluidic chip as shown in fig. 4.3. The chip contains a microfluidic chamber that is 2.5 mm wide and 12.3 mm long. The chamber is much longer than wide in order to achieve uniform filling. Furthermore, the chamber is U-shaped to keep it compact for an equal illumination and easy read-out with a camera. The chip contains in total five sensing areas that are circular and have a diameter of 1.25 mm. The channels are 200 μm deep, so that the entire measurement chamber has a volume of 6.2 μL . The outer dimensions of the chip are 9.5 by 11.5 by 1 mm^3 .

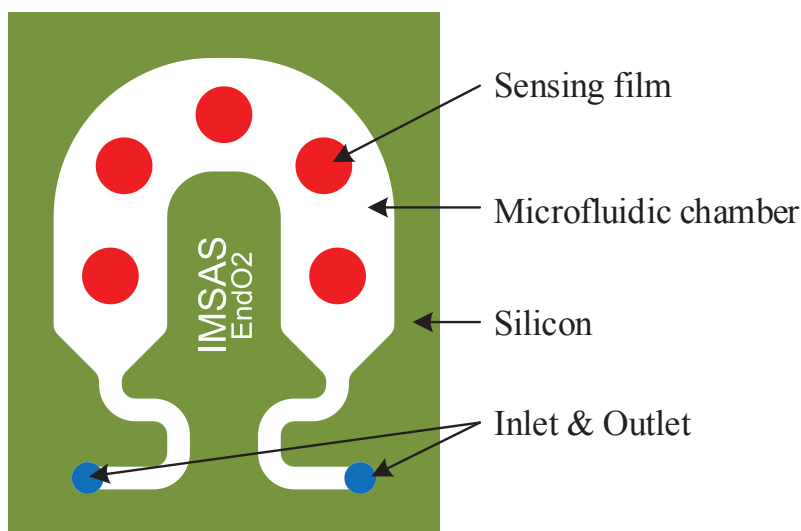


Figure 4.3: Design of the microfluidic chip (green) containing the measurement chamber (white), inlets (blue) and the sensing film (red).

The chamber has to be closed regarding the inlets and outlets. Otherwise, the liquid might either flow in or out of the chamber or oxygen diffuses from e.g. small air bubbles in the assembly into the chamber. Because the implementation of valves at the inlet and outlet is very complex, the microfluidic tubes have to be closed during the measurements to eliminate the flow. The diffusion is minimised by channels between the inlets and the chamber that are 5.8 mm long and only 0.5 mm wide. The inlets themselves are etched through the silicon and have a diameter of 0.7 mm.

4.3.2 Heating element

In order to set and control the temperature of the chip, heating and sensing elements are fabricated on the outer side¹ of the silicon layer. Both elements are made out of platinum because of its high stability and good sensing properties. The sensing elements consist of a layer of silicon oxide (100 nm) as electrical isolation, titanium (5 nm) as adhesion promoter and the platinum layer (100 nm). The sensor is based on the change of resistance, that is proportional to the temperature change. High sensitivity and low self-heating of the sensor is achieved by high resistance (here: 1000 Ω). In contrast, the heater benefits of a low electrical resistance in order to keep the voltage low. All design parameters are given in tab. 4.1.

Table 4.1: Design of the heating and sensing element, where R_{Pt} and R_{Ti} are the resistance of the platinum and titanium layer and R_{total} is the total resistance.

	Sensor	Heater
length	28.3 mm	31.4 mm
width	29.6 μm	490 μm
R_{Pt}	1014 Ω	68.6 Ω
R_{Ti}	76.5 k Ω	5.2 k Ω
R_{total}	1000 Ω	67.7 Ω

The sensor and the heater are patterned on the back side of the chip in a meander shape under the sensing elements. An overview of the design is given in fig. 4.4. The final chip is clamped in a 3D-printed holder (see also sec. 4.3.6). In contrast to silicon and water, the holder underneath the chip and the cover plate out of glass are only slightly thermally conductive. Therefore, the temperature of the silicon layer can be assumed as equally distributed.

4.3.3 Sensing film

As mentioned in sec. 4.2.2, a suitable dye for the application is PtTFPP. Here, this dye is embedded in a polystyrene matrix ("PS-film") as well as in a silica gel matrix ("SG-film") as described below. [17]

¹The inner side contains the channels and points towards the sensing elements.

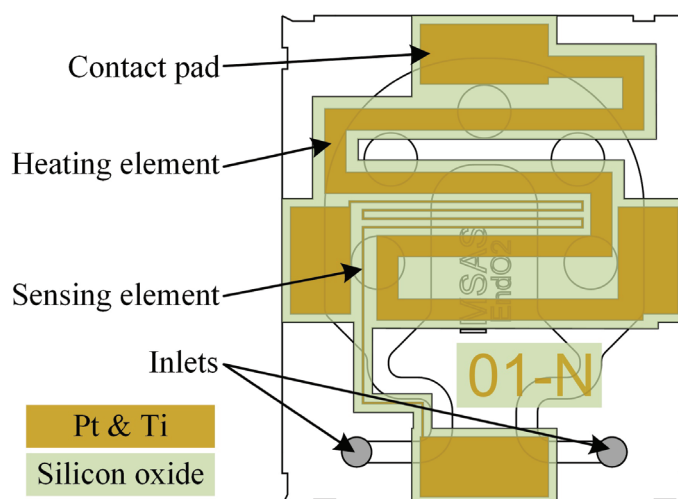


Figure 4.4: Design of the heating and sensing element on the back side of the silicon layer (the microfluidic channel on the front side is shown for orientation).

PS-film: PtTFPP in PS

The PS-film where PtTFPP is embedded in polystyrene consists of the following components:

- 10 mg PtTFPP,
- 500 mg polystyrene (PS),
- 10 mL toluol.

The solid compounds are dissolved in toluol and the solution is stirred for 15 min. Subsequently, the solution is pipetted onto the wafer and film is formed by the evaporation of the solvent. This process is accelerated by placing the wafer inside an exsiccator with vacuum.

SG-film: PtTFPP in silica gel

The SG-film consists of PtTFPP which is embedded in a silica gel. This gel is made by mixing:

- 4 mL tetraethylorthosilicate (TEOS),
- 0.2 mL octyltrimethoxysilane (OctyltriEOS),
- 1.25 mL ethanol,
- 0.4 mL 0.1 M hydrochlorid acid (HCl).

This solution is stirred for 1 h before it is mixed with a second solution consisting of 1 mL tetrahydrofuran (THF) and 2 mg PtTFPP. After another 10 min of stirring,

the solution is pipetted onto the wafer. The film solidifies by evaporation of the solvents. [24]

4.3.4 Fabrication

The chip is fabricated out of a 380 μm thick silicon wafer, that contains the channels, the heater and the temperature sensor, and a 500 μm thick borosilicate glass wafer with the sensing film. The entire process is summarised in fig. 4.5. At first, 10 μm photoresist AZ9260 of MicroChemicals is spin-coated on the silicon wafer, exposed for 120 s with a foil mask of Zitzmann GmbH and developed with AZ400K. This layer is used as a mask for the following DRIE-process to form the 200 μm deep channels in the silicon wafer. After the removal of the resist, the wafer is oxidised to form a 100 nm thick oxide layer, that is used later on as electrical isolation between the thermometer and the silicon. Then, the negative photoresist AZ nLoF 2070 of MicroChemicals is spin-coated on the unstructured side of the wafer, heated to 100 $^{\circ}\text{C}$ for 360 s, exposed for 18 s through a foil mask, baked again for 100 s at 110 $^{\circ}\text{C}$ and finally developed for 2 min with AZ726MIF of MicroChemicals. This process results in an undercut of the photoresist. Subsequently, 5 nm titanium and 100 nm platinum are sputtered on the wafer. The photoresist is removed with AZ-remover and consequently, the metal is patterned by lift-off. Another layer of 1.8 μm AZ1518 photoresist is patterned on the metal layer and used as a mask for the following wet-etching of the silicon oxide with Oxide Etch 7:1 of Honeywell Specialty Chemicals. After the removal of this layer, 1 μm aluminium is sputtered on the DRIE-etched side of the wafer and 10 μm AZ9260 resist is patterned on the platinum side of the wafer. Subsequently, the holes are etched into the wafer with a DRIE-process. Finally, the resist and the aluminium are removed by wet-etching. [16, 17]

The dry film resist i-HE of Harke Germany Services GmbH & Co. KG is laminated on the borosilicate wafer and patterned with a foil mask. This mask is used for the partial roughening of the glass by powder blasting. Consequently, the rms-roughness is increased to $R_q = 3.8 \mu\text{m}$. After removal of the resist and cleaning of the wafer, the dry film resist Etertec XP800-15 of Eternal Chemical Co., Ltd. is laminated on the wafer, exposed with the same mask as for the powder-blasting and developed for 1.5 min with $10 \frac{\text{g}}{\text{L}}$ K_2CO_3 . Then, the oxygen sensing film is applied as described in sec. 4.3.3. The resist is stripped with K_2CO_3 within 2 h, which also lifts off the sensing film. This patterning method is gentle enough not to harm the film, as no organic solvents, strong bases or acids are used.

Finally, both wafers are bonded anodically. The sensing dye is decomposed at high temperatures above 230 $^{\circ}\text{C}$ meaning that the phosphorescence is oppressed.

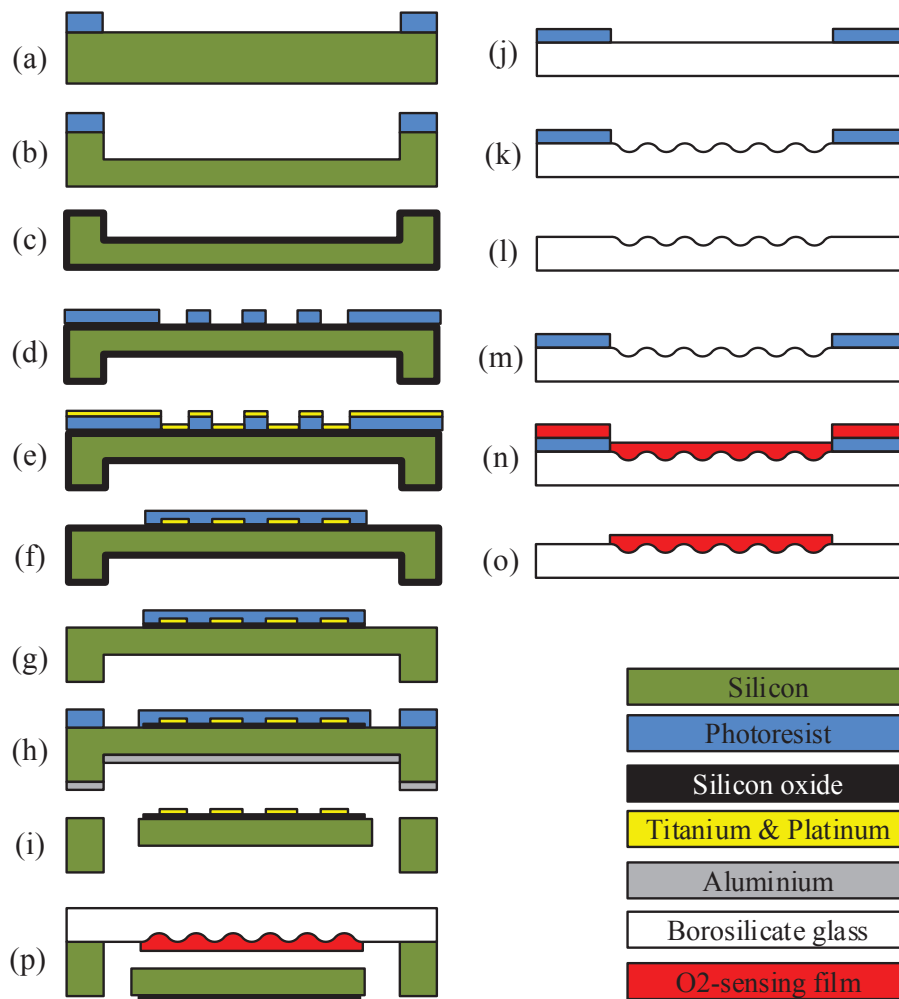


Figure 4.5: Fabrication of the oxygen sensing chip: (a) patterning of 10 μm photoresist AZ9260 on the silicon wafer (b) 200 μm DRIE-process (c) removal of the resist and thermal oxidation of the wafer (d) patterning of photoresist AZ nLoF 2070 (e) deposition of 5 nm titanium and 100 nm platinum (f) lift-off of the metal layers by removing the resist and subsequently patterning of 1.8 μm photoresist AZ1518 (g) wet-etching of SiO_2 (h) patterning of 10 μm AZ9260 and deposition of aluminium on the back side (i) DRIE-process, removal of the resist and of the aluminium (j) patterning of i-HE dry film resist on a borosilicate glass wafer (k) roughening of the glass surface by powder blasting (l) removal of the resist (m) patterning of Etertec XP 800-15 (n) deposition of the oxygen sensing film (o) lift-off process of the film by removing the resist and (p) anodic bonding of both wafers.

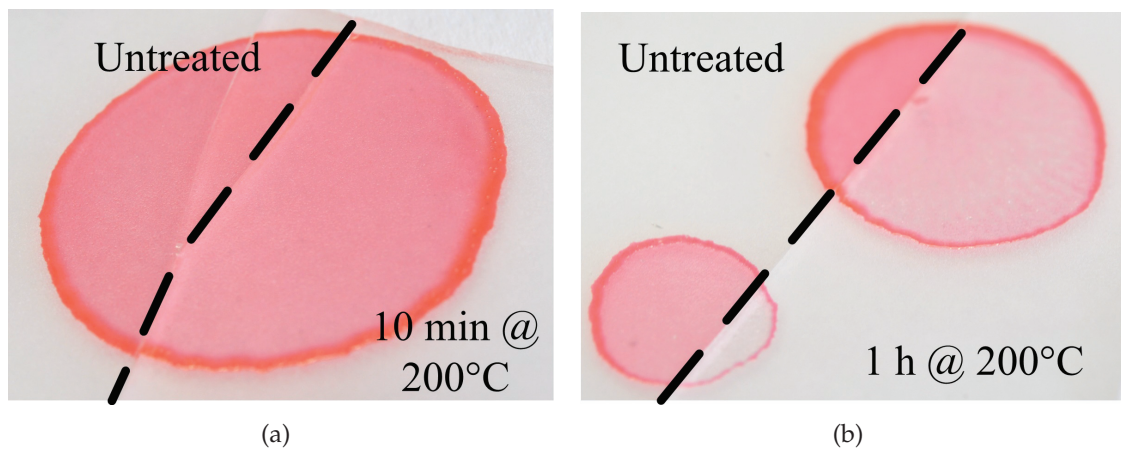


Figure 4.6: Comparison of the PS-PtTFPP-film before and after thermal treatment: (a) 10 min at 200 °C in vacuum (b) 1 h at 200 °C in vacuum.

The bonding at lower temperatures (here 200 °C) reduces the mobility of the ions and results in low bonding strength. This effect is compensated partly by increasing the voltage to 1100 V. Furthermore, the film is also damaged the longer it is exposed to high temperatures. Fig. 4.6 compares the PS-film before and after a thermal treatment similar to the bonding process, except of the missing electric field. Although this temper process is carried out in vacuum, the film shows much more bleaching after 1 h at 200 °C compared to just 10 min for which the colour of the film is almost identical to the film before the tempering step. As a consequence, the anodic bonding of the wafer is executed for only 10 min. The final chip is shown in fig. 4.7.

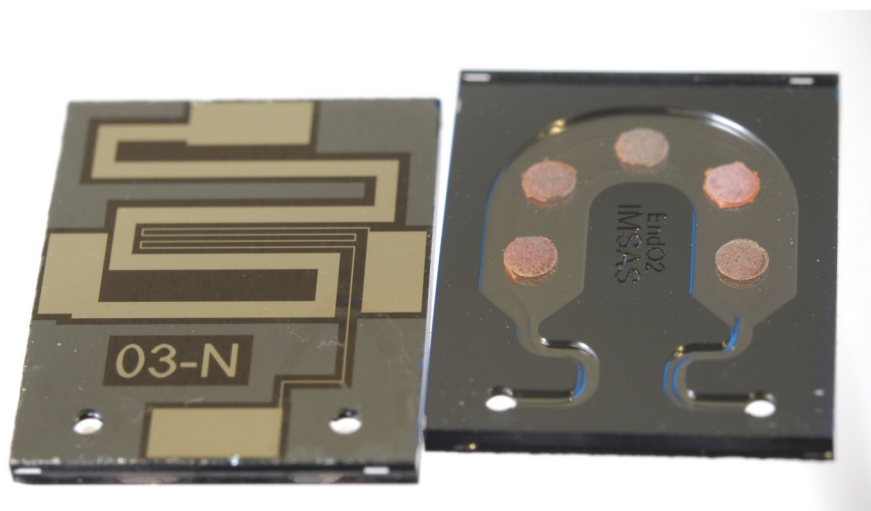


Figure 4.7: Images of the back side and front side of the final chip with a silica gel film. The outer dimensions are $9.5 \times 11.5 \times 1 \text{ mm}^3$ [17]_{©2017 IEEE}

4.3.5 Temperature control and electrical read-out system

Two different read-out systems are implemented - the read-out of the intensity and of the phase shift. Furthermore, the setup contains a electrical network for the temperature control.

Read-out of the intensity

The read-out system of the intensity, as summarised in fig. 4.8, is based mainly on the Raspberry Pi and the Raspberry Pi Camera V2 because it allows the easy control of image acquisition and of electronic components. The optical system contains the camera, a high-power LED with the wavelength of 395 nm, the chip and an optical long-pass filter with the cut-off wavelength of 600 nm so that only the phosphorescent light is recorded by the camera. Although a high-power LED is used, the shutter speed of the camera has to be around 300 ms because of the weak intensity of the emitted light by the thin optical film.

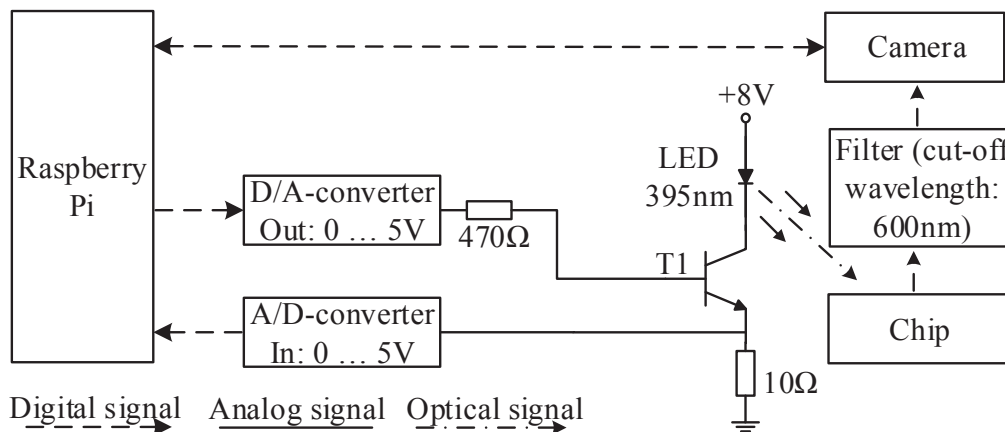


Figure 4.8: Electrical system for the intensity measurement containing the controlled drive of the LED and the optical system with a camera for which all digital components are controlled by a Raspberry Pi.

The electrical power of the LED in the experiments is around 300 mW, which is too high to be controlled directly by the Raspberry Pi. Therefore, the digital signal of the Raspberry Pi is converted with a 10 bit D/A-converter to a low-power analog signal, which is amplified with a npn-bipolar transistor. Obviously, the intensity of the phosphorescent light depends strongly on the intensity of the LED being proportional to the electrical current. Consequently, this current has to be set precisely in order to achieve reproducible results. As the amplification of the transistor varies significantly with temperature and voltage, a feedback system is required. Here, the current is determined by measuring the voltage over a high-

power $10\ \Omega$ resistance with an 12 bit A/D-converter. The resolution of the read-out system is 0.1 mA.

Read-out of the phase shift

The electronic circuit for the read-out of the phase shift consists of three parts: the amplifier network to drive the LED, the read-out circuits and the external devices, as shown in fig. 4.9. These devices are the waveform-generator for the low-power input signal that is sine-wave in the kHz range with an offset and the oscilloscope for the actual read-out. The input signal is amplified with an npn-transistor similar to the read-out circuit of the intensity. The high-power electrical signal (up to 1 W peak power) is transformed into excitation light with an high-power LED with the wavelength of 395 nm. The phosphorescent light of the film is filtered with an optical long-pass filter with the cut-off wavelength of 620 nm and recorded with a photodiode (OPT101 from Texas Instruments) that has an integrated transimpedance amplifier.

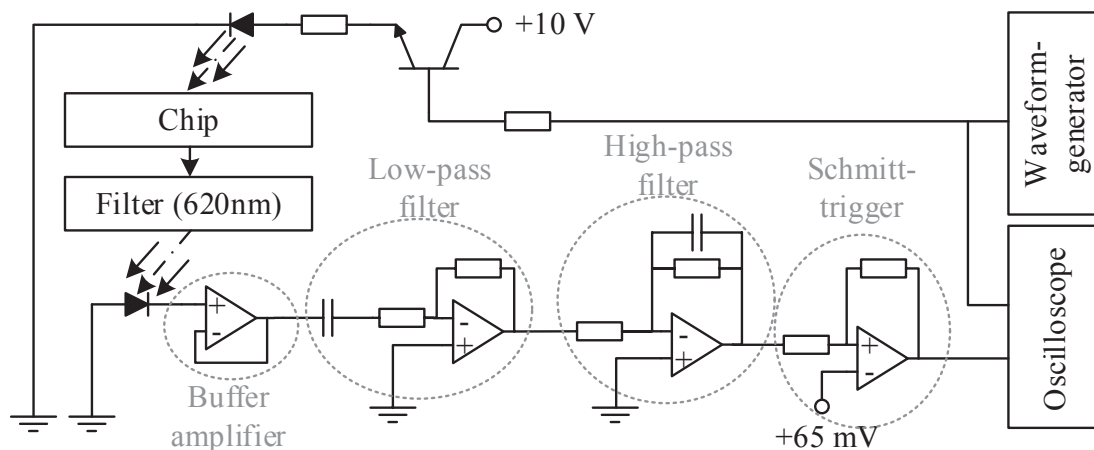


Figure 4.9: Electrical system for the read-out of the phase shift.

The signal of the photodiode is decoupled from the following circuit with a buffer amplifier. Subsequently, the signal is amplified and filtered with an active low-pass filter (cut-off frequency 20 kHz) and active high-pass filter (1 kHz) with the amplification of 20 each. For a better read-out, the signal is transformed into a binary signal with a Schmitt-trigger before the phase between this signal and the original input signal of the waveform-generator is determined in the oscilloscope.

The main signals are shown in fig. 4.10. The voltage of the photodiode has a low amplitude of about 2 mV with an offset of 4 mV and with a phase shift regarding the excitation LED. This phase shift φ is originated by the phase of the luminescent film and also by the integrated amplifier. The signal is amplified, filtered and

finally transferred to a binary signal with a Schmitt-trigger. This process results in a clear signal, that is either approximately -0.05 V or 4.5 V , but also alters the phase regarding the excitation signal. The phase, that is analysed later in sec. 4.4.2.5, is defined between the zero-crossing of the signal of the Schmitt-trigger and the crossing of the excitation signal with its offset at the falling slope (see fig. 4.10).

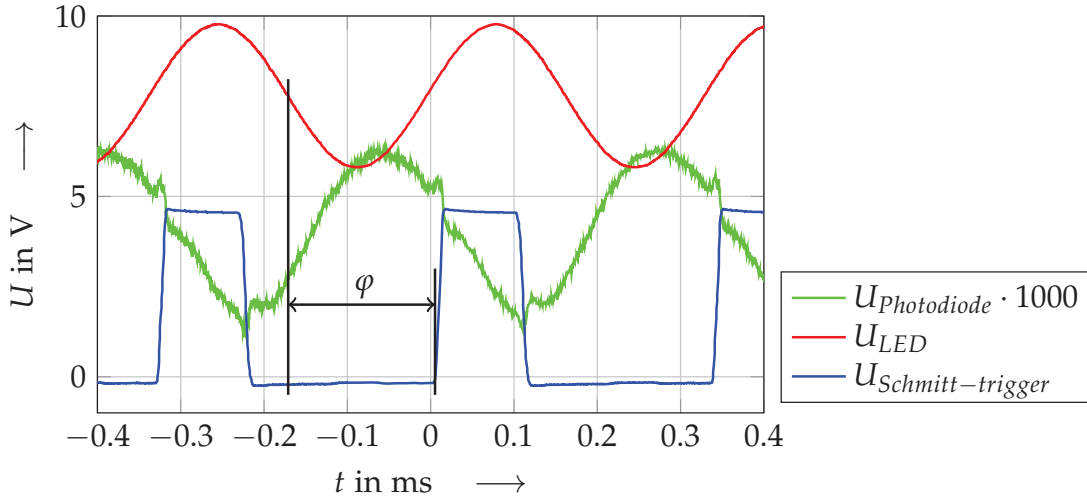


Figure 4.10: Electrical signals of the excitation LED U_{LED} , of the photodiode $U_{Photodiode}$ and of the Schmitt-trigger $U_{Schmitt-trigger}$ and the resulting phase shift φ .

Temperature control

The temperature control consists mainly of 3 components, as summarised in fig. 4.11: The Raspberry Pi which processes the data and where the PI-controller is implemented, the read-out circuit for the temperature and the control circuit for the heater. The platinum resistances of the chip for the temperature measurement is part of a Wheatstone bridge which transforms the resistance change into a voltage. Due to fabrication tolerances, the platinum resistances vary between the chips, but the conductivity and its thermal coefficient α_{Pt} can be assumed as identical. Therefore, the Wheatstone bridge contains a potentiometer to set the bridge voltage to 0 V at room temperature T_0 . So, the bridge voltage U_{bridge} is found as

$$U_{bridge} = \frac{5\text{ V}}{4} \frac{\Delta R_s}{R_s} = \frac{5\text{ V}}{4} \alpha_{Pt} \Delta T, \quad (4.3)$$

where R_s is the resistance of the temperature sensor, ΔR_s is its change and ΔT is the temperature change regarding the room temperature T_0 . In the relevant temperature range, the resistance varies by approximately 10%, which results in a

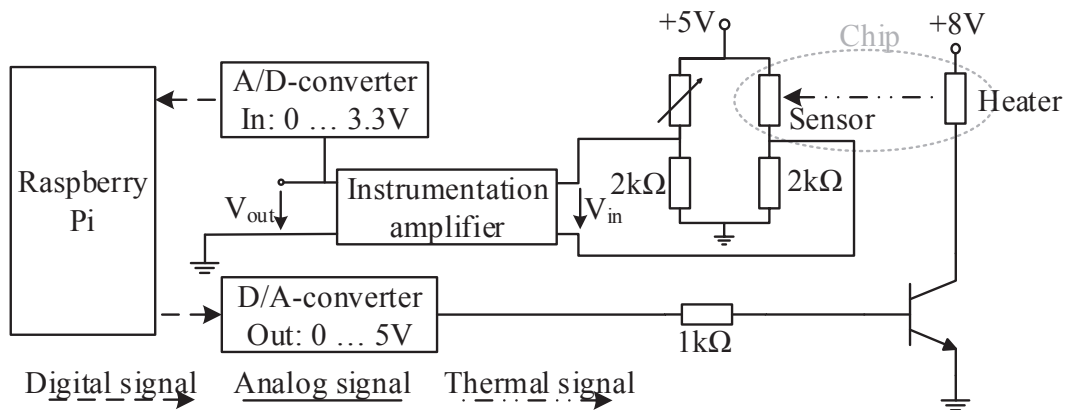


Figure 4.11: Electrical system for the read-out of the temperature with the on-chip resistance and the amplification circuit for the heater current. All components are controlled by a Raspberry Pi.

maximal change of the output voltage of 125 mV. This voltage is amplified with an instrumentation amplifier and converted into a digital signal that is transmitted to the Raspberry Pi.

The digital heating signal of the Raspberry Pi is converted into a voltage with a D/A-converter. The resulting low-power output current is amplified with an npn-bipolar transistor, in which the collector current flows through the heater resistance on the chip. The amplification of the transistor is not constant and might change with temperature and voltage. However, its alternations are relatively slow and is thus levelled out with the PI-controller.

4.3.6 Assembly

Each read-out method requires an individual assembly - either with a camera for the read-out of the intensity or with a photodiode to determine the phase shift. Both assemblies are discussed below, as well as the chip holder that is identical for both assemblies. All holders are fabricated by 3D-printing, which is an attractive technology to fabricate individual connectors and holders with reasonable efforts and costs. [17, 105]

Design of the chip holder

The chip is clamped between two 3D-printed holders. The lower part, as shown in fig. 4.12, contains the two fluidic inlets and the four electric contacts. The fluidic connection from the holder to the macroscopic world is realised by conical inlets in which thin tubes can be inserted and glued. The connection towards the chip is sealed with O-rings of EPDM rubber, purchased from Parker Hannifin GmbH.

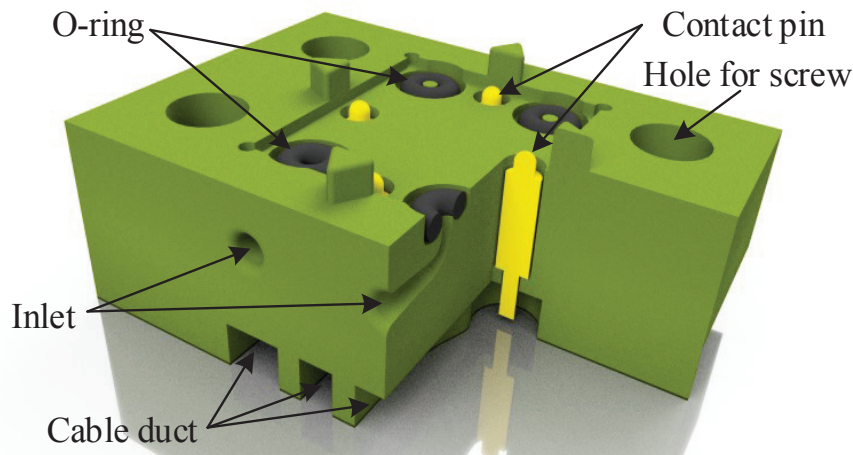


Figure 4.12: CAD-based image of the lower holder structure (green) with the four O-rings (black) and the four contact pins (yellow).

Although the chip has only two fluidic inlets, four O-rings are used for symmetrical clamping.

The electrical contacts are realised with four contact pins that are inserted into the holder. These pins are equipped with springs so that the top of the pin is pressed against the chip but damage of the chip by high mechanical load is avoided. A cable is soldered onto the lower end of each pin and is guided out of the holder through a cable duct. As a consequence of the soldering, the pin is fixed onto the holder.

The upper part of the holder is used to press the chip onto the fluidic and electric connectors. Both parts are fabricated out of HTM140 with the Perfactory Micro HiRes printer from Envisiontec GmbH. To avoid cytotoxic effects of the resin, the lower part with the fluidic inlets is coated with 10 μm Parylene C (compare sec. 3.4.4). The entire dimension of both parts is 23.7 mm by 16.7 mm by 11.6 mm.

Assembly for the read-out of the intensity

The assembly for the read-out of the intensity contains two further holders: one for the LEDs and another one for the Raspberry Pi Camera and the optical filter, as shown in fig. 4.13. The LED-holder enables the fixation of three LEDs: one excitation LED in the middle and if needed two illumination LEDs on the side. All LEDs are inclined by 45° relative to the surface of the chip while the camera is mounted perpendicular to the chip. The entire assembly is 69 mm by 50 mm by 69 mm

Assembly for the read-out of the phase shift

The read-out of the phase shift is realised with a photodiode (see fig. 4.14). Similar to the assembly of the intensity read-out, the photodiode is arranged onto an optical filter that transmits only red light. Both parts are clamped with a cap onto the

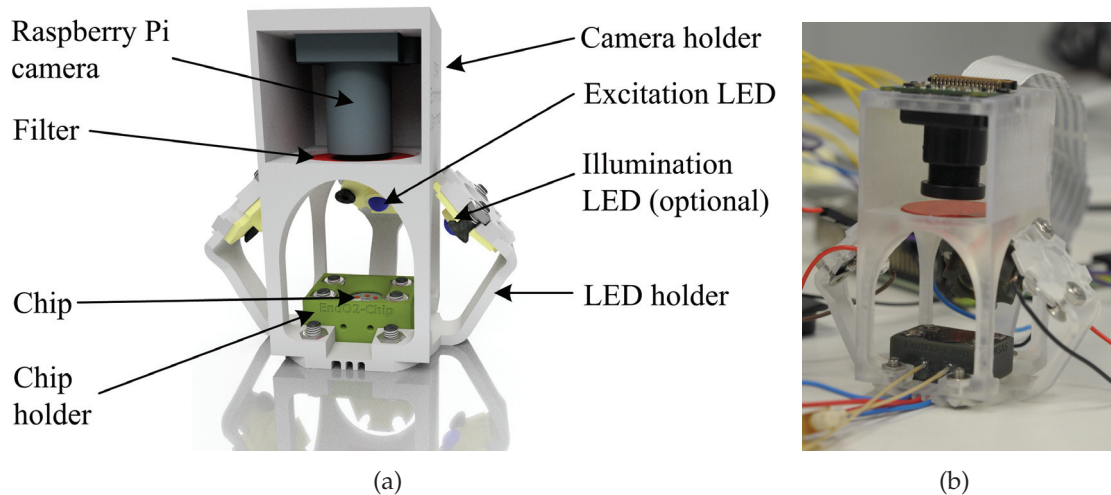


Figure 4.13: Assembly for the read-out of the intensity: (a) CAD rendered image where the cables and tubes are not shown (b) photo.

photodiode holder so that no ambient light (or excitation light) interferes with the measurement.

The position of the photodiode holder and of the LED holder are both adjustable to enable the optimal position of both elements. Furthermore, the distance between the chip and the photodiode is kept as short as possible (here 10 mm) to ensure maximal intensity of the phosphorescent light.

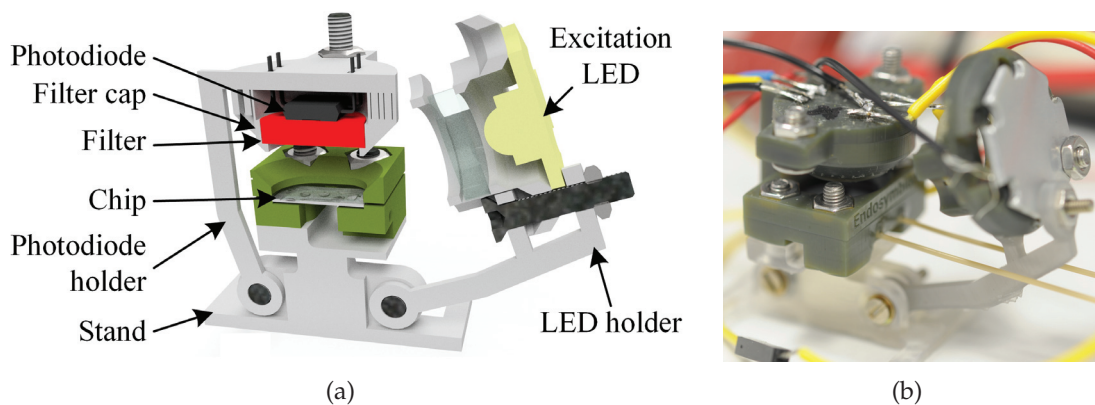


Figure 4.14: Assembly for the read-out of the phase shift: (a) CAD rendered cross-section where the cables and tubes are not shown (b) photo.

4.4 Results

The results of the fabricated devices are presented in this section. At first, the electrical heater and the temperature control are characterised in sec. 4.4.1. Subsequently, both films are characterised as well as both read-out methods (sec. 4.4.2). Finally,

mammalian cells are placed in the chip and their oxygen consumption is determined in sec. 4.4.3.

4.4.1 Characterisation of the temperature control

To evaluate the temperature sensor, the chip is mounted in the holder and placed in an oven. The oven is set at different temperatures and the resistance of the heater is measured with a multimeter. As a result, the resistances increases linearly with increasing temperature as shown in fig. 4.15(a). Based on these results, the temperature T can be determined (coefficient of determination $R^2 = 0.9989$) as

$$T = 452 \text{ K} \frac{R_s}{R_{s0}} + T_0, \quad (4.4)$$

where R_s is the measured resistance, R_{s0} the resistance at the temperature T_0 (here $R_{s0} = 1622 \Omega$ and $T_0 = 25^\circ\text{C}$). However, the resistance of the fabricated temperature sensor is much higher than initially designed (around 1600Ω compared to 1000Ω). This difference is due to the lower conductivity of thin films compared to the bulk material. Here, the conductivity of 110 nm sputtered platinum is only $6.1 \times 10^6 \frac{1}{\Omega \text{ m}}$ compared $9.5 \times 10^6 \frac{1}{\Omega \text{ m}}$ of bulk material. Nevertheless, this difference does not hamper the operability of the temperature sensor.

The circuit as described in sec. 4.3.5 transforms the change of resistance into output voltage U_{out} , that is measured with a 12 bit A/D-converter. The correlation

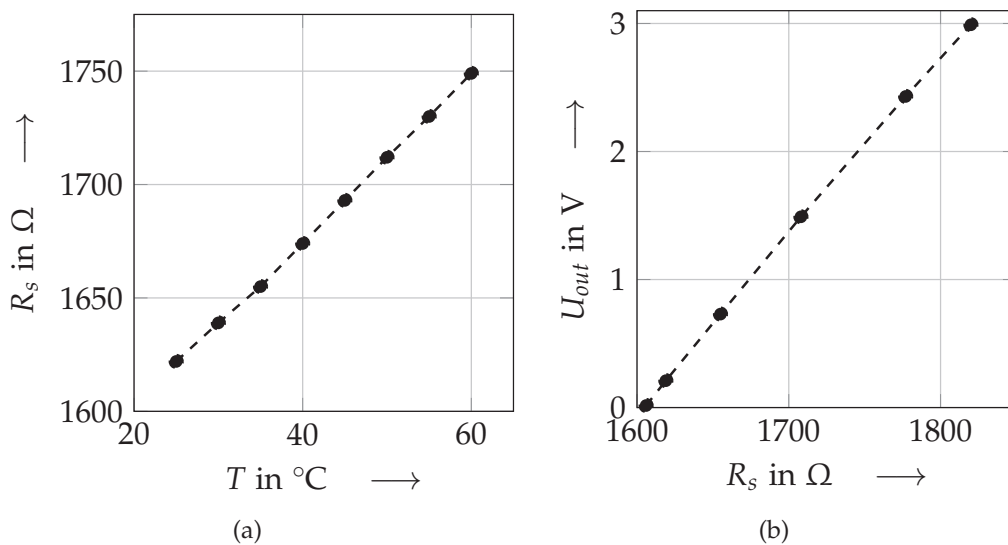


Figure 4.15: (a) Measured steady-state resistance R_s at different temperatures T (b) output voltage U_{out} of the circuit for different resistances R_s of the temperature sensor.

between the resistance R_s and this voltage is shown in fig. 4.15(b). Here, the output voltage increases linearly (coefficient of determination $R^2 = 0.9992$) with the resistance so that the relative change of resistances ($\frac{\Delta R_s}{R_{s0}}$) can be found as

$$\frac{\Delta R_s}{R_{s0}} = 0.044 \frac{1}{V} U_{out}. \quad (4.5)$$

The final temperature is determined with eq. 4.4 as

$$T = 19.9 \frac{K}{V} U_{out} + T_0. \quad (4.6)$$

As a consequence, the measurement range is 65 K starting at T_0 and the resolution 0.02 K. However, the accuracy of the temperature sensor and the read-out system is lower and mainly limited by calibration accuracy (i.e. adjusting the potentiometer at a known temperature).

Fig. 4.16 shows the step response of the system. Here, the heater is supplied with a current of 50 mA for 450 s before the current is turned of. When the heater is switched on, the temperature increases towards 45 °C. Basically, the thermal system of the chip is a PT1-element but the surrounding holder structures represent a second, much slower PT1-element. Therefore, the temperature increases relatively fast after switching the heater on, but converges much slower towards steady-state temperature. So, it takes about 250 s to reach 90 % of the final temperature during heating and 170 s during cooling. The measured temperature shows some high frequency noise that is likely due to the power supply of the Raspberry Pi. However, this frequency is much higher than the cut-off frequency of the thermal system and has thus no influence of the performance of the system. With a constant current of 100 mA, the chip is heated up to 72 °C within 2 min.

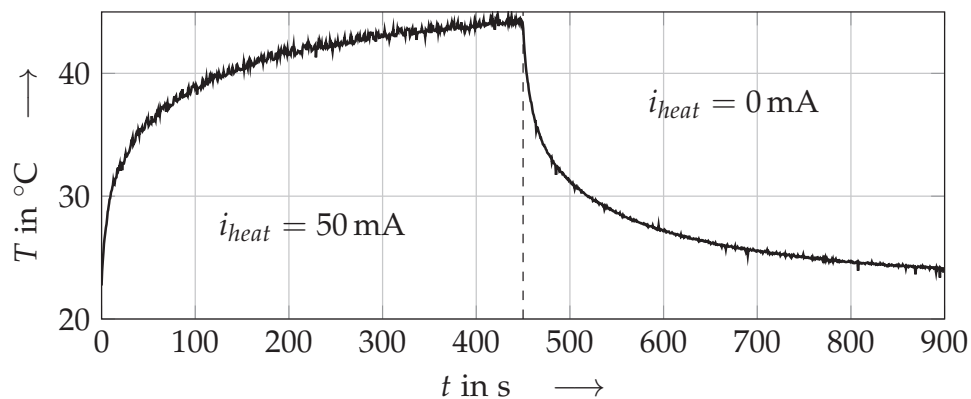


Figure 4.16: Step response of the heater in its holder for $i = 50$ mA (for $t \leq 450$ s) and $i = 0$ mA (for $t > 450$ s) at a room temperature of 22.7 °C.

In order to control the temperature, a discrete PI-control is implemented in the Raspberry Pi. The heating current is set with a sampling rate of 100 Hz that is several orders fast than the system itself. The heating current is limited by the electrical circuit to maximal 100 mA and minimal 0 mA. Active cooling is not possible. Therefore, an anti-wind-up element is added to the PI control that limits the integral part to the physical limitations. Fig. 4.17(a) shows the resulting system behaviour for three different PI-configurations. The corresponding heating currents are given in fig. 4.17(b). The presented scenario contains three step responses for an increasing and decreasing reference temperature T_{ref} and an external disturbance, for which water with room temperature is flushed through the system with high flow rates up to $100 \frac{\mu\text{L}}{\text{s}}$.

In comparison, the setting with $K_p = 10$ and $K_I = 1.5$ shows the fastest response (8.7 s for heating and 18 s for cooling to reach 90% of T_{ref}) and the lowest overshoot (0.25 K for heating and 0.9 K for cooling). However, the overshoot after the disturbance is as high as 2.2 K, but this disturbance also represents a worst-case scenario because the refilling with new medium can be realised slower. The mentioned response time for cooling depends strongly on the temperature of the holder because the chip will not recover to room temperature unless the holder does so, too.

To sum it up, the PI-control results in a much faster response time compared to open-loop heating, small overshoot and very good stability, although the system is

- non-linear since the heating is proportional to the square of the current and the amplification of the electronics is non-constant,
- the system has a PT2-behaviour due to the two heat sinks (the chip and the holder),
- the temperature measurement has some noise,
- the cooling is based only on non-linear convection processes and can thus not be controlled actively.

4.4.2 Characterisation of the sensing film

The fabricated microfluidic chips contain either the SG-film, where the dye PtTFPP is embedded in silica gel or the PS-film, for which the same dye is embedded in a matrix out of Polystyrene. Both films are characterised with the setup of the intensity read-out (sec. 4.4.2.1 - 4.4.2.4). At first, the methods are explained in sec. 4.4.2.1. Subsequently, the intensity is analysed for different oxygen concentrations and for different temperatures. A disadvantage of this luminescent based sensing concept is the photo-oxidation, which consumes oxygen as a by-product of the quenching. This

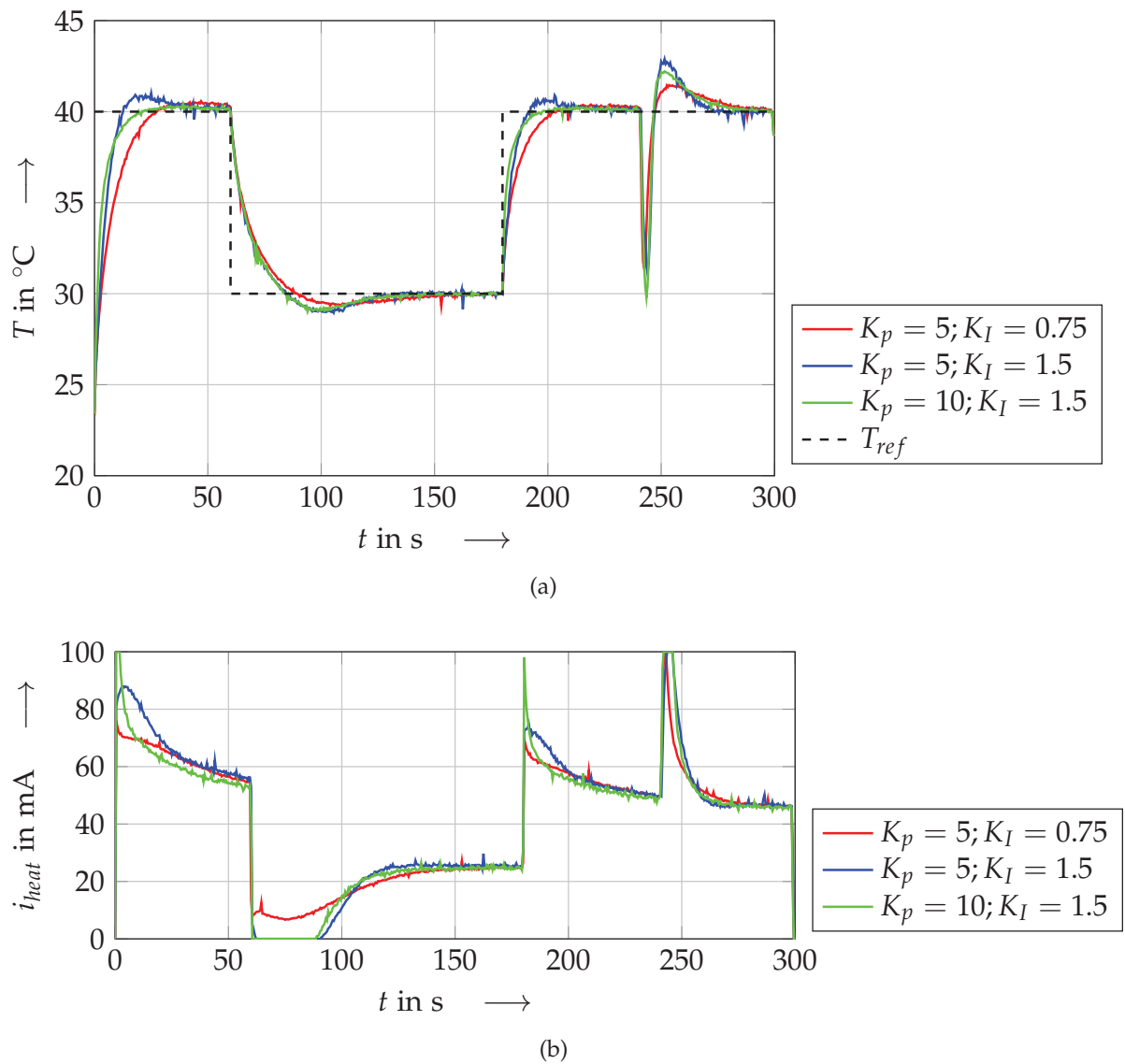


Figure 4.17: Controlled temperature (fig. (a)) and heating current (fig. (b)) of the device for different configurations of the PI-control. At $t = 240$ s, water with 22°C was flushed through the device for 2 s with a flow rate of approximately $100 \frac{\mu\text{L}}{\text{s}}$.

photo-oxidation is analysed in sec. 4.4.2.3. Finally, the response time of the PS-film is determined in sec. 4.4.2.4. The other read-out method is applied to characterise the phase shift of the PS-film in sec. 4.4.2.5. Finally, both read-out methods are compared in sec. 4.4.2.6. [17]

4.4.2.1 Methods

As explained in sec. 4.1.2, the phosphorescent film measures only the partial pressure of the gas in the pores, that correlates with the concentration of the dissolved oxygen. In the following experiments, the pressure inside the chamber during the measurements equals ambient pressure. Therefore, the oxygen concentration is expressed here as % (air), that describes the portion of the volume of oxygen in air and also the portion of the partial pressure of oxygen to the total air pressure.

Unless otherwise stated, the measurements are carried out at room temperature of approximately 23 °C. The oxygen concentration of the samples is measured with the commercial oxygen sensor FireStingO2 of PyroScience GmbH prior to the experiments.

The measurements are carried out with a current of 90 mA through the LED and a shutter speed of 300 ms for the polystyrene based film and 400 ms for the silica gel based film.

4.4.2.2 Intensity of the film

In order to determine the sensitivity and to characterised the film, the intensity of the device for different oxygen concentrations is determined at room temperature. Therefore, five images of the fluorescent film were recorded for each concentration to indicate the reproducibility and accuracy.

Fig. 4.18 shows the mean intensity of the same spot and oxygen concentration for the polystyrene based film and for the silica-based film. The standard deviation for the spots and concentration are very low (0.14 for the PS-film and 0.04 for the SG-film). The intensity varies for both chips between the spots so that each spot has to be calibrated individually. Furthermore, the PS-film has a higher intensity but also a higher relative change of intensity at the given range.

Ideally, the intensity-concentration curve fits the Stern-Volmer-equation:

$$\frac{I}{I_0} = \frac{1}{1 + K_{SV}c_{O_2}}, \quad (4.7)$$

where I_0 is the intensity without any oxygen. In reality, preparing a sample without any oxygen is very difficult so that I_0 cannot be measured directly. Therefore,

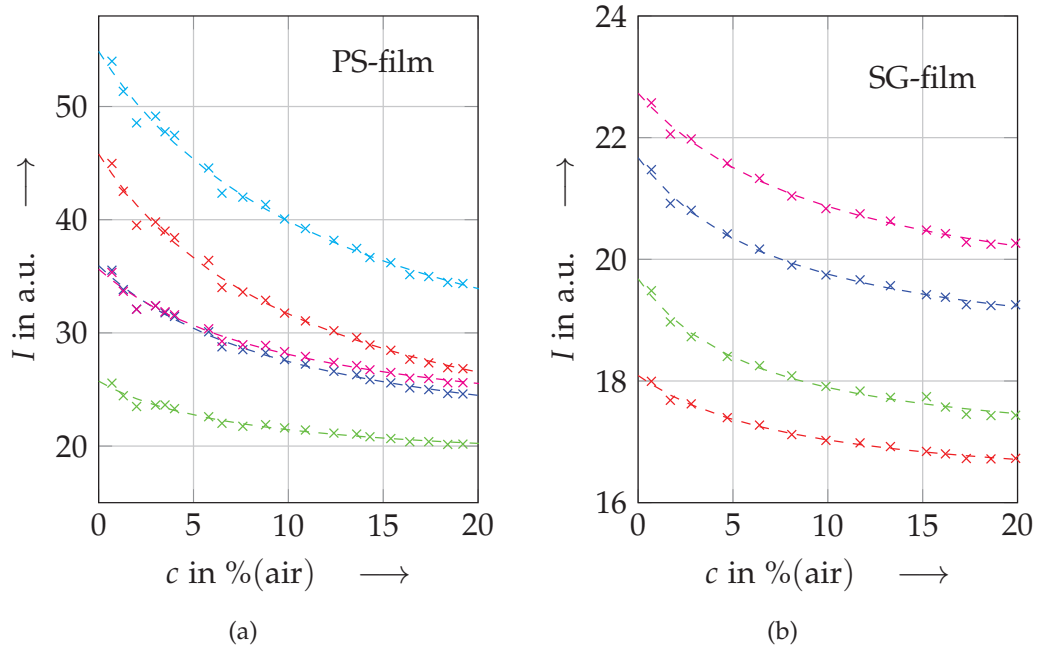


Figure 4.18: Measured intensities for different oxygen concentrations and different spots, and the fitted curves (dashed) at constant temperature. Each point is the mean value of 5 measurements: (a) polystyrene based film (b) silica gel based film.

I_0 and K_{SV} are both fitted by all measurement points by using non-linear least-square algorithms. As a result, mean fitting errors vary for different spots between 0.87%(air) and 1.77%(air) for the PS-film and 1.55%(air) and 1.92%(air) for the SG-film. This fitting error can be significantly reduced by using the two-site model as

$$\frac{I}{I_0} = \frac{\gamma_Q}{1 + K_{SV}c_{O_2}} + (1 - \gamma_Q), \quad (4.8)$$

where γ_Q describes the portion of the dye that is quenched by oxygen [113]. By determining the parameters, as summarised in tab. 4.2, the fitting error is reduced to 0.27%(air) and 0.58%(air) for the PS-film and 0.68%(air) to 1.52%(air) for the SG-film. The fitted curves are also shown in fig. 4.18.

In the two-site model, γ_Q is the portion of the dye that is quenched by oxygen and $(1 - \gamma_Q)$ is not quenched and thus not in contact with any oxygen. The latter portion is around 50% of the dye for the PS-film and around 88% for the SG-film. It means that this amount of dye is completely trapped in the matrix and not on the surface of the porous material.

In order to determine the temperature dependency of the sensor, water with a given oxygen concentration is filled into the chip and the temperature is altered

Table 4.2: Fitted parameters for both chips by using the two-site model (see eq. 4.8).

Parameter	Polystyrene based film	Silica gel based film
$\frac{I_0}{I_{20}}$	1.65 ... 1.30	1.076 ... 1.117
I_0	25.7 ... 54.9	18.1 ... 22.7
γ_Q	0.29 ... 0.66	0.11 ... 0.17
K_{SV}	0.076 ... 0.13 l/%(air)	0.09 ... 0.16 l/%(air)
Fitting error	0.27 ... 0.59 %(air)	0.68 ... 1.52 %(air)

with the integrated heater in steps of 3 K. For each temperature and concentration, five images are taken and the intensity is analysed. While the sample is heated up, the absolute amount of oxygen remains constant, but the partial pressure changes because the solubility is temperature dependent.

Fig. 4.19 shows the mean intensity for four different temperatures and oxygen concentrations at one exemplary spot. The mean standard deviation for each marked point is 0.026 (PS-film) and 0.017 (Si-Film).

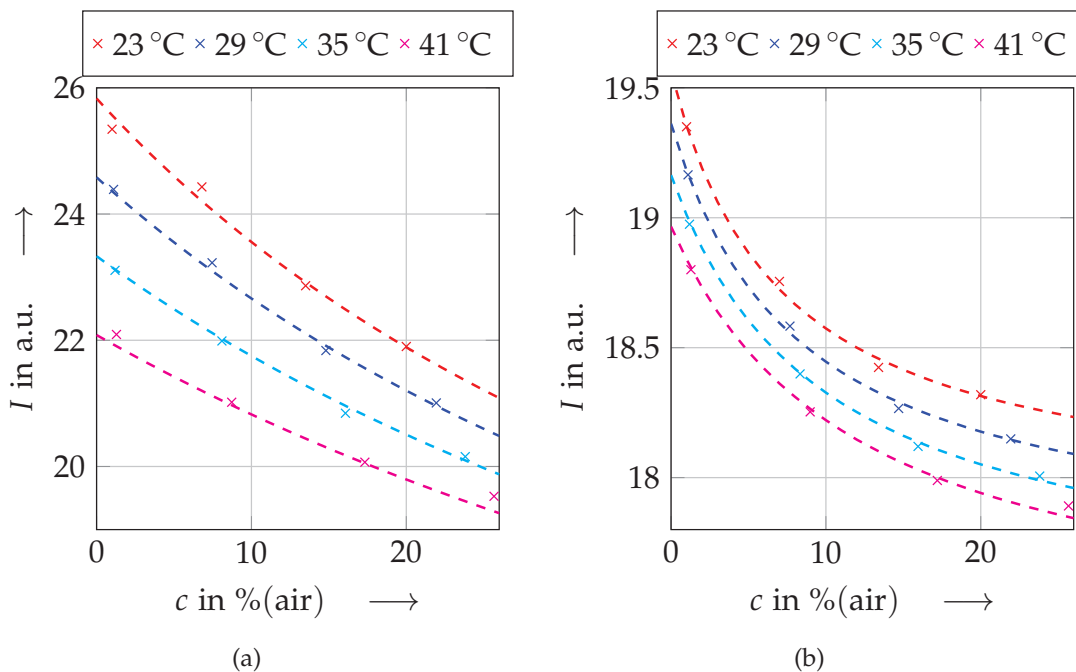


Figure 4.19: Measured intensity at one exemplary spot for different temperatures and different oxygen concentrations and the fitted curves (dashed) of the temperature extended two-site model. Each point is the mean value of 5 measurements: (a) Polystyrene based film (b) Silica gel based film.

The two-site model can be extended to model also the temperature dependency to

$$I(c, T) = I_{0,0}(1 + \alpha_{I_0}\Delta T) \left(\frac{\gamma_Q}{1 + K_{SV,0}(1 + \alpha_{K_{SV}}\Delta T)c_{O_2}} + (1 - \gamma_Q) \right), \quad (4.9)$$

where α_{I_0} describes the change of $I_{0,0}$ and $\alpha_{K_{SV}}$ the change of $K_{SV,0}$ depending on the temperature. This model assumes that the intensity I_0 and the Stern-Volmer-coefficient K_{SV} depend linearly on the temperature while γ_Q remains constant. By using all 140 measured intensities², the five parameters $I_{0,0}$, α_{I_0} , γ_Q , $K_{SV,0}$ and $\alpha_{K_{SV}}$ are fitted by using non-linear fitting algorithm and the fitted curves are also plotted in fig. 4.19. Both thermal coefficients are negative and differ between the spots. In case of the exemplary spots, $I_{0,0}$ decreases by $-0.0071/\text{K}$ (PS-film) and $-0.00161/\text{K}$ (SG-film) and $K_{SV,0}$ with $-0.0151/\text{K}$ (PS-film) and $-0.011/\text{K}$. By using the proposed model and the fitted parameters, the fitting error for the oxygen concentration is 0.84 %(air) (PS-film) and 0.95 %(air) (SG-film).

4.4.2.3 Photo-oxidation of the film

The photo-oxidation, and thus the stability of the film, is determined by filling the chamber with water with an oxygen concentration of 20 %(air). During the experiment, the temperature is kept constant at 25 °C. The determined concentration over time is shown in fig. 4.20. In case of the polystyrene based film, the oxygen concentration decreases by 0.61 ± 0.04 %(air)/h. In contrast, the silica gel based film is much more stable, as the oxygen consumption is only 0.017 ± 0.004 %(air).

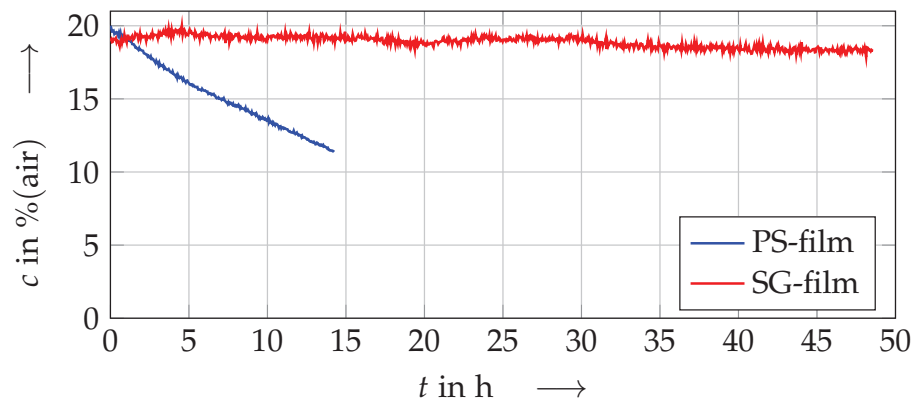


Figure 4.20: Stability of the oxygen sensing system for both films at 25 °C.

² 7 different temperatures with each 4 different oxygen concentrations while 5 images are taken of each combination.

4.4.2.4 Response time of the film

In order to analyse the response time of the film, a chip with a PS-film is filled alternating with water with approximately 0%(air) and with 20%(air) oxygen, and the intensity is measured with a highly sensitive reflex camera at a rate of approximately 2.5 Hz. The response of the sensor is depicted in fig. 4.21. In case of increasing oxygen concentration, the response time is determined as 0.93 ± 0.02 s and in case of decreasing concentration as 0.88 ± 0.03 s. Consequently, the sensor is much slower than the lifetime of the film which is the theoretical minimal response time. The difference is due to the porosity of the film, where the oxygen has to dissolve from the sample liquid and diffuse through the film.

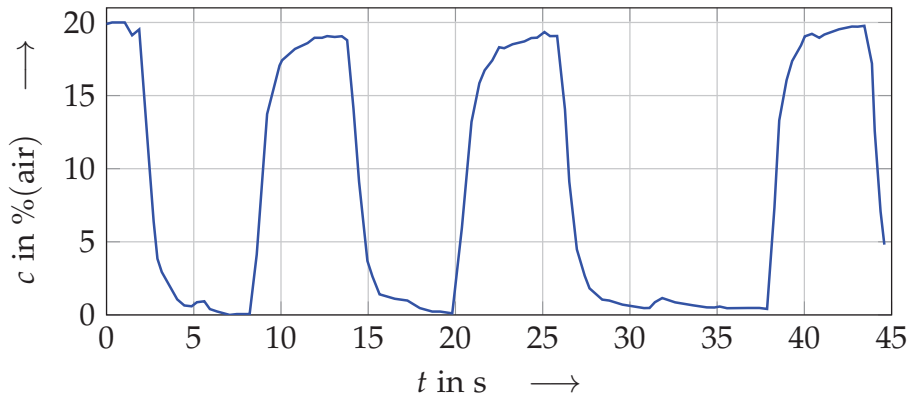


Figure 4.21: Step response of the PS-film.

4.4.2.5 Phase shift of the polystyrene film

The measured phase depends on the oxygen concentration, but also on the different excitation signals as discussed below. The following experiments are run with the PS-film at room temperature (22 ± 1 °C). Furthermore, each measurement point represents the mean value of five measurements, which are determined out of the average of 256 cycles with the oscilloscope.

Excitation parameters

In a first experiment, the minimal excitation voltage³ of the LED $U_{LED,min}$ is altered while the maximal voltage remains 10 V for an excitation frequency of 4 kHz. Consequently, the offset and the amplitude vary. As shown in fig. 4.22(a), the phase for any oxygen concentration increases with increasing $U_{LED,min}$. The phase shift also increases from e.g. 6.6° for $U_{LED,min} = 4$ V to 10.7° at 7 V. The standard deviation of the signals has a minimum of 0.007° at 4 V. Theoretically, the phase between

³The minimal voltage equals the offset minus the amplitude.

the excitation signal and the luminescent signal does not depend on the amplitudes. Therefore, the reason for the determined performance might be either some non-linearities of the electrical network or the superposition of the phosphorescent light by background light or reflected light. For further measurements, the lower amplitude is set to 4 V, which is a good compromise between high quality (i.e. low standard deviation) and high phase shift of the signal.

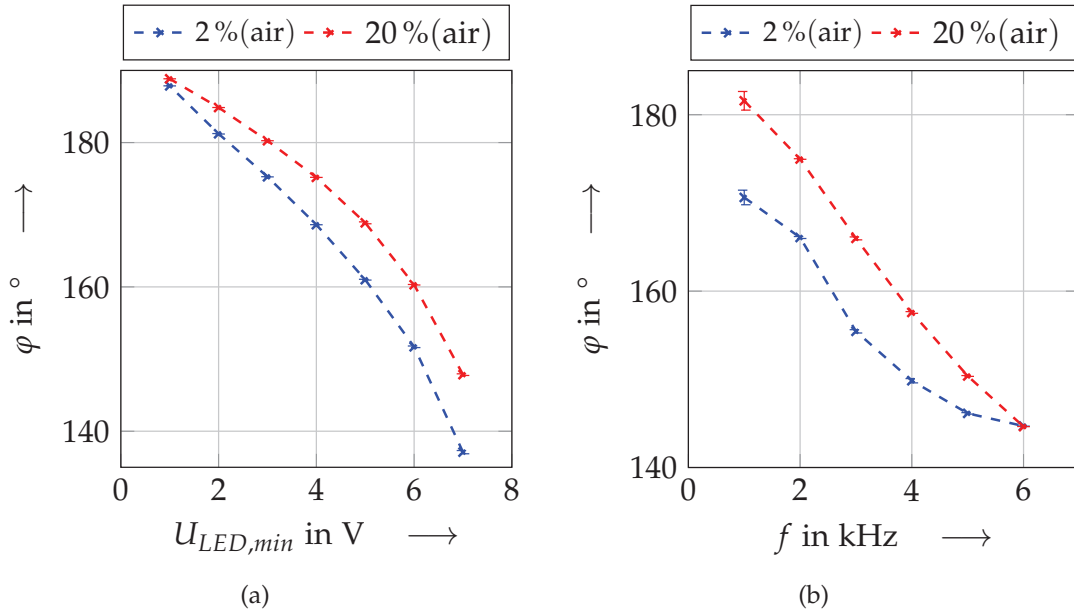


Figure 4.22: Measured phase for oxygen concentrations of 2% (air) (blue) and 20% (air) for different input signals: (a) different excitation voltages which vary between $U_{LED,min}$ and 10 V (b) different excitation frequencies.

The second main excitation parameter is the frequency. With increasing frequency, the phase decreases with a maximal phase shift at 3 kHz, as shown in fig. 4.22(b). Theoretically, the phase increases linearly with the frequency but the intensity of the signal decreases. Due to this decrease, the signals are too low for frequencies above 5 kHz. For this setup, 3 kHz is found as optimal operating frequency.

Oxygen-sensing

Based on the mentioned excitation parameters, the phase for different oxygen concentration is presented in fig. 4.23(a). Here, the phase increases with increasing oxygen concentrations.

Based on the theoretical model (see sec. 4.1.3), the phase of the signal depends on the oxygen concentration as

$$\varphi(c_{O_2}) = \varphi_0 - \arctan\left(\frac{2\pi f \tau_0}{1 + K_{SV} c_{O_2}}\right), \quad (4.10)$$

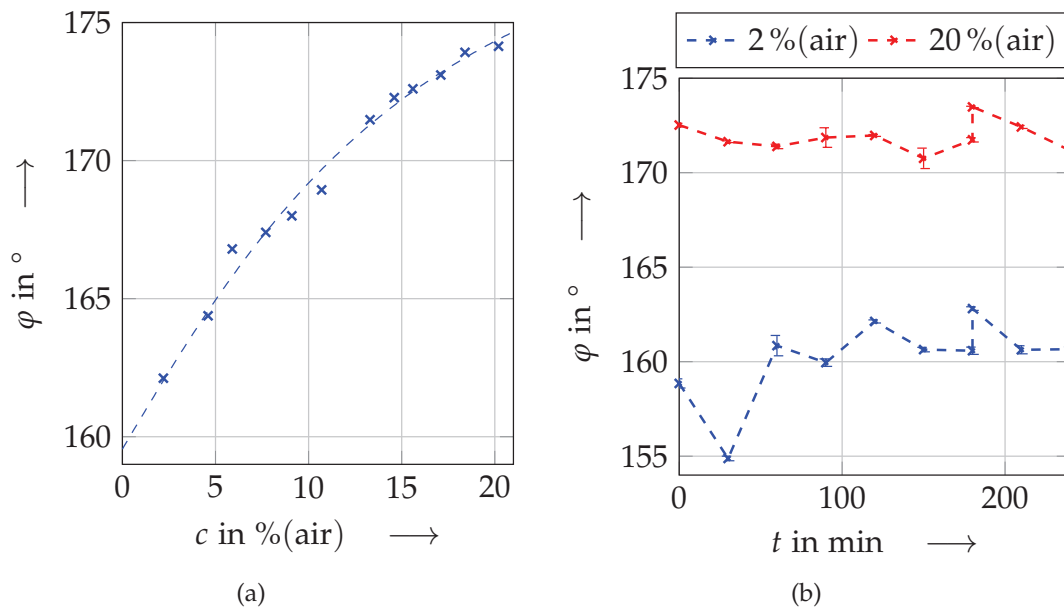


Figure 4.23: Measured phase of the sensor: (a) phase for different oxygen concentration and the fitted curve (dashed) of the theoretical model with fitted parameters (b) long-term measurement of the phase, for which the sample inside the chip is refreshed after 180 min.

where φ_0 is the offset of the phase that depends, among others, on the electrical network. The parameter $\tau_0 = 31 \mu\text{s}$, $K_{SV} = 0.0611 / \text{% (air)}$ and $\varphi_0 = 189.2^\circ$ are fitted with a least-square fitting algorithm. In this case, the uncertainty to calculate the oxygen concentration is about $\pm 0.6 \text{ % (air)}$ in the given range. The lifetime is found as $31 \mu\text{s}$, while the values found in the literature are higher and vary between $64 \mu\text{s}$ [5] and $97 \mu\text{s}$ [66]. The fitted curve of the phase shift is also shown in fig. 4.23(a).

In a further experiment, the measurement of a sample with 20% (air) and a second one with 2% (air) is repeated every 30 min. After 180 min, both samples are refreshed. During the entire measurement, the phases are $171.9 \pm 0.8^\circ$ for 20% (air) and $160.2 \pm 2.1^\circ$ for 2% (air). The refreshment of the samples results in higher phases which might be caused by a different sample temperature.

4.4.2.6 Comparison of the read-out methods

The concentration of the dissolved oxygen can be determined by measuring the intensity as well as the phase shift. In comparison, the read-out of the intensity is more precise than the read-out of the phase shift. The read-out of the phase shift suffers from the weak signal of the phosphorescent film and thus requires electrical filters and amplifiers. Though, the signal of SG-film as well as the PS-film with

reduced spot-size⁴ are too weak to allow reliable measurements. In contrast, the Raspberry Pi camera can cope with this problem by long exposure times of several hundred ms. Consequently, the read-out of the intensity is better suited for weak signals and for the SG-films.

In theory, the read-out of the phase shift is more reliable because changes of the light intensity (e.g. due to different background light or photobleaching) does not influence the measurement. However, the experiments of the different excitation parameters such as the voltage show a correlation with the phase. The reason might be a superposition with luminescence of other parts, such as the holder, or nonlinearities of the photodiode and the amplification circuit. Therefore, the theoretical advantage of the read-out of the phase cannot be confirmed by experiments.

Additionally, the intensity read-out is completely controlled by the Raspberry Pi which also drives the temperature control. In contrast, the read-out of the phase shift requires a waveform generator and an oscilloscope, which means that the measurement is not as automated as the intensity. Therefore, the intensity method is chosen for the following experiments with mammalian cells.

4.4.3 Cell experiments

The oxygen consumption of HaCaT cells is measured in the presented chip with the PS-film and the read-out of the intensity. The methods of the experiments are described in sec. 4.4.3.1. The oxygen uptake of the cells is discussed exemplary at 37 °C in sec. 4.4.3.2. As shown in sec. 4.4.3.3, the oxygen consumption rate (OCR) depends strongly on the temperature.

4.4.3.1 Methods

The following experiments are done with HaCaT cells that are cultured prior to the experiments in standard conditions in an incubator. Unless stated otherwise, the culture medium consists of 10 % FBS, 89.5 % DMEM-medium and 0.5 % Penicillin-Streptomycin. The cells are removed with TrypLE from the culture flasks and centrifuged for 3 min at 1200 rpm. Subsequently, the liquid is replaced with the culture medium and the solution is mixed in a vortexer at 1500 rpm for another 3 min. Finally, the solution is filled into the chips. In parallel, two times 10 μ L are filled into a Neubauer counting chamber, in which the cells are counted at least four times in volumes of about 0.34 μ L each. The standard deviation regarding the number of cells is calculated from these eight values. The oxygen measurements are repeated at least three times and the different spots are evaluated to determine

⁴Such a chip contains fewer spots or smaller spots with the oxygen sensitive film.

the uncertainty of the oxygen uptake. Measurements, in which bubbles are visible inside the chamber, are not evaluated for the following results.

4.4.3.2 Oxygen consumption of cells

Fig. 4.24 shows exemplary the oxygen consumption of HaCaT cells at 37 °C. At all three spots, the oxygen concentration decreases similarly. The oxygen is consumed continuously and with similar rates until almost no oxygen is left. This behaviour is described theoretically by the Michaelis-Menten-kinetics, which predict that the oxygen consumption of the cells is independent of the amount of available oxygen until very low concentrations below 10 μM are reached (see also sec. 3.1.3 [112]). Furthermore, the oxygen consumption of the film due to photo-oxidation with the same medium at the same temperature is significantly lower than the oxygen consumption with the medium and the cells.

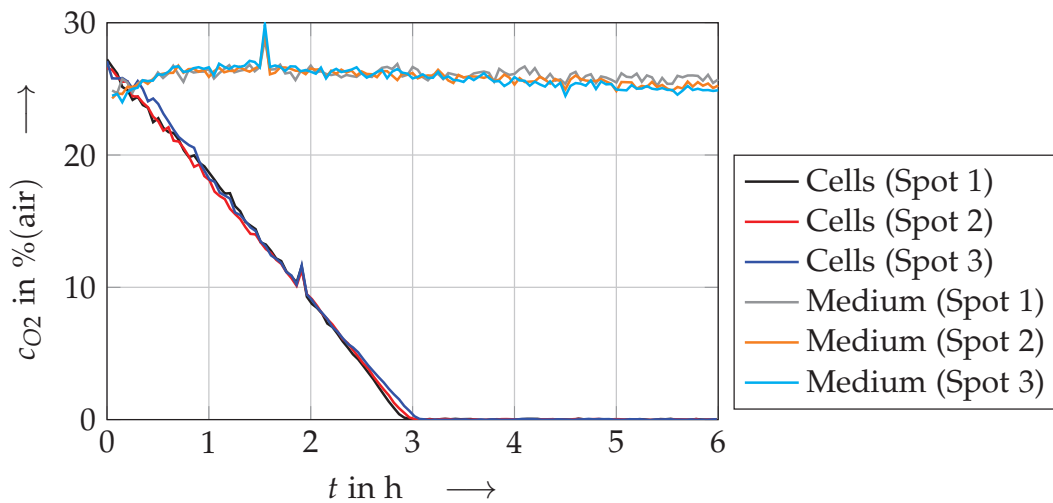


Figure 4.24: Comparison of the decay of the oxygen concentration with HaCaT cells (concentration $12.9 \pm 1.2 \times 10^8 \frac{\text{cell}}{\text{L}}$) at 37 °C.

The cell concentration is $12.9 \pm 1.2 \times 10^8 \frac{\text{cell}}{\text{L}}$ and the entire dissolved oxygen (here $0.26 \frac{\text{mmol}}{\text{L}}$) inside the chip is consumed within $3.04 \pm 0.06 \text{ h}$. Therefore, the oxygen consumption of the chip with the cells is about $24.3 \pm 0.1 \times 10^{-8} \frac{\text{mol}}{\text{L s}}$. At the same time, the oxygen consumption of the device due to photo-oxidation is about $4.7 \times 10^{-10} \frac{\text{mol}}{\text{L s}}$. Considering the cell concentration, the total oxygen consumption per cell is about $18.9 \pm 2.3 \frac{\text{amol}}{\text{cell s}}$ which is in the typical range of mammalian cells of 10 to 50 $\frac{\text{amol}}{\text{cell s}}$ [112].

4.4.3.3 Temperature dependency of the oxygen consumption

The uptake of the oxygen depends on the temperature as well as on the number of cells, as shown in fig. 4.25(a). Basically, the uptake, which is the change of concentration per time, increases linearly with the number of cells as expected from the theoretical considerations in which more cells consume more oxygen. The ratio of the uptake and the number of cells gives the oxygen consumption rate (OCR). The mean OCR is plotted in fig. 4.25(a) as well.

The oxygen consumption rate increases with the temperature, as shown in fig. 4.25(b). The OCR at 37 °C and 40 °C is roughly the same and much higher than at lower temperatures. This indicates an increased metabolism at higher temperatures.

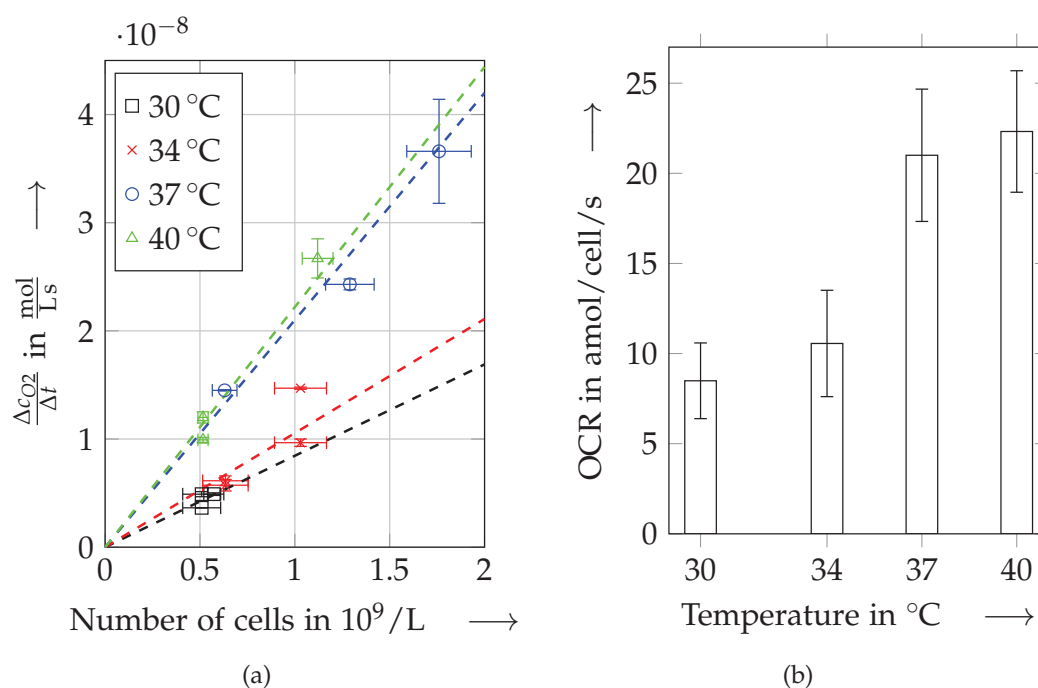


Figure 4.25: Temperature dependence of oxygen consumption: (a) Correlation between the speed of the oxygen decay and the number of cells for different temperatures with the dashed lines as the approximated linear functions (b) Oxygen consumption rate per cell for different temperatures.

4.5 Conclusion

The integration of a phosphorescent film, which is sensitive to oxygen, into a closed microfluidic chip is a reliable and elegant method to measure the concentration of dissolved oxygen. The sensing principle is based on quenching of the excited

luminescent dye. As water also quenches the dye, this sensor is actually only suited as gas sensor and not for liquid samples. A practical way out is to embed the dye in a porous but hydrophobic matrix, so that the oxygen has to dissolve from the liquid and diffuses into the gas-filled pores of the matrix. The second advantage of this approach is the extremely increased surface of porous materials compared to flat surfaces. Hence, this sensor could be considered as functionalised volume instead of functionalised surface. However, this sensor cannot measure the dissolved oxygen in oil or alcohols, which would require a lipophobic matrix.

For the presented device, the oxygen sensitive dye PtTFPP is chosen out of a large variety of dyes because of its commercial availability and the promising results in the literature. However, this dye is not very stable at high temperatures that occur during the fabrication (especially during the bonding process), so that the choice of the process parameters requires special care. Therefore, a different dye might be better suited for the presented chip, but only little information is available about the thermal stability of other dyes.

Similar to the dye, there is also a large range of suitable matrices. For this study, devices with a matrix out of polystyrene (PS-film) and organically modified silica gel (SG-film) are fabricated. In comparison, the fabrication of the PS-film is easier and the film is more sensitive than the SG-film. The results indicate that only part of the dye is quenched by oxygen while the rest is not quenched, probably because it is not on the surface of the porous matrix. The comparison shows that the quenched portion of the PS-film is about 3 times higher than the SG-film. In contrast, the SG-film shows a 35 times reduced photo-oxidation, which makes this film more suitable for long-term experiments while the PS-film can be used for short-term measurements.

The characterisation of the film also shows the strong influence of temperature on the intensity. Therefore, the temperature has to be measured or kept constant while measuring the oxygen concentration. Otherwise, an increase in temperature of about 1 K results already in an additional measurement error of about 1.5% (air). Therefore, a heating element and a temperature sensing element are integrated on the back side of the chip. Both elements show a very good stability and thus enable a reliable and precise control of the temperature.

The read-out of the oxygen measurement is either based on the change of intensity or on the lifetime. The intensity measurement is less complex and more prone to measurement errors e.g. due to different excitation light or photo-degradation of the film. In contrast, the read-out of the phase shift which correlates to the lifetime requires a more sophisticated electrical setup, but should be more robust according to the theory. However, the intensity measurements show a lower measurement uncertainty compared to the phase shift, which suffers from the weak signals.

Furthermore, the intensity measurement is easier to automate and does not require any expensive equipment. So, the presented measurement of the intensity based on a Raspberry Pi camera is found as a well suited read-out method.

The chip requires fluidic connections to insert the sample solution, electrical connections for the heater and temperature sensor, as well as an optical interface for the actual oxygen measurements. All these connections from the chip to the outer world are integrated in the 3D-printed holder and assembly. Their fabrication is low-cost compared to other technologies like injection moulding or milling processes and the design is individually adapted on the chip. Furthermore, the chip is only clamped and not glued or soldered so that it can be replaced within 1 min. Consequently, 3D-printed holder are very attractive for the connection of microfluidic chips to the macroscopic world.

The presented oxygen sensor requires a lot of equipment in addition to the microfluidic chip. This includes among other the optical components like the excitation light source or the detector, the control unit or the temperature control. Though, the presented setup has a small footprint of the measurement assembly⁵ and of the control parts⁶. Furthermore, all components apart from the microfluidic chip cost less than 150 € together. Because of low costs, small footprint and the easy usage caused by the implemented algorithm, the system is ready to be used by biologists or lab technicians in their labs.

4.6 Outlook

The presented setup is able to determine the oxygen consumption rate of mammalian cells. However, the uncertainty of the results is still rather high, which limits the significance of the results. The reasons for the uncertainty are discussed below as well as suitable solutions.

Air bubbles

It occurs from time to time that small air bubbles are flushed into the chip, which might adhere on the hydrophobic oxygen sensor spots. Obviously, these bubbles contain oxygen that can be consumed by the cells in addition to the dissolved oxygen and thus result in a apparently lower OCR than it is in reality.

The trapping of bubbles could be reduced by smaller spots or a higher chamber. Additionally, some structures might be added near the inlets to trap and remove bubbles [20, 22, 64].

⁵This includes the chip, the assembly and the optical components.

⁶The control parts are the Raspberry Pi and the electrical network.

Oxygen diffusion from the inlets and outlets

The measurement of the oxygen consumption takes place in the main chamber. As valves are difficult to realise with standard clean room technologies, the measurement chamber is always connected to the inlets and outlets. The inlets are a potential source of measurement errors because of the following reasons:

- Small air bubbles might be trapped, e.g. near the O-rings, or oxygen might diffuse from or through the O-rings or holders into the sample liquid.
- The inlets also contain cells which consume the oxygen. However, the temperature is lower which means that less oxygen is consumed here. Therefore, the oxygen concentration decreases slower than in the main chamber because of the reduced respiration.
- The temperature of sample liquid inside the holder is lower than inside the chip. The solubility of oxygen decreases with increasing temperatures. Therefore, the partial pressure of oxygen in the main measurement chamber is higher than in the holder directly after heating the chip. As a consequence, oxygen might diffuse out of the chamber after starting the experiment.
- For future experiments, it might be interesting to analyse also the oxygen production of algae by photosynthesis. Here, the algae in the holder are kept in the dark so that they still consume oxygen while the cells in the main chamber produce oxygen in the presence of light.

All mentioned reasons result in a different oxygen concentration of the inlets of the holder and of the main measurement chamber. Consequently, oxygen diffuses in or out of the measurement chamber, but this mass transport is unknown and not constant over time.

To avoid this, one possible solution is a state observer which is a concept of the control theory to estimate internal states. Here, a mathematical model of the system is run and supplied with the same inputs as the real system (temperature and number of cells) and with the measured values (oxygen concentration at each spot). The error between the output of the model and the measured value is minimised by adapting the model. Consequently, further information can be obtained from the internal states such as the oxygen concentration inside the inlets or the diffusion of oxygen along the channel. The advantage of this approach is that the same setup can be used and a large variety of parameters can be observed. However, a thermal, fluidic and biological model of the system have to be realised and the parameters have to be determined, which are complex tasks and might result in modelling errors.

A second solution is fabrication of valves to close the chamber. Novel fabrication methods such as two-photon-polymerisation allow to print 3-dimensional objects with a micrometer resolution inside microfluidic channels. For example, a stage that is moveable in vertical direction can be printed with a predefined distance above the inlets. After printing, metal might be vapour-deposited onto the printed object. By applying a voltage between the stage and the silicon wafer, the stage is pressed electrostatically against the inlets and thus closes the chamber. The advantage is the compactness of such a valve and the possibility to close the chamber. However, the fabrication process is more complex than the used one.

The third solution is an extended length of the channel between the inlets and the measurement chamber. If this channel is very long, the transport of oxygen by diffusion is much lower than the consumption (or production) inside the measurement chamber even at high partial pressure differences. Assuming the oxygen consumption inside the chamber of about $1 \times 10^{-13} \frac{\text{mol}}{\text{s}}$ ⁷, the mass transport through each inlet should be below $5 \times 10^{-16} \frac{\text{mol}}{\text{s}}$ to limit this error to 1 % in a steady state. Such a little mass transport is realised for example by a 25 mm long channel with a width of 100 μm and a height of 200 μm . Such a channel could be easily added to the current design, but does not exclude the diffusion of oxygen.

Number of cells

The OCR of one mammalian cell is determined by measuring the decay of the oxygen consumption inside the chamber relative to the number of cells. The volume of the chamber is relatively small (about 6 μL), which gives space to several thousand cells. However, the cells are not homogeneously distributed because of insufficient mixing or sedimentation. In the presented experiments, the number of cells is determined with a Neubauer counting chamber, in which the number of cells is counted in randomly chosen volumes of 0.3 μL . The cell counting during the presented experiments results already in a uncertainty of about 15 % and the number of cells inside the chip might vary from the number of cells in the counting chamber. Consequently, the uncertainty in the number of cells increases the uncertainty of the OCR-measurement.

A solution might be either larger measurement chambers, in which the inhomogeneity of the sample liquid is levelled out or integrated cell counting elements. The latter option is more elegant and follows more consequently the idea of LoC. Cell counting elements are already available for LoC [91].

⁷Such a oxygen consumption means that the entire oxygen inside the chamber is consumed within 5 h.

5 Conclusion

In this thesis, novel concepts for the cell cultivation and cell analysis inside microfluidic devices are reported which follow the vision of Lab-on-a-Chip (LoC). This idea means that all processes, which are required for one analysis or diagnosis, are integrated in a microfluidic chip. Consequently, LoC-analyses are potentially cheaper, faster or provide new functionalities that are not possible with conventional methods. Numerous publications already reported such functionalities like organ-on-a-chip or culture chambers with integrated sensors. Though, the break-through of LoCs for long-term cultivation and monitoring of mammalian cells is pending due to a lack of suitable interfaces, low ease of use, an inappropriate choice of materials and a high number of external equipment.

The presented devices for cell cultivation and cell analysis are realised with respect to these issues while still providing the advantages of LoC:

Functionalities

Two concepts are investigated to cultivate mammalian cells including the seeding, feeding with nutrients and gases over several hours and days and the passaging. The supply is realised by diffusion through a porous membrane that is arranged either vertically and made out of agarose hydrogel (horizontal supply concept) or horizontally and made out of anodised aluminium oxide (vertical supply concept). This diffusion based approaches result in a continuous and homogeneous supply without any shear stress on the cells and without flushing away of the chemical microenvironment. Both concepts are designed for adherent cell cultures but are also suitable for embedding the cells in 3D-cultures. Both MDCK cells and HaCaT cells show a significant cell growth and thus proved the suitability of the concepts for long-term on-chip cell cultivation.

The cell analysis focuses on the determination of the oxygen consumption of the cells, because this parameter is directly linked to the metabolism being a key process of living cells. In this case, a film with an oxygen-sensitive phosphorescent is integrated into a closed microfluidic chamber, in which the cells grow. The dye is embedded in a porous and hydrophobic matrix, which enables more quenching processes of the dye by oxygen compared to functionalised flat surfaces but also avoids the cross-sensitivity to other compounds and the flushing away of the dye. The influence of the temperature is ruled out by an integrated temperature control,

which also enables constant experimental conditions. As the volume and the cell concentration is known, the oxygen consumption per cell can be determined in real-time to get a direct feedback from the cells.

Fabrication

Both cultivation devices and the analysis chip are based on a fabrication with standard clean room technologies. This allows potentially low costs per device in case of mass production, good control of the design and the future integration of additional functionalities.

Choice of materials

The majority of LoC-devices for cell applications are made at least partially out of PDMS because of the easy fabrication of prototypes and because of its permeability of gases. However, this material has some drawbacks like its infeasibility for mass production or its limited biocompatibility. Therefore, the presented devices relinquish PDMS and contain only materials that are proven or known as non-cytotoxic and suited for clean room processes. The assemblies including the interfaces to the macroscopic world are fabricated by 3D-printing, for which the toxic materials are coated with Parylene to enable well-suited growth conditions.

Interfaces

The connection of the microfluidic devices to the macroscopic world is an underestimated problem which might prevent any utilisation by the users. The interfaces include the fluidic connections but also the electrical connections, which are often realised by glueing of tubes and bonding to a printed circuit board. Both techniques result in high packaging costs and rule out the exchange of components. The presented chips are clamped into 3D-printed holders. These holders connect the chip either to reservoirs, in which the sample liquid is pipetted, or to tubes that are connected to a pump. The electrical interface is realised with spring probes. Consequently, the 3D-printed holders enable a reliable filling and emptying of the chips but also an easy and reversible assembly.

Ease of use

The horizontal supply concept with the hydrogel membranes requires careful preparation of the hydrogel membranes prior to using the device. Once prepared, the usage is straight forward and only the sample liquids have to be replaced periodically. Due to the interface with the 3D-printed holder, this step is rather simple by pipetting the liquids in / out of the reservoir. The same is valid for the vertical supply

concept, except that the preparation step is omitted. The presented devices still require manual action although the automation of these processes is easy to realise.

In contrast, the oxygen measurement and the temperature control of the analysis chip are completely automated so that only the sample preparation, the cell counting, the filling and the data analysis to a certain extent need to be done manually.

External equipment

In an ideal device in the vision of LoC, all functionalities are integrated so that the analysis does not rely on any external equipment. This integration results in low equipment costs but also in a low barrier for end-user. The concepts of cell cultivation lay the focus on the integration of supply structures into the chip as well as into the holder. However, both concepts require an incubator to supply the assembly with suitable gases but also to maintain the desired temperature. Furthermore, microfluidic pumps might be necessary unless the samples are provided from the reservoir. In the future, the temperature control could be added onto the cultivation chips similar to the oxygen sensing chip. A small and low cost gas supply could be realised with standard components so that the incubator is no longer needed.

The oxygen sensor chip has integrated sensing elements and a temperature control. The optical read-out as well as the excitation LED are external but part of the assembly. Furthermore, the electrical circuits and the control unit have a small footprint and are based on low-cost components. Therefore, all functionalities apart of the determination of the cell density are integrated into the setup and thus provide a low barrier for its usage in normal laboratories.

As a conclusion, the presented devices are a major step to convert microfluidic devices into LoC. The chips prove that new functionalities, like porous membranes or oxygen sensing elements, can be integrated into microfluidic devices while using technologies for mass production, only non-cytotoxic materials, providing a high ease of use and relinquish as much external equipment as possible. Consequently, the progress made in this thesis will enable new microfluidic devices for better pharmaceutical research to provide new therapies with lower costs, higher efficiency and enhanced results.

Bibliography

- [1] Miguel A. Acosta, Xiao Jiang, Pin-Kang Huang, Kyle B. Cutler, Christine S. Grant, Glenn M. Walker, and Michael P. Gamcsik. A microfluidic device to study cancer metastasis under chronic and intermittent hypoxia. *Biomicrofluidics*, 8(5):054117, 2014.
- [2] Claudia Altamirano, Julio Berríos, Mauricio Vergara, and Silvana Becerra. Advances in improving mammalian cells metabolism for recombinant protein production. *Electronic Journal of Biotechnology*, 16(3), 2013.
- [3] Helene Andersson and Albert van den Berg. Microfluidic devices for cellomics: a review. *Sensors and Actuators B: Chemical*, 92(3):315–325, 2003.
- [4] Pierre Aymard, David R. Martin, Kevin Plucknett, Tim J. Foster, Allan H. Clark, and Ian T. Norton. Influence of thermal history on the structural and mechanical properties of agarose gels. *Biopolymers*, 59(3):131–144, 2001.
- [5] Denis Badocco, Andrea Mondin, and Paolo Pastore. Signal drift of oxygen optical sensors. part i: Rationalization of the drift nature and its experimental check with a light intensity detection based sensor. *Sensors and Actuators B: Chemical*, 181:943–948, 2013.
- [6] Ross Booth and Hanseup Kim. Characterization of a microfluidic in vitro model of the blood-brain barrier (μ BBB). *Lab on a Chip*, 12(10):1784, 2012.
- [7] Dorothea Brüggemann. Nanoporous aluminium oxide membranes as cell interfaces. *Journal of Nanomaterials*, 2013:1–18, 2013.
- [8] Stephanie J. Bryant, Charles R. Nuttelman, and Kristi S. Anseth. Cytocompatibility of UV and visible light photoinitiating systems on cultured NIH/3t3 fibroblasts in vitro. *Journal of Biomaterials Science, Polymer Edition*, 11(5):439–457, 2000.
- [9] Frank Bunge, Christian Habben, Sander van den Driesche, and Michael J. Vellekoop. Integration and characterization of nanoporous aluminium oxide membranes in microfluidic chips. In *2018 IEEE 31th International Conference on Micro Electro Mechanical Systems (MEMS)*, pages 1237–1240, Jan 2018.
- [10] Frank Bunge, Sander van den Driesche, and Michael J. Vellekoop. Hydrophobic self-assembled monolayers as guiding structures for agarose hydrogels in microfluidic chips. *Proc. microTAS - 19th International Conference on Miniaturized Systems for Chemistry and Life Sciences, Korea*, pages 1472–1474, 2015.

- [11] Frank Bunge, Sander van den Driesche, and Michael J. Vellekoop. Gas supply through agarose walls in cell culturing microchips. *Advances in Science and Technology*, 100:115–119, 2016.
- [12] Frank Bunge, Sander van den Driesche, and Michael J. Vellekoop. Symmetric surficial phaseguides: a passive technology to generate wall-less channels by two-dimensional guiding elements. *Microfluidics and Nanofluidics*, 20(7), 2016.
- [13] Frank Bunge, Sander van den Driesche, and Michael J. Vellekoop. Easy-to-use microfluidic chip for long-term 3D-cell cultures. *Proc. SPIE - Conference*, 2017.
- [14] Frank Bunge, Sander van den Driesche, and Michael J. Vellekoop. Microfluidic platform for the long-term on-chip cultivation of mammalian cells for lab-on-a-chip applications. *Sensors*, 17(7):1603, 2017.
- [15] Frank Bunge, Sander van den Driesche, and Michael J. Vellekoop. A novel on-chip element to provide mammalian cell cultivation and passaging to labs-on-chips. In *2017 19th International Conference on Solid-State Sensors, Actuators and Microsystems (TRANSDUCERS)*. IEEE, 2017.
- [16] Frank Bunge, Sander van den Driesche, Anya Waite, Ursula Mirastschijski, and Michael J. Vellekoop. μ respirometer to determine the oxygen consumption rate of mammalian cells in a microfluidic cell culture. In *2017 IEEE 30th International Conference on Micro Electro Mechanical Systems (MEMS)*, pages 414–417, January 2017.
- [17] Frank Bunge, Sander van den Driesche, Anya Waite, Ursula Mirastschijski, and Michael J. Vellekoop. Microfluidic oxygen sensor based on silica gels for longterm experiments. In *2018 IEEE 31th International Conference on Micro Electro Mechanical Systems (MEMS)*, pages 1221–1224, Jan 2018.
- [18] Sandra Burghoff and Jürgen Schrader. Secretome of human endothelial cells under shear stress. *Journal of Proteome Research*, 10(3):1160–1169, 2011.
- [19] M.R. Chatni, D.E. Maier, and D.M. Porterfield. Evaluation of microparticle materials for enhancing the performance of fluorescence lifetime based optrodes. *Sensors and Actuators B: Chemical*, 141(2):471–477, 2009.
- [20] Daming Cheng and Hongrui Jiang. A debubbler for microfluidics utilizing air-liquid interfaces. *Applied Physics Letters*, 95(21):214103, 2009.
- [21] Daniel T. Chiu, Andrew J. deMello, Dino Di Carlo, Patrick S. Doyle, Carl Hansen, Richard M. Maceiczky, and Robert C.R. Wootton. Small but perfectly formed? successes, challenges, and opportunities for microfluidics in the chemical and biological sciences. *Chem*, 2(2):201–223, 2017.
- [22] Munseok Choi, Yang Na, and Sung-Jin Kim. Hydrophilic strips for preventing air bubble formation in a microfluidic chamber. *Electrophoresis*, 36(23):2896–2901, 2015.

- [23] Chen-Shane Chu and Yu-Lung Lo. 2D full-field measurement of oxygen concentration based on the phase fluorometry technique that uses the four-frame integrating-bucket method. *Sensors and Actuators B: Chemical*, 147(1):310 – 315, 2010.
- [24] Cheng-Shane Chu and Che-An Lin. Optical fiber sensor for dual sensing of temperature and oxygen based on PtTFPP/CF embedded in sol-gel matrix. *Sensors and Actuators B: Chemical*, 195:259–265, 2014.
- [25] Bong Geun Chung, Kwang-Ho Lee, Ali Khademhosseini, and Sang-Hoon Lee. Microfluidic fabrication of microengineered hydrogels and their application in tissue engineering. *Lab Chip*, 12(1):45–59, 2012.
- [26] Kosmas Deligkaris, Tadele Shiferaw Tadele, Wouter Olthuis, and Albert van den Berg. Hydrogel-based devices for biomedical applications. *Sensors and Actuators B: Chemical*, 147(2):765–774, 2010.
- [27] Kangfa Deng, Mathias Rohn, Margarita Güenther, and Gerald Gerlach. Thermal microactuator based on temperature-sensitive hydrogel. *Procedia Engineering*, 120:57–62, 2015.
- [28] A. Soleimani Dorcheh and M.H. Abbasi. Silica aerogel: synthesis, properties and characterization. *Journal of Materials Processing Technology*, 199(1-3):10–26, 2008.
- [29] Jon F. Edd, Dino Di Carlo, Katherine J. Humphry, Sarah Köster, Daniel Irimia, David A. Weitz, and Mehmet Toner. Controlled encapsulation of single-cells into monodisperse picolitre drops. *Lab on a Chip*, 8(8):1262, 2008.
- [30] Josef Ehgartner, Philipp Sulzer, Tobias Burger, Alice Kasjanow, Dominique Bouwes, Ulrich Krühne, Ingo Klimant, and Torsten Mayr. Online analysis of oxygen inside silicon-glass microreactors with integrated optical sensors. *Sensors and Actuators B: Chemical*, 228:748–757, 2016.
- [31] Barbara Enko, Sergey M. Borisov, Johannes Regensburger, Wolfgang Bäuml, Georg Gescheidt, and Ingo Klimant. Singlet oxygen-induced photodegradation of the polymers and dyes in optical sensing materials and the effect of stabilizers on these processes. *The Journal of Physical Chemistry A*, 117(36):8873–8882, 2013. PMID: 23964784.
- [32] Mandy B. Esch, Hidetaka Ueno, Dawn R. Applegate, and Michael L. Shuler. Modular, pumpless body-on-a-chip platform for the co-culture of gi tract epithelium and 3D primary liver tissue. *Lab on a Chip*, 16:2719–2729, 2016.
- [33] Benjamin D. Fairbanks, Michael P. Schwartz, Christopher N. Bowman, and Kristi S. Anseth. Photoinitiated polymerization of PEG-diacrylate with lithium phenyl-2,4,6-trimethylbenzoylphosphinate: polymerization rate and cytocompatibility. *Biomaterials*, 30(35):6702–6707, 2009.

- [34] Jonas Flueckiger, Vahid Bazargan, Boris Stoeber, and Karen C. Cheung. Characterization of postfabricated parylene c coatings inside PDMS microdevices. *Sensors and Actuators B: Chemical*, 160(1):864–874, 2011.
- [35] Samuel P. Forry and Laurie E. Locascio. On-chip CO₂ control for microfluidic cell culture. *Lab on a Chip*, 11(23):4041, 2011.
- [36] Thomas Frisk, Susanna Rydholm, Helene Andersson, Göran Stemme, and Hjalmar Brismar. A concept for miniaturized 3-d cell culture using an extracellular matrix gel. *ELECTROPHORESIS*, 26(24):4751–4758, 2005.
- [37] Gerald Gerlach, Margarita Günther, Jörg Sorber, Gunnar Suchaneck, Karl-Friedrich Arndt, and Andreas Richter. Chemical and pH sensors based on the swelling behavior of hydrogels. *Sensors and Actuators B: Chemical*, 111-112:555–561, 2005.
- [38] Emel I. Goksu, Matthew I. Hoopes, Barbara A. Nellis, Chenyue Xing, Roland Faller, Curtis W. Frank, Subhash H. Risbud, Joe H. Satcher, and Marjorie L. Longo. Silica xerogel/aerogel-supported lipid bilayers: Consequences of surface corrugation. *Biochimica et Biophysica Acta (BBA) - Biomembranes*, 1798(4):719–729, 2010.
- [39] Samantha Grist, Jonathan Schmok, Meng-Chi Liu, Lukas Chrostowski, and Karen Cheung. Designing a microfluidic device with integrated ratiometric oxygen sensors for the long-term control and monitoring of chronic and cyclic hypoxia. *Sensors*, 15(8):20030–20052, 2015.
- [40] Sebastian Häfner, Philipp Frank, Enrico Langer, Denise Gruner, Ulrike Schmidt, Martin Elstner, Gerald Gerlach, and Andreas Richter. Chemically controlled micro-pores and nano-filters for separation tasks in 2D and 3D microfluidic systems. *RSC Adv.*, 7(78):49279–49289, 2017.
- [41] Skarphedinn Halldorsson, Edinson Lucumi, Rafael Gómez-Sjöberg, and Ronan M.T.Fleming. Advantages and challenges of microfluidic cell culture in polydimethylsiloxane devices. *Biosens. Bioelectron.*, 63:218–231, 2015.
- [42] Koji Hattori, Yoichi Munehira, Hideki Kobayashi, Taku Satoh, Shinji Sugiura, and Toshiyuki Kanamori. Microfluidic perfusion culture chip providing different strengths of shear stress for analysis of vascular endothelial function. *Journal of Bioscience and Bioengineering*, 118(3):327–332, 2014.
- [43] Jonas Hereijgers, Gert Desmet, Tom Breugelmans, and Wim De Malsche. Strategies to integrate porous layers in microfluidic devices. *Microelectronic Engineering*, 132:1–13, 2015.
- [44] Todd R. Hoare and Daniel S. Kohane. Hydrogels in drug delivery: Progress and challenges. *Polymer*, 49(8):1993–2007, 2008.

- [45] Aaron M. Hosios, Vivian C. Hecht, Laura V. Danai, Marc O. Johnson, Jeffrey C. Rathmell, Matthew L. Steinhauser, Scott R. Manalis, and Matthew G. Vander Heiden. Amino acids rather than glucose account for the majority of cell mass in proliferating mammalian cells. *Developmental Cell*, 36(5):540–549, 2016.
- [46] Jerrod E. Houser and Kurt R. Hebert. The role of viscous flow of oxide in the growth of self-ordered porous anodic alumina films. *Nature Materials*, 8(5):415–420, 2009.
- [47] Paul J. Hung, Philip J. Lee, Poorya Sabounchi, Robert Lin, and Luke P. Lee. Continuous perfusion microfluidic cell culture array for high-throughput cell-based assays. *Biotechnology and Bioengineering*, 89(1):1–8, 2004.
- [48] Nazar Ileri. Fabrication of functional silicon-based nanoporous membranes. *Journal of Micro/Nanolithography, MEMS, and MOEMS*, 11(1):013012, 2012.
- [49] Abdul Mutalib Md Jani, Dusan Losic, and Nicolas H. Voelcker. Nanoporous anodic aluminium oxide: Advances in surface engineering and emerging applications. *Progress in Materials Science*, 58(5):636–704, 2013.
- [50] Jessie S. Jeon, Simone Bersini, Mara Gilardi, Gabriele Dubini, Joseph L. Charest, Matteo Moretti, and Roger D. Kamm. Human 3D vascularized organotypic microfluidic assays to study breast cancer cell extravasation. *PNAS*, 112(1):214–219, 2014.
- [51] Paula C.A. Jerónimo, Alberto N. Araújo, and M. Conceição B.S.M. Montenegro. Optical sensors and biosensors based on sol–gel films. *Talanta*, 72(1):13–27, 2007.
- [52] B. Johnson-White and J. Golden. Reduction of background signal in automated array biosensors. *Meas. Sci. Technol.*, 16(9):N29–N31, 2005.
- [53] Hari R. Kumar, Xiaoling Zhong, Derek J. Hoelz, Frederick J. Rescorla, Robert J. Hickey, Linda H. Malkas, and John A. Sandoval. Three-dimensional neuroblastoma cell culture: proteomic analysis between monolayer and multicellular tumor spheroids. *Pediatric Surgery International*, 24(11):1229–1234, 2008.
- [54] Ngoc Lieu Le, Mathias Ulbricht, and Suzana P. Nunes. How do polyethylene glycol and poly(sulfobetaine) hydrogel layers on ultrafiltration membranes minimize fouling and stay stable in cleaning chemicals? *Industrial & Engineering Chemistry Research*, 56(23):6785–6795, 2017.
- [55] Dong Sup Lee, Su Jin Kim, Eun Bi Kwom, Cheol Whee Park, Su Min Jun, Bumkyoo Choi, and Sae Woong Kim. Comparison of in vivo biocompatibilities between parylene-c and polydimethylsiloxane for implantable microelectronic devices. *Bulletin of Materials Science*, 36(6):1127–1132, 2013.
- [56] Ji Soo Lee, Roberto Romero, Yu Mi Han, Hee Chan Kim, Chong Jai Kim, Joon-Seok Hong, and Dongeun Huh. Placenta-on-a-chip: a novel platform to study the biology of the human placenta. *The Journal of Maternal-Fetal & Neonatal Medicine*, 29(7):1046–1054, 2015.

- [57] Yong-Eun Koo Lee, Elyse E. Ulbrich, Gwangseong Kim, Hoejin Hah, Christen Strollo, Wenzhe Fan, Rajan Gurjar, SangMan Koo, and Raoul Kopelman. Near infrared luminescent oxygen nanosensors with nanoparticle matrix tailored sensitivity. *Analytical Chemistry*, 82(20):8446–8455, 2010.
- [58] Kin Fong Lei, Hsueh-Peng Tseng, Chia-Yi Lee, and Ngan-Ming Tsang. Quantitative study of cell invasion process under extracellular stimulation of cytokine in a microfluidic device. *Scientific Reports*, 6(1), 2016.
- [59] A. P. Li, F. Müller, A. Birner, K. Nielsch, and U. Gösele. Hexagonal pore arrays with a 50–420 nm interpore distance formed by self-organization in anodic alumina. *Journal of Applied Physics*, 84(11):6023–6026, 1998.
- [60] Jr-Lung Lin, Shih-Siou Wang, Min-Hsien Wu, and Chih-Chin Oh-Yang. Development of an integrated microfluidic perfusion cell culture system for real-time microscopic observation of biological cells. *Sensors*, 11(12):8395–8411, 2011.
- [61] Yibo Ling, Jamie Rubin, Yuting Deng, Catherine Huang, Utkan Demirci, Jeffrey M. Karp, and Ali Khademhosseini. A cell-laden microfluidic hydrogel. *Lab on a Chip*, 7(6):756, 2007.
- [62] Kan Liu, Yuliang Deng, Nangang Zhang, Sizhe Li, Huijiang Ding, Feng Guo, Wei Liu, Shishang Guo, and Xing-Zhong Zhao. Generation of disk-like hydrogel beads for cell encapsulation and manipulation using a droplet-based microfluidic device. *Microfluidics and Nanofluidics*, 13(5):761–767, 2012.
- [63] Shih-Jie Lo and Da-Jeng Yao. Get to understand more from single-cells: Current studies of microfluidic-based techniques for single-cell analysis. *International Journal of Molecular Sciences*, 16(8):16763–16777, 2015.
- [64] Conrad Lochovsky, Sanjesh Yasotharan, and Axel Günther. Bubbles no more: in-plane trapping and removal of bubbles in microfluidic devices. *Lab Chip*, 12(3):595–601, 2012.
- [65] Jennie P. Mather and Penelope E. Roberts. *Introduction to Cell and Tissue Culture*. Plenum Press, New York, 1998.
- [66] Santiago Medina-Rodríguez, Marta Marín-Suárez, Jorge Fernando Fernández-Sánchez, Ángel de la Torre-Vega, Etienne Baranoff, and Alberto Fernández-Gutiérrez. High performance optical sensing nanocomposites for low and ultra-low oxygen concentrations using phase-shift measurements. *The Analyst*, 138(16):4607, 2013.
- [67] Iris Mironi-Harpaz, Dennis Yingquan Wang, Subbu Venkatraman, and Dror Seliktar. Photopolymerization of cell-encapsulating hydrogels: Crosslinking efficiency versus cytotoxicity. *Acta Biomaterialia*, 8(5):1838–1848, 2012.
- [68] Mazher Iqbal Mohammed, Steven Haswell, and Ian Gibson. Lab-on-a-chip or chip-in-a-lab: Challenges of commercialization lost in translation. *Procedia Technology*, 20:54–59, 2015.

- [69] Alexandra I. Mot, Jeffrey R. Liddell, Anthony R. White, and Peter J. Crouch. Circumventing the crabtree effect: A method to induce lactate consumption and increase oxidative phosphorylation in cell culture. *The International Journal of Biochemistry & Cell Biology*, 79:128–138, 2016.
- [70] Joshua N. Musher and Roy G. Gordon. Low-temperature CVD TiN as a diffusion barrier between gold and silicon. *Journal of Electronic Materials*, 20(12):1105–1107, 1991.
- [71] K.Y. Ng, Yuan Lin, and A.H.W. Ngan. Compression of micron-sized pillars of anodic aluminium oxide nano-honeycomb. *Journal of the Mechanics and Physics of Solids*, 59(2):251–264, 2011.
- [72] S. Noh and H. Kim. A micro lung chip to assess air pollutant effects. In *2017 IEEE 30th International Conference on Micro Electro Mechanical Systems (MEMS)*, pages 498–501, Jan 2017.
- [73] Datasheet obtained from Sigma Aldrich. "<https://www.sigmaaldrich.com/life-science/cell-culture/learning-center/media-formulations/dme.html>", 23.03.2018.
- [74] Sachiko Ono, Makiko Saito, and Hidetaka Asoh. Self-ordering of anodic porous alumina formed in organic acid electrolytes. *Electrochimica Acta*, 51(5):827–833, 2005.
- [75] Pieter E. Oomen, Maciej D. Skolimowski, and Elisabeth Verpoorte. Implementing oxygen control in chip-based cell and tissue culture systems. *Lab Chip*, 16(18):3394–3414, 2016.
- [76] Jae Hong Park, Bong Geun Chung, Won Gu Lee, Jinseok Kim, Mark D. Brigham, Jaesool Shim, Seunghwan Lee, Changmo Hwang, Naside Gozde Durmus, Utkan Demirci, and Ali Khademhosseini. Microporous cell-laden hydrogels for engineered tissue constructs. *Biotechnology and Bioengineering*, 106(1):138–148, 2010.
- [77] Nadine Pernodet, Mounir Maaloum, and Bernard Tinland. Pore size of agarose gels by atomic force microscopy. *Electrophoresis*, 18(1):55–58, 1997.
- [78] Simon A Pfeiffer and Stefan Nagl. Microfluidic platforms employing integrated fluorescent or luminescent chemical sensors: a review of methods, scope and applications. *Methods and Applications in Fluorescence*, 3(3):034003, 2015.
- [79] Brian J. Polk, Anna Stelzenmuller, Geraldine Mijares, William MacCrehan, and Michael Gaitan. Ag/AgCl microelectrodes with improved stability for microfluidics. *Sensors and Actuators B: Chemical*, 114(1):239–247, 2006.
- [80] J.C. Portais, P. Voisin, M. Merle, and P. Canioni. Glucose and glutamine metabolism in c6 glioma cells studied by carbon 13 NMR. *Biochimie*, 78(3):155–164, 1996.
- [81] R. Portillo-Lara and N. Annabi. Microengineered cancer-on-a-chip platforms to study the metastatic microenvironment. *Lab Chip*, 16(21):4063–4081, 2016.

- [82] Dietmar Puchberger-Enengl, Christian Krutzler, Franz Keplinger, and Michael J. Vellekoop. Single-step design of hydrogel-based microfluidic assays for rapid diagnostics. *Lab Chip*, 14(2):378–383, 2014.
- [83] Dietmar Puchberger-Enengl, Sander van den Driesche, Christian Krutzler, Franz Keplinger, and Michael J. Vellekoop. Hydrogel-based microfluidic incubator for microorganism cultivation and analyses. *Biomicrofluidics*, 9(1):014127, 2015.
- [84] Michela Quaranta, Sergey M. Borisov, and Ingo Klimant. Indicators for optical oxygen sensors. *Bioanalytical Reviews*, 4(2-4):115–157, 2012.
- [85] R. Ramamoorthy, P. K. Dutta, and S. A. Akbar. Oxygen sensors: Materials, methods, designs and applications. *Journal of Materials Science*, 38(21):4271–4282, 2003.
- [86] A. Parvathy Rao, G. M. Pajonk, and A. V. Rao. Effect of preparation conditions on the physical and hydrophobic properties of two step processed ambient pressure dried silica aerogels. *Journal of Materials Science*, 40(13):3481–3489, 2005.
- [87] Sina Reede, Frank Bunge, and Michael J. Vellekoop. Integration of silica aerogels in microfluidic chips. *Proceedings of Eurosensors*, 1(4):298, 2017.
- [88] Keil J. Regehr, Maribella Domenech, Justin T. Koepsel, Kristopher C. Carver, Stephanie J. Ellison-Zelski, William L. Murphy, Linda A. Schuler, Elaine T. Alarid, and David J. Beebe. Biological implications of polydimethylsiloxane-based microfluidic cell culture. *Lab. Chip*, 9(15):2132–2139, 2009.
- [89] Ana C. F. Ribeiro, Victor M. M. Lobo, Derek G. Leaist, Joaquim J. S. Natividade, Luís P. Veríssimo, Marisa C. F. Barros, and Ana M. T. D. P. V. Cabral. Binary diffusion coefficients for aqueous solutions of lactic acid. *Journal of Solution Chemistry*, 34(9):1009–1016, 2005.
- [90] V. Romero, V. Vega, J. García, V.M. Prida, B. Hernando, and J. Benavente. Ionic transport across tailored nanoporous anodic alumina membranes. *Journal of Colloid and Interface Science*, 376(1):40–46, 2012.
- [91] Michael Rosenauer, Wolfgang Buchegger, Inez Finoulst, Peter Verhaert, and Michael Vellekoop. Miniaturized flow cytometer with 3D hydrodynamic particle focusing and integrated optical elements applying silicon photodiodes. *Microfluidics and Nanofluidics*, 10(4):761–771, 2010.
- [92] Eric K. Sackmann, Anna L. Fulton, and David J. Beebe. The present and future role of microfluidics in biomedical research. *Nature*, 507(7491):181–189, 2014.
- [93] Hirotaka Sasaki, Hiroaki Onoe, Toshihisa Osaki, Ryuji Kawano, and Shoji Takeuchi. Parylene-coating in pdms microfluidic channels prevents the absorption of fluorescent dyes. *Sens. Actuators, B*, 150(1):478–482, 2010.

- [94] Bart Schurink and Regina Luttge. Hydrogel/poly-dimethylsiloxane hybrid bioreactor facilitating 3D cell culturing. *Journal of Vacuum Science & Technology B, Nanotechnology and Microelectronics: Materials, Processing, Measurement, and Phenomena*, 31(6):06F903, 2013.
- [95] C.S. Shin, B. Kwak, B. Han, K. Park, and A. Panitch. 3D cancer tumor models for evaluating chemotherapeutic efficacy. *Biomaterials for Cancer Therapeutics: Diagnosis, Prevention and Therapy*, pages 445–460, 2013.
- [96] Yoojin Shin, Sewoon Han, Jessie S Jeon, Kyoko Yamamoto, Ioannis K Zervantonakis, Ryo Sudo, Roger D Kamm, and Seok Chung. Microfluidic assay for simultaneous culture of multiple cell types on surfaces or within hydrogels. *Nature Protocols*, 7(7):1247–1259, 2012.
- [97] Y. Sidorenko, A. Wahl, M. Dauner, Y. Genzel, and U. Reichl. Comparison of metabolic flux distributions for MDCK cell growth in glutamine- and pyruvate-containing media. *Biotechnology Progress*, 24(2):311–320, 2008.
- [98] Sarah Stolberg and Kara E. McCloskey. Can shear stress direct stem cell fate? *Biotechnology Progress*, 25(1):10–19, 2009.
- [99] Grzegorz D. Sulka and Wojciech J. Stępniewski. Structural features of self-organized nanopore arrays formed by anodization of aluminum in oxalic acid at relatively high temperatures. *Electrochimica Acta*, 54(14):3683–3691, 2009.
- [100] Atsushi Takano, Masato Tanaka, and Nobuyuki Futai. On-chip multi-gas incubation for microfluidic cell cultures under hypoxia. *Biomicrofluidics*, 8(6):061101, 2014.
- [101] Annika Thormann, Nico Teuscher, Monika Pfannmöller, Ulrich Rothe, and Andreas Heilmann. Nanoporous aluminum oxide membranes for filtration and biofunctionalization. *Small*, 3(6):1032–1040, 2007.
- [102] Yi-Chin Toh, Chi Zhang, Jing Zhang, Yuet Mei Khong, Shi Chang, Victor D. Samper, Danny van Noort, Dietmar W. Huttmacher, and Hanry Yu. A novel 3D mammalian cell perfusion-culture system in microfluidic channels. *Lab on a Chip*, 7(3):302, 2007.
- [103] Desmond Tromans. Modeling oxygen solubility in water and electrolyte solutions. *Industrial & Engineering Chemistry Research*, 39(3):805–812, 2000.
- [104] Birgit Ungerböck, Verena Charwat, Peter Ertl, and Torsten Mayr. Microfluidic oxygen imaging using integrated optical sensor layers and a color camera. *Lab on a Chip*, 13(8):1593, 2013.
- [105] Sander van den Driesche, Frieder Lucklum, Frank Bunge, and Michael Vellekoop. 3D printing solutions for microfluidic chip-to-world connections. *Micromachines*, 9(2):71, 2018.

- [106] Andries D. van der Meer, Valeria V. Orlova, Peter ten Dijke, Albert van den Berg, and Christine L. Mummery. Three-dimensional co-cultures of human endothelial cells and embryonic stem cell-derived pericytes inside a microfluidic device. *Lab on a Chip*, 13(18):3562, 2013.
- [107] Guilhem Velve-Casquillas, Maël Le Berre, Matthieu Piel, and Phong T. Tran. Microfluidic tools for cell biological research. *Nano Today*, 5(1):28–47, 2010.
- [108] Vernella Vickerman, Jennifer Blundo, Seok Chung, and Roger Kamm. Design, fabrication and implementation of a novel multi-parameter control microfluidic platform for three-dimensional cell culture and real-time imaging. *Lab on a Chip*, 8(9):1468, 2008.
- [109] Lisa R. Volpatti and Ali K. Yetisen. Commercialization of microfluidic devices. *Trends in Biotechnology*, 32(7):347–350, 2014.
- [110] P. Vulto, G. Medoro, L. Altomare, G.A. Urban, M. Tartagni, R. Guerrieri, and N. Manaresi. Selective sample recovery of dep-separated cells and particles by phaseguide-controlled laminar flow. *J. Micromech. and Microeng.*, 16(9):1847–1853, 2006.
- [111] Paul Vulto, Susann Podszun, Philipp Meyer, Carsten Hermann, Andreas Manz, and Gerald A. Urban. Phaseguides: a paradigm shift in microfluidic priming and emptying. *Lab on a Chip*, 11(9):1596, 2011.
- [112] Brett A. Wagner, Sujatha Venkataraman, and Garry R. Buettner. The rate of oxygen utilization by cells. *Free Radical Biol Med*, 51(3):700–712, 2011.
- [113] Xu-dong Wang and Otto S. Wolfbeis. Optical methods for sensing and imaging oxygen: materials, spectroscopies and applications. *Chem. Soc. Rev.*, 43:3666–3761, 2014.
- [114] Z.F. Wang, Y.P. Seah, and Z.P. Wang. Seamless joining of porous membrane with thermoplastic microfluidic devices. *Microelectronic Engineering*, 110:386–391, 2013.
- [115] Andreas Weltin, Kinga Slotwinski, Jochen Kieninger, Isabella Moser, Gerhard Jobst, Marcus Wego, Ralf Ehret, and Gerald A. Urban. Cell culture monitoring for drug screening and cancer research: a transparent, microfluidic, multi-sensor microsystem. *Lab Chip*, 14(1):138–146, 2014.
- [116] Otto S. Wolfbeis. Luminescent sensing and imaging of oxygen: Fierce competition to the clark electrode. *BioEssays*, 37(8):921–928, 2015.
- [117] Changqing Yi, Cheuk-Wing Li, Shenglin Ji, and Mengsu Yang. Microfluidics technology for manipulation and analysis of biological cells. *Analytica Chimica Acta*, 560(1-2):1–23, 2006.
- [118] Toshihisa Yotsuyanagi, Tsuneo Ohkubo, Takafumi Ohhashi, and Ken Ikeda. Calcium-induced gelation of alginic acid and pH-sensitive reswelling of dried gels. *Chemical & Pharmaceutical Bulletin*, 35(4):1555–1563, 1987.

-
- [119] Ting Yu, Zhe Guo, Hui Fan, Jing Song, Yuanbin Liu, Zhancheng Gao, and Qi Wang. Cancer-associated fibroblasts promote non-small cell lung cancer cell invasion by upregulation of glucose-regulated protein 78 (GRP78) expression in an integrated bionic microfluidic device. *Oncotarget*, 2016.
- [120] Xuanqi Zhang, Lingjun Li, and Chunxiong Luo. Gel integration for microfluidic applications. *Lab Chip*, 16(10):1757–1776, 2016.
- [121] Hong Zhuo, Fuchuan Peng, Limei Lin, Yan Qu, and Fachun Lai. Optical properties of porous anodic aluminum oxide thin films on quartz substrates. *Thin Solid Films*, 519(7):2308–2312, 2011.

List of publications

Journal papers

- Frank Bunge, Sander van den Driesche, and Michael J. Vellekoop. Symmetric surficial phaseguides: a passive technology to generate wall-less channels by two-dimensional guiding elements. *Microfluidics and Nanofluidics*, 20(7), 2016.
- Frank Bunge, Sander van den Driesche, and Michael J. Vellekoop. Microfluidic platform for the long-term on-chip cultivation of mammalian cells for lab-on-a-chip applications. *Sensors*, 17(7):1603, 2017.
- Sander van den Driesche, Frieder Lucklum, Frank Bunge, and Michael J. Vellekoop. 3D printing solutions for microfluidic chip-to-world connections. *Micromachines*, 9(2):71, 2018.
- Frank Bunge, Steffen Leopold, Sebastian Bohm, Martin Hoffmann. Scanning micromirror for large, quasi-static 2D-deflections based on electrostatic driven rotation of a hemisphere. *Sensors and Actuators A: Physical*, 243:1, pages 159-166, 2016

Conference proceedings

- Frank Bunge, Sander van den Driesche, and Michael J. Vellekoop. Hydrophobic selfassembled monolayers as guiding structures for agarose hydrogels in microfluidic chips. *microTAS - 19th International Conference on Miniaturized Systems for Chemistry and Life Sciences*, Gyeongju, Korea, 25-29 October 2015.
- Frank Bunge, Sander van den Driesche, and Michael J. Vellekoop. Gas supply through agarose walls in cell culturing microchips. *Cimtec Congress*, Perugia, Italy, 5-9 June 2016
- Frank Bunge, Sander van den Driesche, Anya Waite, Ursula Mirastschijski, and Michael J. Vellekoop. μ respirometer to determine the oxygen consumption rate of mammalian cells in a microfluidic cell culture. *IEEE 30th International Conference on Micro Electro Mechanical Systems (MEMS)*, Las Vegas, USA, 22-26 January 2017.
- Frank Bunge, Sander van den Driesche, and Michael J. Vellekoop. Easy-to-use microfluidic chip for long-term 3D-cell cultures. *SPIE Microtechnologies*, Barcelona, Spain, 8-10 May 2017.
- Frank Bunge, Sander van den Driesche, and Michael J. Vellekoop. A novel on-chip element to provide mammalian cell cultivation and passaging to labs-on-chips. *19th International Conference on Solid-State Sensors, Actuators and Microsystems (TRANSDUCERS)*. IEEE, Kaohsiung, Taiwan, 18-22 June 2017.

- Frank Bunge, Sander van den Driesche, and Michael J. Vellekoop. Mikroinkubator mit Hydrogelmembranen für die Langzeitkultivierung von Säugetierzellen. *Mikrosystemtechnikkongress*, München, Germany, 28-30 October 2017.
- Frank Bunge, Sander van den Driesche, Anya Waite, Ursula Mirastschijski, and Michael J. Vellekoop. Microfluidic oxygen sensor based on silica gels for longterm experiments. *2018 IEEE 31th International Conference on Micro Electro Mechanical Systems (MEMS)*, Belfast, UK, 21-25 January 2018.
- Frank Bunge, Christian Habben, Sander van den Driesche, and Michael J. Vellekoop. Integration and characterization of nanoporous aluminium oxide membranes in microfluidic chips. *2018 IEEE 31th International Conference on Micro Electro Mechanical Systems (MEMS)*, Belfast, UK, 21-25 January 2018.
- Frank Bunge, Martin Oellers, Sander van den Driesche, and Michael J. Vellekoop. Mikrofluidischer Sensor zur Überwachung der Sauerstoffkonzentration. *19. ITG/GMA-Fachtagung Sensoren und Messsysteme*, Nürnberg, Germany, 26-27 June 2018.
- Ali Abdallah, Sander van den Driesche, Lukas Brandhoff, Frank Bunge, Mahmuda Akhtar, Reza Ebrahimifard, Stefan Clara, Bernhard Jakoby, and Michael J. Vellekoop. Microfluidic device for acoustophoresis and dielectrophoresis assisted particle and cell transfer between different fluidic media. *Euroensors*, Freiburg, Germany, 6-9 September 2015
- Sander van den Driesche, Frank Bunge, Sebastian Tepner, Marcus Kotitschke, and Michael J. Vellekoop. Travelling-wave dielectrophoresis allowing flexible microchannel design for suspended cell handling. *SPIE Microtechnologies*, Barcelona, Spain, 8-10 May 2017.
- Frieder Lucklum, Frank Bunge, and Michael J. Vellekoop. Experimental and numerical analysis of complete acoustic band gaps in three-dimensional phononic crystals. *19th International Conference on Solid-State Sensors, Actuators and Microsystems (TRANSDUCERS)*. IEEE, Kaohsiung, Taiwan, 18-22 June 2017.
- Sina Reede, Frank Bunge, and Michael J. Vellekoop. Integration of silica aerogels in microfluidic chips. *Euroensors*, Paris, France, 3-6 September 2017.
- Martin Oellers, Frank Bunge, Poornanchandra Vinayaka, Sander van den Driesche and Michael J. Vellekoop. Flow-ratio monitoring in a microchannel by liquid-liquid interface interferometry. *Euroensors*, Paris, France, 3-6 September 2017.
- Sander van den Driesche, Frank Bunge, Frieder Lucklum and Micheal J. Vellekoop. 3D-Printing: An attractive tool to realise microfluidic chip holders. *Conference on Microfluidic Handling Systems*, Enschede, Netherlands, 4-6 October 2017.
- Martin Oellers, Frank Bunge, Frieder Lucklum, Poornachanda Papireddy Vinayaka, Christian Habben, Melanie Kirsch, Sander van den Driesche, and Michael J. Vellekoop. Microfluidic swap structure to enhance on-chip liquid mixing. *IEEE Sensors*, Glasgow, UK, 29 October - 1 November 2017.

Acknowledgements

The results, that are presented in this thesis, were only enabled by the support and numerous discussions with my friends, colleagues and my supervisor. Here, I would like to express my gratitude to all of them.

First of all, I would like to thank Michael J. Vellekoop for his support as well as for the opportunity to work in the institute and to work on this thesis. Our fruitful discussions helped me to develop new ideas and concepts, but also to realize them. His feedback and motivation encouraged me to submit many abstracts and papers as well as this thesis.

I also would like to thank Gerald Gerlach for his review of this thesis.

I am very grateful to Sander van den Driesche for his valuable support of my work. He helped me with various publications and gave me much advice regarding the scientific work. Last but not least, his enormous knowledge of biology made this thesis possible.

Special thanks belongs to my colleagues of the IMSAS for their input especially regarding the design, the fabrication and experimental problems. In particular, Frieder Lucklum introduced me to 3D-printing, which became an indispensable part of the work. Martin Oellers always took time to support me and to have discussions whenever I got stuck.

Apart from scientific colleagues, the technical team of our institute made this thesis possible by maintaining the clean room and by instructing me with the clean room processes or by running some fabrication steps. Special thanks goes to Christian Habben and André Bödecker who helped with the development of the fabrication processes and who had some ideas how to avoid or solve technical problems.

I am grateful towards the collaborators of the Endosymbiont Project who actually encourage me for the measurement of oxygen consumption. Additionally, the fruitful discussions with Ursula Mirastschijski, Anya Waite, Sørge Kelm, Mario Waespy, Arlo Radtke and Gazanfer Belge motivated me and helped me to solve the problems of measuring dissolved oxygen.

I want to thank the students whose master project or master thesis I supervised. In particular, Sina Reede and Camilla Konermann contributed significantly to this thesis regarding the silica aerogels and the read-out of the phase shift for the oxygen sensing.

Last but not least, I want to thank my girlfriend Anja Rebelein for her support and for proofreading this thesis.